

**BIOMIMETIC DESIGN AND FABRICATION OF TISSUE ENGINEERED
SCAFFOLDS USING COMPUTER AIDED TISSUE ENGINEERING**

A Thesis

Submitted to the Faculty

of

Drexel University

by

Binil Starly

in partial fulfillment of the

requirements for the degree

of

Doctor of Philosophy

June 2006

© Copyright 2006

Binil Starly. All Rights Reserved.

DEDICATED TO

To my wonderful parents,

my mom, Mariamma

and

my dad, Starly

...with respect and love,

“Thinking should be your capital asset, no matter whatever ups and downs you come across in your life”

Dr. A.P.J. Abdul Kalam, President of India

ACKNOWLEDGMENTS

I would like to express my sincere and deepest gratitude to my advisor and mentor, Dr. Wei Sun, for his help, guidance, encouragement and friendship throughout my graduate studies. I admire his hard work, commitment, enthusiasm for research and cheerfulness that has inspired me to pursue a career in academia.

I would also like to thank my advisory committee members Dr. Francis Wang, Dr. Alan Lau, Dr. Jack Zhou, Dr. Moses Noh, and Dr. Ali Shokoufandeh for their participation, time, and helpful suggestions to improve my thesis content.

I would like to take this opportunity to thank the faculty and staff at the MEM Department for their constant support and conversations during my graduate studies at Drexel. I thank Dr Mun Choi for his support, advice and encouragement in my outreach activities within the department and the College of Engineering.

My special gratitude and thanks for the funding support from Therics Incorporated, the National Science Foundation (Grant# 219176 and #0427216), and the George Hill Jr Fellowship for their support of my research activities during the past five years.

I would also like to make special acknowledgments to the current and past CATEL members Zhibin Fang, Ganesh Subbaraman, Lauren Shor, Saif Khalil, Andrew Darling, Connie Gomez, Kalyani Nair, Eda Yildirim, Bobby Chang, Xi Yin, Peter Evans and Xun Zhou for our endless discussions, debates, gossips and for all the help that you have given me. I will miss you all.

TABLE OF CONTENTS

LIST OF TABLES	viii
LIST OF FIGURES	ix
ABSTRACT	xiii
CHAPTER 1: INTRODUCTION	1
1.1. Computer Aided Tissue Engineering	1
1.2. Solid Freeform Fabrication Technologies in Tissue Engineering	8
1.3. Research Objectives	18
1.4. Thesis Outline	19
CHAPTER 2: BIOMIMETIC DESIGN OF TISSUE SCAFFOLDS	21
2.1 Biomimetic Design and Fabrication Approach	21
2.2 Design of Tissue Scaffold Macro-Architecture	24
2.3 Design of Tissue Scaffold Micro-Architecture	31
2.4 Effective Young's Modulus and Tortuosity Characterization	42
2.5 Conclusions	56
CHAPTER 3: DIRECT SLICING FOR FREEFORM FABRICATION OF TISSUE SCAFFOLDS	59
3.1 Introduction	59
3.2 Conventional STL Based Slicing	60
3.3 Direct Slicing of STEP Based NURBS Models	69
3.4 Model Case Studies	83
3.5 Conclusions	95

CHAPTER 4: FREEFORM FABRICATION OF TISSUE SCAFFOLDS	98
4.1 Internal Architecture Design of Tissue Scaffolds.....	98
4.2 Design Manufacturing Interface	105
4.3 Fabrication using 3DP™ and PED Systems.....	116
4.4 Conclusions.....	119
CHAPTER 5: APPLICATION EXAMPLES FOR VIRTUAL RECONSTRUCTION AND PROTOTYPE MODELING	123
5.1 A CT/MRI Based Reconstruction of Anatomic Parts.....	123
5.2 Real Time Surgical Planning and Quality Control	128
CHAPTER 6: CONCLUSIONS AND RECOMMENDATIONS	137
6.1 Summary	137
6.2 Research Contributions.....	139
6.3 Future Research Recommendations.....	141
6.3 Concluding Remarks.....	143
LIST OF REFERENCES	144
VITA.....	152

LIST OF TABLES

Table 2.1: Biomimetic design requirements and possible design solutions	23
Table 2.2: Bone Spatial Heterogeneity -7 layer model.....	47
Table 2.3: Summary of results obtained by FEA analysis.....	49
Table 3.1: STL and STEP based slicing comparisons	96
Table 5.1: Process Comparison – Conversion from CT/MRI images to CAD of the proximal femur.....	127

LIST OF FIGURES

Figure 1.1: Scaffold Guided Tissue Engineering using CAD/CAM Technologies.....	3
Figure 1.2: Overview of Computer Aided Tissue Engineering	6
Figure 1.3: Scaffolds designed in CAD and transferred to SFF systems.....	9
Figure 1.4: Three Dimensional Printing Process	11
Figure 1.5: Extrusion Process through FDM	14
Figure 1.6: Micro-valve/Micro-syringe based deposition systems.....	16
Figure 2.1: Overall Procedure for the biomimetic design and fabrication of a tissue scaffold	25
Figure 2.2: Roadmap from CT/MRI to 3D reconstruction	27
Figure 2.3: Process definition to arrive at a CAD model from CT/MRI data	30
Figure 2.4: Interior scaffold design process.....	33
Figure 2.5: Variations of trabecular bone architecture	34
Figure 2.6: Analogized feature primitives	34
Figure 2.7: A library of designed scaffold unit cells based on different feature primitives	35
Figure 2.8: Standard 2D patterns currently produced by extrusion SFF systems.....	36
Figure 2.9: Hilbert curve recursive generation process	39
Figure 2.10: Scaffold structure with the Hilbert pattern.....	40
Figure 2.11: The Sierpinski curve at Levels 1, 2 and 3	41
Figure 2.12: Scaffold structure with the Sierpinski pattern	41
Figure 2.13: Average QCT Values Measured from CT.....	46
Figure 2.14: Samples of the designed scaffold unit cells.....	47

Figure 2.15: Finite element method for predicting unit cell stress and deformation	48
Figure 2.16: Effect of unit cell material and porosity on unit cell mechanical properties	50
Figure 2.17: Definition of Tortuosity	51
Figure 2.18: Tortuosity Measurement using Tracer Distance Metric Analysis.....	54
Figure 2.19: Two Models with different porosity but same rectangular pore shape having different tortuosity factors.....	54
Figure 2.20: Two models with constant porosity of 48% but different tortuosity factors due to the difference in formation factors.....	55
Figure 2.21: Four types of scaffolds with varying tortuosity particularly in the z-axis....	56
Figure 3.1: The cusp height on faceted surfaces.....	61
Figure 3.2: API slice errors from a major CAD vendor	64
Figure 3.3: General Biomodeling and Medical Rapid Prototyping Process Path.....	65
Figure 3.4: Data Flow during Fabrication.....	67
Figure 3.5: STEP description of a Uniform B-Spline surface	69
Figure 3.6: Step by Step procedure on calculation of NURBS intersection points	71
Figure 3.7: General Slice Algorithm.....	73
Figure 3.8: Refined Process of NURBS using the Oslo Algorithm.....	75
Figure 3.9: Program file organization within algorithm	80
Figure 3.10: Data Flow of the CAD model data.....	83
Figure 3.11: 14 NURBS patch sphere.....	84
Figure 3.12: Data Output Format from the Solidworks Macro	85
Figure 3.13: Subdivision Procedure.....	86
Figure 3.14: Slicing Operation.....	86

Figure 3.15: Format of Ray Cast File for FPS	87
Figure 3.16: Raster Pattern for the sphere	87
Figure 3.17: Raster Pattern for the cone	88
Figure 3.18: Raster Pattern for the foot	89
Figure 3.19: Raster Pattern for the sinus graft model 1	90
Figure 3.20: Raster Pattern for the sinus graft model 2	91
Figure 3.21: Raster Pattern for sinus graft model 3	92
Figure 3.22: Raster Pattern for the sinus graft model 4	93
Figure 3.23: Raster Pattern for the bone with holes.....	94
Figure 3.24: Raster Pattern for the combination bones.....	95
Figure 4.1: Unit cell assignment within scaffold structure	98
Figure 4.2: Decomposition and accumulation for layered manufacturing	101
Figure 4.3: Slicing of Unit Cell and Scaffold and associating them to specific regions	104
Figure 4.4: Intersection of 2D slice patterns onto Scaffold 2D pattern to form 3D structure.....	104
Figure 4.5: IAD algorithm	105
Figure 4.6: Flowchart of process planning for fabricating tissue scaffold	107
Figure 4.7: Fabrication Planning Modules.....	108
Figure 4.8: Unit Cell Input Files Interface.....	110
Figure 4.9: 3D Unit Cell mapping process command window.....	111
Figure 4.10: Rectangular hole in a square shaped scaffold block.....	111
Figure 4.11: Circular hole in a cylindrical scaffold	112
Figure 4.12: Circular hole in a bone structure	113

Figure 4.13: Multiple unit cell architecture in the bone structure.....	113
Figure 4.14: Two different pore architectures assigned to a model structure with multi patterns in a single layer	114
Figure 4.15: Three Pore architectures assigned to a shaped scaffold	115
Figure 4.16: Slices 5, 10, 70 do not meet the area selection criterion and hence no patterning is observed	115
Figure 4.17: Cylindrical and bone shaped scaffold	117
Figure 4.18: The Hilbert and Sierpinski Patterned Scaffold.....	118
Figure 4.19: PCL scaffold with spiral pattern.....	119
Figure 4.20: Multi-porous regions in the PCL scaffold.....	119
Figure 5.1: Image Registration, 2-D segmentation and 3-D reconstruction process	123
Figure 5.2: CAD model construction using MedCAD interface	124
Figure 5.3: CAD model construction using reverse engineering approach.....	125
Figure 5.4: Conversion from Voxel Model to CAD model via STL interface	126
Figure 5.5: Models generated for downstream CAD applications	127
Figure 5.6: Different views of the voxelized skull model	130
Figure 5.7: Virtual reconstruction process.....	131
Figure 5.8: Prototype fabrication using ZCorp 3DP™ system.....	132
Figure 5.9: Real time quality control interface	133
Figure 5.10: Direct conversion of the STL model to DICOM format	135
Figure 6.1: Process flow path from images to final scaffold	137

ABSTRACT**Biomimetic Design and Fabrication of Tissue Engineered Scaffolds
Using Computer Aided Tissue Engineering****Binil Starly
Wei Sun, Ph.D**

The field of tissue engineering brings together the multidisciplinary research of life sciences and engineering to seek man-made substitutes for the regeneration of damaged tissue or organs. A key component in tissue engineering is the use of porous scaffolds to guide cells for attachment, proliferation and differentiation in the tissue regenerative process. Upon satisfactory in-vitro culture, this engineered living scaffold is implanted into the regeneration site of the patient to function as the tissue substitute. Conventional processing techniques for the fabrication of scaffolds often encounter difficulties in the precise control of the internal architecture, interconnectivity and distribution of pores within the scaffold. These challenges, along with the advances in biology, medicine, and information technology for tissue engineering applications, have led to the development of a new field of Computer Aided Tissue Engineering (CATE).

CATE enables a systematic application of computer-aided technologies, i.e., computer-aided design (CAD), image processing, computer-aided manufacturing (CAM), and solid freeform fabrication (SFF) for modeling, designing, simulation, and manufacturing of biological tissue and organ substitutes. Through the use of CATE, the design of intricate three dimensional architecture of scaffold can be realized and these scaffolds can be fabricated with reproducible accuracy to assist biologists in studying complex tissue engineering problems. This thesis reports a research addressing some of the challenges in applying the CATE approach for the biomimetic design and freeform

fabrication of tissue scaffolds. The major research accomplishments reported in this thesis include:

- a) The development of a BioCAD modeling technique for the design and representation of patient specific 3D tissue models based on non-invasive medical image data.
- b) The development of a biomimetic design approach for design of load bearing tissue scaffold subject to multiple biophysical, geometrical and manufacturing requirements. This includes the design of the unit cell micro-architecture based on tissue morphologies, unit cell characterization and evaluation of the mechanical and transport properties, and the use of unit cells as building block to design anatomic tissue scaffold replacements.
- c) The development of a CAD based path planning procedure through a direct slicing algorithm which can convert a neutral ISO (International Standards Organization) standardized STEP (Standard for the Exchange of Product Data) formatted NURBS (Non-Uniform Rational B-Spline) geometric representation to a tool path instruction set for layered freeform fabrication.
- d) The development of a novel Internal Architecture Design (IAD) approach for the mapping of characteristic patterns of the unit cell micro-architectures designed within the 3D scaffold. This design approach is implemented into a process algorithm that converts these 2D patterns to tool path datasets for the 3DP™ (three-dimensional printing) and extrusion based freeform fabrication. .

CATE enables many novel approaches in modeling, design, and fabrication of complex tissue substitutes with enhanced functionality for research in patient specific implant analysis and simulation, image guided surgical planning and scaffold guided tissue engineering. The research will also enable cell biologists and engineers to expand their scope of research and study in the field of tissue engineering and regenerative medicine.

CHAPTER 1: INTRODUCTION

1.1. Computer Aided Tissue Engineering

Currently, the need for organ and tissue substitutes to repair or replace damaged or diseased organs or tissues is on the increase with about a million surgical procedures performed every year in the US alone [Medimonitor, 2000]. Loss of bone tissue due to surgery, trauma, disease or normal aging very often entails the use of substitutes to help repair or replace the damaged or diseased tissue. Currently available bone substitutes, including auto grafts, allograft, and synthetic materials, are the most commonly implanted materials in surgeries conducted countrywide. However, these substitutes are far from ideal and have many associated problems. The problems include: non-availability of donor site tissue, implant subsistence and failure, immune rejection and fixation problems. In addition, the existence of non-living synthetic materials in the body calls for recurring surgeries since the material does not grow or adapt to the changing environments that the patient undergoes. In this scenario, there is a growing need and demand for “living substitutes” that can help grow the patient’s own functional tissue and is currently an active area of research, in what has been termed as “Tissue Engineering” [Langer 1993, 1995, 1999].

Tissue Engineering as defined by the National Science Foundation and coined by Y.C. Fung, in 1987 is the application of principles and methods of engineering and life sciences toward the fundamental understanding of structure-function relationships in normal and pathological mammalian tissues and the development of biological substitutes to restore, maintain, or improve tissue function [Viola et al, 2003]. A fundamental

premise for tissue engineering lies in that sample cells can be cultured *ex vivo*, introduced within the scaffold in an appropriate environment for cell and tissue growth, and the newly grown tissue/organ can eventually be implanted to restore the patient tissue function. Regeneration of functional tissue or organ structure requires a scaffold to guide the overall shape and the three dimensional growth of multiple cell types and is the central component of the tissue engineering concept [Lanza, 2000]. Currently, researchers have succeeded in growing human skin [Eaglstein et al, 1997], human urinary bladders [Atala, 2006], non load bearing cartilage such as the ear [Saim et al, 2000], and to a limited extent in bone tissue substitutes [Shao et al.2006, Borden et al., 2002]. It is hoped that in the next several decades, human tissue/organ such as the bone, liver and heart valves can be grown and be available for clinical applications.

During the early years of tissue scaffold research, there was limited capability in being able to control the scaffold architecture due to the lack of automation and computer integrated fabrication. Initially, chemical based methods of fabrication such as salt leaching [Laurencin et al, 1996], gas foaming [Murphy et al., 2000], fiber bonding [Lu et al., 1996] to name a few, were used to fabricate scaffolds that resulted in a random pore generation and distribution. Limited architectural control was achieved by adjusting the chemical fabrication parameters. As a result, repeatable structures could not be ensured and hence there was no means for a structured characterization or systematic biological study process. Since 2000, chemical based techniques made way to alternate methods of fabrication that had the capability to be integrated with CAD/CAM technologies [Zeltinger et al., 2001, Zein et al, 2002, Wang et al, 2004, Khalil et al., 2005]. This made it possible for the scaffolds to be designed using CAD software and then transferred to

rapid prototyping (RP) machines for final fabrication. The primary advantages that this process allowed were its ability to produce reproducible structures for biological and clinical study, process capability in producing micron-size features, the ability to develop computational and simulation algorithms that could predict the effective mechanical and transport properties and the availability of a large number of candidate biomaterials that could be used as the scaffolding material [Sun et al, 2002, Hutmacher et al 2004]. The current preferred approach among bone tissue engineering researchers is graphically displayed in Figure 1.1.

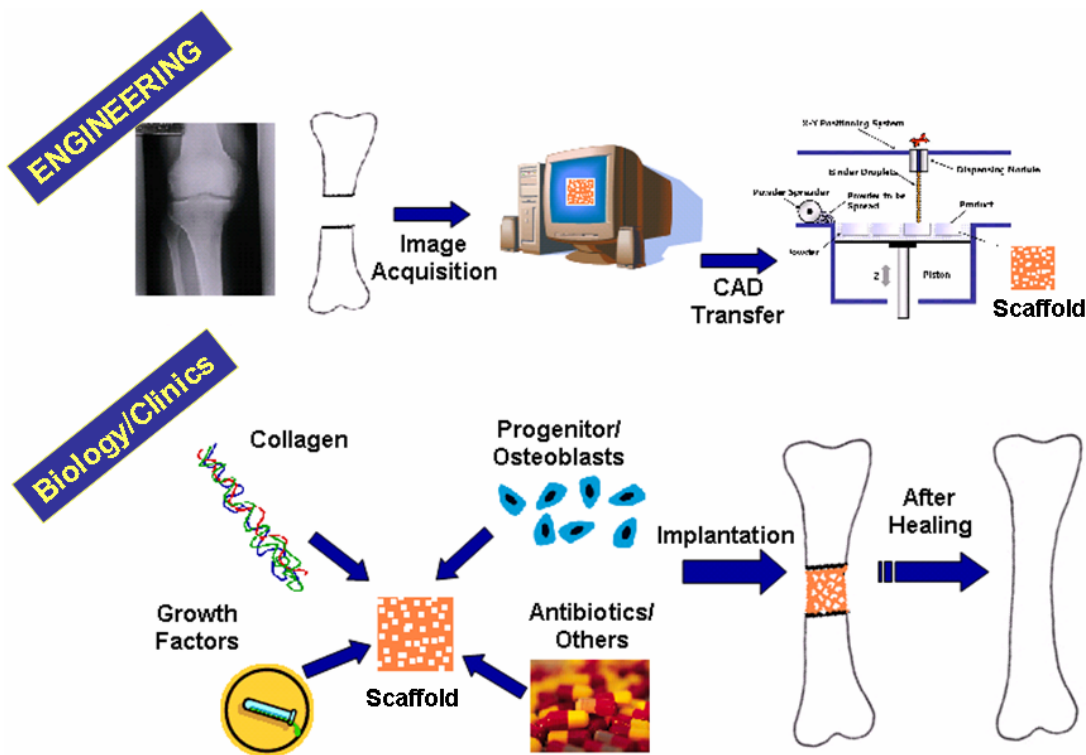


Figure 1.1 : Scaffold Guided Tissue Engineering using CAD/CAM Technologies

Essentially, non-invasive image acquisition technologies are utilized to obtain the sliced 2D data of the defect site and reconstructed into a 3D model. The 3D model of the

defect site is used to aid in the design of a 3D scaffold that fits within the defect site. The model is then transmitted to the available rapid prototyping system for fabrication. The scaffold is replenished with the patient's own cells, growth factors, collagen and nutrients, grown in an incubator for a period of time and is then implanted into the defect site of the patient. After healing, the scaffold degrades away leaving behind the patient's own regenerated tissue. The central component in this approach is the "design of the scaffold" that must meet multiple mechanical, biophysical, biological requirements before this approach could be made viable.

The design of the scaffold takes into account several parameters which include scaffold porosity, pore size, pore organization and interconnectivity of the tissue scaffold structure. These have been identified by researchers [Hollister et al., 2002, Hutmacher et al, 2000, Yang et al., 2001, Li et al., 2001] to be some of the important factors that contribute to tissue regeneration in a scaffold. These features aid in the transportation of nutrients that enable the proliferation of cells and allow the tissue scaffold to act as a suitable support for tissue regeneration and eventual healing. Control over the scaffold internal pore architecture can lead to scaffolds with desired biological, mechanical and transport properties. Similarly, control over the external architecture of the scaffold can help match with the geometrical fitting qualities at the defect site. Therefore, any man made substitute, must at best mimic the natural tissue properties in order to function as a true substitute by providing an immediate mechanical fixation and support upon implantation, particularly for load bearing substitutes such as bone.

Design of scaffolds in current enabling CAD software is by no means an easy task. Current CAD software functional capabilities are geared towards the design of

mechanical components based on conceptual designs that are borne out of the minds of engineers and scientists. Tissue scaffold substitutes are not man-made and must follow strict design rules set forth by nature as a result of evolution taken place over millions of years. A single design of a tissue scaffold could potentially encompass multi-scale features ranging from the nano-scale all the way up to the meso-scale level. Inclusion of a hierarchical multi-scale structure of features within a scaffold necessitates the development of Biomodeling process paths, specialized computational methods and process planning algorithms for its design and fabrication. How much of these natural nano and micro features must be mimicked within a man-made substitute is currently under debate by the scientific community. It is understood that features whether it be at the nano-scale level or at the meso-scale will influence cellular behavior and therefore, the process capability to reproduce and replicate multi-scale features for the success of scaffold guided tissue engineering is important.

Recent advances in computing technologies both in terms of hardware and software have helped in the advancement of CAD in applications beyond that of traditional design and analysis. CAD is now being used extensively in the biomedical industry in applications ranging from clinical medicine, customized medical implant design to tissue engineering. This has largely been made possible due to developments made in imaging technologies and reverse engineering techniques supported equally by both hardware and software technology advancements [Keppel et al., 1975, Bajaj et al., 1996, Marsan et al., 1996]. Utilization of computer-aided technologies in tissue engineering has evolved the birth of a new field of Computer-Aided Tissue Engineering (CATE), which integrates advances in Biology, Biomedical Engineering, and Information

Technology to Tissue Engineering application. CATE can be defined as the application of enabling computer-aided technologies, including computer-aided design (CAD), image processing, computer-aided manufacturing (CAM), and rapid prototyping (RP) and/or solid freeform fabrication (SFF) for modeling, designing, simulation, and manufacturing of biological tissue and organ substitutes. Specifically, CATE encompasses the following three major applications in tissue engineering: 1) computer-aided tissue modeling; 2) computer-aided tissue informatics; and 3) computer-aided tissue scaffold design and manufacturing. An overview of CATE is presented in Figure 1.2.

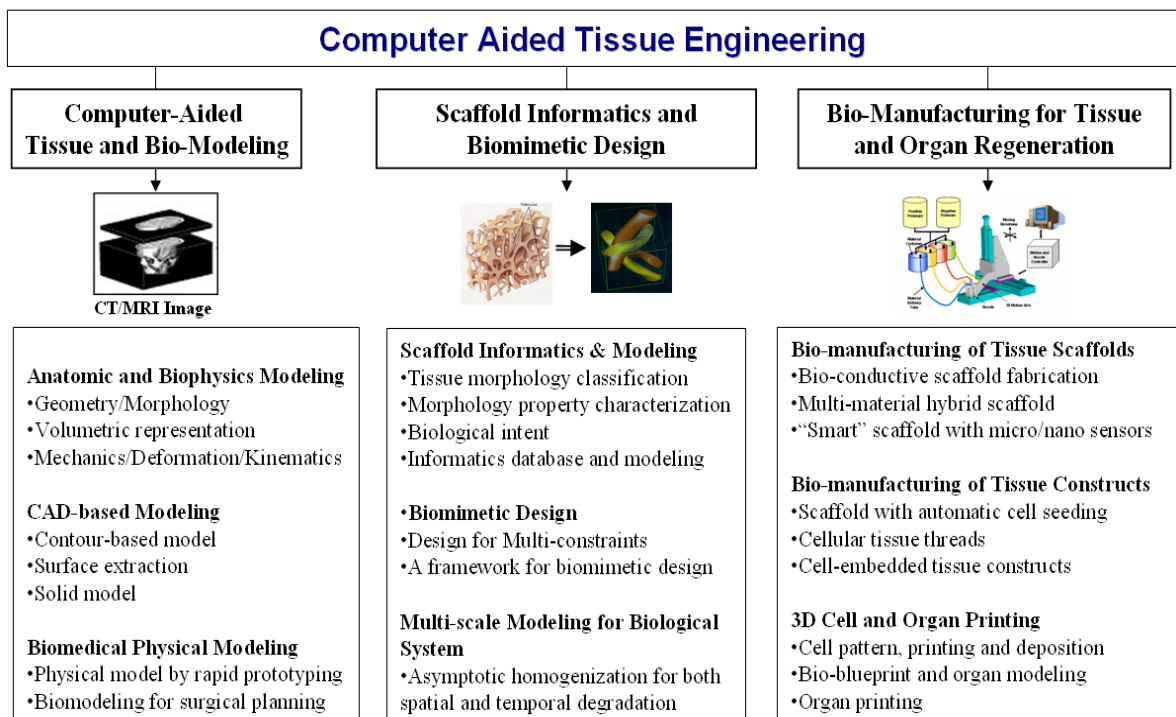


Figure 1.2: Overview of Computer Aided Tissue Engineering

1) Computer Aided Tissue Modeling

Human anatomic structure has evolved over millions of years leading us to believe that the human organ structure has been optimized to meet the current physiological needs. Therefore, for any man made tissue substitutes to be designed, anatomic data must be obtained to provide us with a starting point. This anatomic data can be obtained digitally using non-invasive imaging procedures such as CT/MRI/PET technologies. Each of these scanning procedures generates a set of scanned slices which can be used to reconstruct data in the form of 3D models of the tissue of interest. These technologies are accompanied by the use of computer aided reconstruction software which aid in the generation of 3D voxel models that can be used for medical diagnosis [Van et al 2006], surgical planning [Piatt et al, 2006], biomedical implants [Evans et al, 2006,] and tissue engineering [Hollister et al, 2002, Hutmacher et al., 2004, Ho et al., 2006].

2) Computer Aided Tissue Informatics

The vast technological development in imaging, sensing, optical microscopy and characterization technologies have provided the capability for tissue engineering researchers to gather a variety of data from native tissue and tissue grown from substitutes to enable tissue classification procedures, property estimation, cell adhesion and aggregation studies, gene sequencing etc [Valencia et al., 2005]. A lot of these studies are performed using advanced image processing algorithms, statistical tools and analysis software. The understanding of cellular constituents and metabolism at the smallest scale can be directly applied to the characterization and analysis of features on

the tissue scale (tissue informatics). The information obtained from such characterization procedures can in turn be used to evaluate the design parameters of the tissue substitute and to tailor them for any specific application.

3) Computer Aided Tissue Scaffold Design and Manufacturing

Design of 3D tissue scaffolds or tissue substitutes for tissue engineering application should consider the complex hierarchy and structural heterogeneity of the host tissue and/or scaffold environment. Other than important factors of porosity, pore size, interconnectivity, and transport property for nutrients that would enable the ingrowth of new cells and cell-tissue formation, the designed scaffolds should also be able to have compliant mechanical properties with the host environment as well as required mechanical strength after implantation in the design of load bearing tissue scaffolds or substitutes such as bone and cartilage [Chu et al., 2002, Hutmacher et al., 2004, Hollister et al., Gordon et al., 2005]. The use of computer aided manufacturing systems for the production of tissue scaffolds structures have opened up a new field in the study of scaffold guided tissue engineering. Complex interior structures made out of a variety of biomaterials can be reproducibly fabricated and its effect on cellular activity can be studied. Biomaterial distribution, surface topography, pore structure and distribution, cellular encapsulation can be accurately controlled to achieve the desired properties.

1.2. Solid Freeform Fabrication Technologies in Tissue Engineering

Application of solid freeform fabrication (SFF) technologies in the design and fabrication of scaffolds/constructs in tissue engineering constitutes the third component in CATE. SFF systems are directly linked to CAD software which facilitates the design of the scaffold in a virtual environment after which the CAD model is transferred to the systems for fabrication. Unlike, traditional machining, the SFF system builds parts by selectively adding material as specified by the CAD model. Figure 1.3 shows the process by which a scaffold designed in CAD software is converted to machine instructions for part buildup. Since the 1990's, SFF technology has been primarily used in the rapid prototyping industry to make prototypes of parts that were designed in CAD. This technology allowed the rapid fabrication of conceptual designs, thereby allowing for design changes early on in the product development cycle. However, over the last 6yrs, researchers began to use these technologies to produce scaffolds for tissue engineering. The system's ability to achieve precise control over material distribution, high level of design capability in the model's internal structure and the ability to fabricate highly reproducible scaffolds with a variety of composite biomaterials makes it attractive for tissue engineering applications. These reasons have mainly contributed to making the SFF process the most favored approach for the fabrication of engineered scaffolds/constructs.

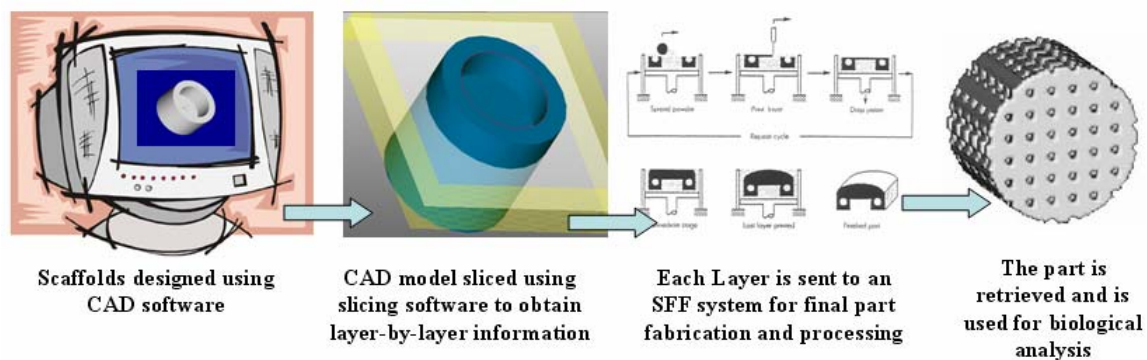


Figure 1.3: Scaffolds designed in CAD and transferred to SFF systems

Among the currently available SFF techniques, 3-D printing (3DP) [Griffith et al, 1997, Zeltinger et al., 2001, Lam et al., 2002], fused deposition (FDM) [Zein et al., 2002, Wang et al, 2004, Kalita et al, 2003] and the Micro-nozzle based extrusion systems [Landers et al., 2002, Vozzi et al., 2003, Khalil et al., 2005] appears to be the currently active areas of research for the freeform fabrication of tissue scaffolds. In the following section, current state of the art designs produced by these systems as applied to scaffold fabrication will be discussed. Although other systems such as the Stereolithography (SLA) [Tan et al., 2003], Selective Laser Sintering (SLS) [Leong et al, 2001, Williams et al, 2005] techniques have been used for tissue engineering applications, their combined disability to provide bio-friendly fabrication environments and a relatively low library of candidate biomaterials, resulted in its low degree of popularity among tissue engineering researchers.

1) Three Dimensional Printing (3DP™) process

Three dimensional printing technology (3DP™) was developed in MIT [Cima et al, 1994] and was one of the first SFF techniques to be used in the fabrication of scaffolds

and drug delivery applications. A 3D model is made by first spreading down an even layer of fresh biomaterial powder in the build box and having a nozzle print head drop the binder in specified patterns on the powder particles. The binder “fuses” the particles together to form one layer of the model. The process is repeated by spreading an additional layer of powder with a specified layer thickness on the previous layer with the print cycle continuing until all the layers have been built. The process is analogous to having a “word document” printed using an inkjet printer, except in this case all of the “papers” fuse together to form one integral model. After the process is completed, the model is salvaged from the build chamber and air blown to remove any unbound powder. The process is shown in Figure 1.4.

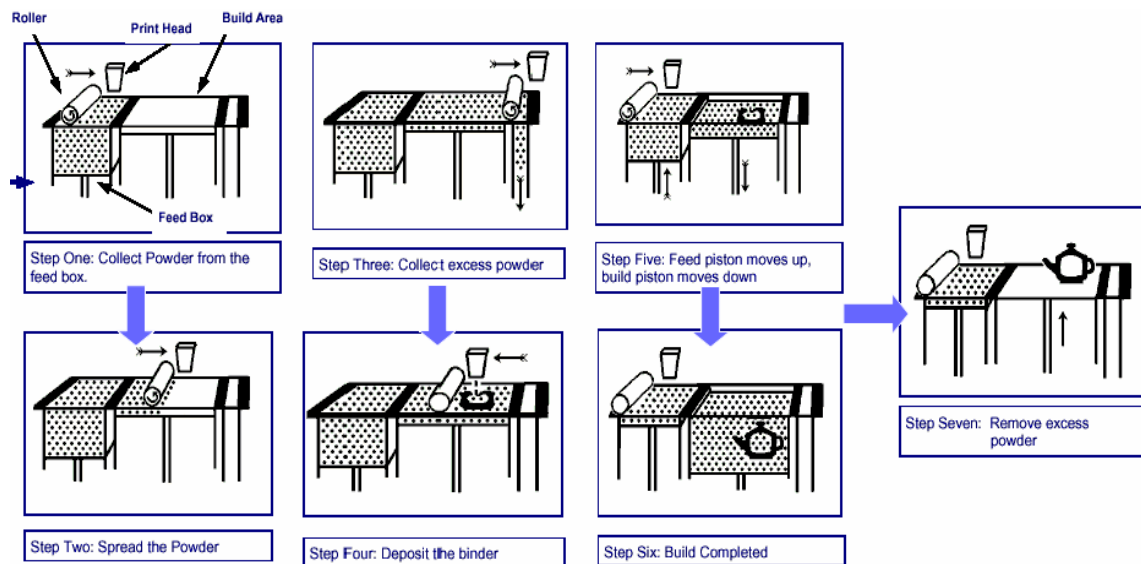


Figure 1.4: Three Dimensional Printing Process

Licensing the technology developed at MIT, Therics Incorporated has applied the 3DP™ process to tissue engineering and developed the *TheriForm™* process. This

process allows for control on both the structure and composition of drug delivery systems such as pills and scaffolds at <1mm resolutions. The process does not use heat and hence can be used in conjunction with biologically active molecules, cells, growth factors and thermal responsive materials. The process is designed to be controlled at the macroscopic scales (1mm ~ 20mm) by CAD models and at intermediate and microscopic features (100µm to 1mm) by using several post processing techniques. Various experiments have been reported using the process: Zeltinger *et al.* created poly (L-lactic acid) scaffolds for testing the effects of porosity on cellular growth in vitro using fibroblasts, smooth muscle cells, and epithelial cells. Kim, *et al.* produced scaffolds from polylactide-coglycolide (PLGA) that contained interconnected channels to improve circulation. Experiments by Wu, *et al.* reported the feasibility of computer-aided drug design by designing the concentrations of the drug within a pill and using the TheriForm system to produce drug gradient pills. Concentrations of the drug can be minutely controlled and deposited while creating the pill to produce patient specific customized drug release profiles.

The three dimensional printing techniques offers the following advantages over conventional and other SFF techniques for scaffold fabrication:

- a) Computer guided fabrication process with direct linkage to CAD software packages. This allows for repeatable and accurate reproduction of scaffolds since the data is obtained from the same master file.
- b) Bio-friendly manufacturing environment with no excessive use of heat or harsh chemicals. Biomaterial powders that include PLLA, starch, dextran, gelatin, hydroxyapatite with their compatible binders have been used for the scaffold fabrication process.

- c) Mass production of tissue scaffolds is possible due to the high speed ink-jetting process of the print-heads and is a significant advantage over the FDM.
- d) The biomaterial powder acts as the support material and hence do not require the use of any additional support build structure.

However, they do lack in certain features that limits its use for certain applications which are:

- a) Features sizes are limited to 300 μ m and above due to the difficulty in the removal of unbound powder from the pores of the scaffolds. Air blowing alone will not result in complete removal of powder from the interior pores.
- b) The surface roughness and aggregation of biomaterial powder particles after final build up affects component resolution and mechanical properties of the scaffold.
- c) The requirement of having the biomaterial in its powder form requires the use of special and expensive pre-processing techniques.
- d) Low viscosity binders can only be used in the ink jetting process. Hence, the base biomaterial will always have to be present in the build bed. This therefore precludes its use to the fabrication of hard tissue substitutes such as bone.

2) Fused Deposition Modeling (FDM) process

The fused deposition process overcomes the 3DP disadvantages by having the molten biomaterial extruded out of a nozzle. Filaments of the thermoplastic biomaterial are fed through rollers into a liquefier chamber that melts the biomaterial and is then extruded out through a computer controlled nozzle stage to produce strands that are deposited on the substrate. The process cycle continues with the strands continuously

extruded out to produce roads that are built upon each other. Varied internal patterns can be obtained by orienting the strands in specific angles. Multiple nozzles may be necessary for building models that require the simultaneous buildup of support architectures. Figure 1.5 shows the extrusion head of the FDM system.

The need for filaments prevents the FDM process from having biomaterials that are either brittle or too soft. This led to the development of the Precision Extrusion Deposition (PED) system at Drexel, in which the molten biomaterial is forced out through the nozzle by the pressure created by a precision screw [Wang et al, 2004]. This allows the material to be in the form of pellets or small chunks for the extrusion process making it suitable for composite biomaterial blends. Scaffolds made out of Poly-ε-caprolactone/hydroxyapatite with percentages of up to 65% and Poly-4-Hydroxy-butyrate has been extruded using the process.

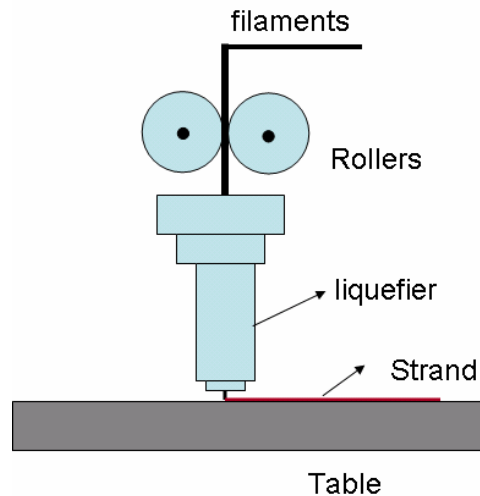


Figure 1.5: Extrusion Process through FDM

The FDM extrusion techniques offer the following advantages over the 3DP process, although they share a lot of common features:

- a) Features sizes at 100 μ m and above are easily and reproducibly achievable with excellent uniformity of the fill gaps, the depositing struts, and internal pore connectivity.
- b) The process does not require the need for post processing steps and hence the part can be used as is.
- c) Limited wastage of biomaterial in comparison to the 3DP process especially when the biomaterial is expensive or is available in limited quantities.

The disadvantages of the FDM process are:

- a) Although the process does not use harsh chemicals, the use of heat often in excess of 70°C prevents the technology from being used in conjunction with biological species and molecules.
- b) They require the use of support structures for parts that contain overhanging or undercut features.
- c) Mass production of scaffolds is difficult and expensive to implement due to the extrusion process.
- d) Most biomaterials that can be extruded out through the nozzle system are most often used for bone tissue engineering. Scaffolds made for soft tissue applications are yet to be produced.

3) Micro-syringe based biopolymer deposition

The use of hydrogels for tissue scaffolding for applications in cartilage, nerve regeneration and drug delivery have led to the development of SFM systems that utilize pneumatic micro-valves coupled with the use of micro-syringes for the deposition of

polymers. Structural formation is achieved by either ionic or covalent means through the use of cross-linking agents. Ang et al, 2002 presented work on using a 3D plotting technique for the fabrication of chitosan-hydroxapatite scaffolds. Landers et al, 2002 reported experiments on fabricating tissue scaffolds from thermo-reversible hydrogels using 3D plotting freeform fabrication systems. Vozzi et al, 2004 presented work on a novel method for deposition of biopolymers in high-resolution structures using a pressure-activated syringe. Khalil et al, 2005 have extended the use of pneumatic nozzle systems to incorporate delivery of multiple biomaterials through the use of multiple nozzles for the fabrication of heterogeneous alginate tissue constructs as illustrated in Fig 1.6.

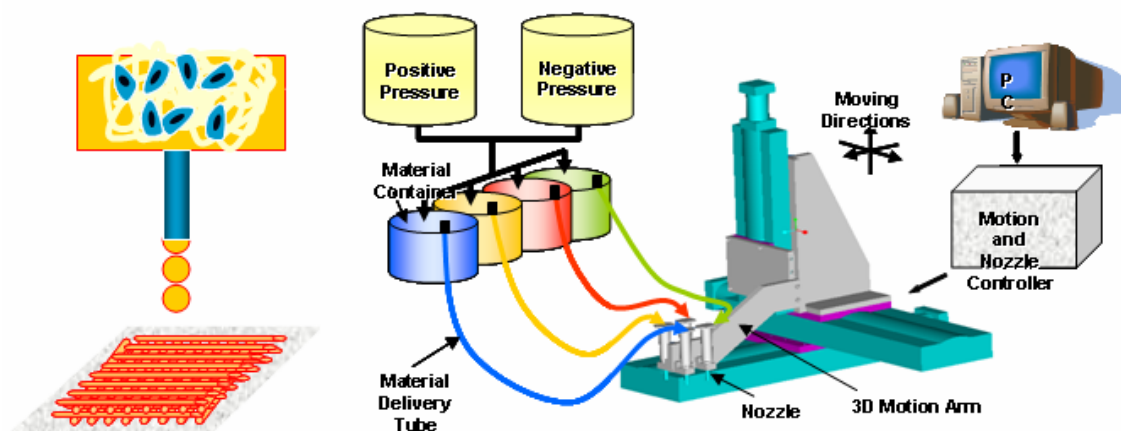


Figure 1.6: Micro-valve/Micro-syringe based deposition systems

These systems have two clear advantages over the 3DP and FDM based methods that make it attractive for soft tissue engineering applications.

- a) The deposition technique permits the use of hydrogel biomaterials that are suitable for cell encapsulation example, Alginate, chitosan, fibrin or composites of these materials.
- b) The deposition can take place in a sterile environment and at room temperature. This means that it can apply unstable and thermally sensitive biomaterials since it does not require any heating in the process. This technology enables the use of critical bio-components such as cells, growth factors which can be incorporated into the scaffold fabrication process for deposition.

The disadvantages of the system are similar to that of the FDM:

- a) Structural formation techniques are more complex and at times difficult to control. The scaffolds produced are soft with low mechanical properties and can be suited for only cartilage and nerve applications.
- b) Similar to the FDM, the process would require the use of support structures for the fabrication of tissue scaffolds that require support materials.

Common to all of the above systems, the solid model of the scaffold is designed in a 3D CAD package or imported from 3D CT/MRI scanners and this digital information is converted to a neutral STL format. The STL model is sliced and is transferred to machine specific cross-sectional layer instructions for final part build up. A major challenge in this step is the process algorithms that come into play during the transfer of CAD data to the SFF systems. The CAD scaffold data contains multi-scale information such as features as large as 50mm to microscale features as small as 50 μ m. The use of

STL files as the transition file format is often a bottleneck and therefore efficient algorithms must be devised for the fabrication of tissue scaffolds from CAD packages.

1.3. Research Objectives

The objective of this research is to develop a design, characterization and fabrication approach for man made tissue substitutes/scaffolds using enabling CAD/SFF technologies through the use of computer aided tissue engineering. This thesis will present some salient advances of bio-CAD modeling techniques and application in computer-aided tissue engineering, including biomimetic design, analysis, characterization and freeform fabrication of tissue engineered substitutes. Specifically, the research has the following activities:

(1) To develop an image-based computer modeling approach for the characterization and development of a computer based informatics model for three-dimensional heterogeneous tissue structure representation, with application to design and freeform fabrication of load bearing scaffolds.

(2) To develop a biomimetic design approach for the inclusion of complex unit cell micro-architectures under multiple biophysical, geometrical and manufacturing requirements for applications in guided tissue regeneration.

(3) To develop a direct slicing algorithm for the conversion of STEP-formatted NURBS freeform models to tool path instructions for raster based freeform fabrication machines.

(4) To develop a design manufacturing interface for the implicit representation of micro-architecture within tissue scaffolds and to transfer this data to freeform fabrication

machines, specifically, the TheriForm™, Precision Extrusion Deposition (PED) and the Multi-Nozzle Deposition (MND) systems.

1.4. Thesis Outline

This thesis is outlined as follows:

Chapter 2 presents an overall approach to the design of the macro and micro-architecture of tissue scaffold. Reverse engineering approaches that utilize enabling technologies for the generation of the tissue substitute CAD model is described. A unit cell methodology is presented for the inclusion of micro-architecture within the tissue scaffold CAD model. New internal pore architecture designs by making use of space filling curves that extends the general use of layer road patterns (0/90, 0/60) for extrusion based SFF systems has been developed. Two characterization techniques have been developed and presented to estimate the effective mechanical and tortuosity properties of the designed scaffold respectively.

Chapter 3 describes a direct slicing algorithm to transfer CAD models to SFF systems which makes use of the international CAD transfer format STEP as the input file of the model to be prototyped. The approach described here is feasible for both traditional manufacturing designs as well as for biomedical applications. We have currently focused on NURBS based freeform shapes to demonstrate the capability of the algorithm and the proposed methodology with regards to raster line pattern layout suited for the three dimensional printing 3DP™ machines.

Chapter 4 describes a process tool path algorithm for the freeform fabrication of the designed tissue scaffolds, including a novel Internal Architecture Design (IAD)

approach which enables the generation of internal scaffold patterns from architecture designs of the scaffold building blocks. The output of such a process would be to have scaffolds with intended interior architecture which ensures the right pore size, pore shape and interconnectivity throughout the entire scaffold structure while making use of current CAD technologies. The process has been implemented using the 3DP™ and PED fabrication systems.

Chapter 5 describes two application case studies that make use of the techniques described in chapter 2. The first example is a case study that describes the reconstruction of anatomic parts from CT/MRI data such as the Femur bone, Ankle, Sinus etc. Techniques that are presented are extremely useful for the generation of a CAD model for downstream applications such as FEA and CFD analysis. The second case study presents a clinical study that was performed at the St. Christopher's Children's Hospital which showcases the marriage of computer-assisted design methods to a commercially available neurosurgical image-guidance system in the treatment of a case of anterior plagiocephaly. The technique utilizes using an image based virtual reconstruction approach to produce plaster prototypes that were used to guide the surgery in real time.

Conclusions, recommendations for future work of this research are presented in Chapter 6.

CHAPTER 2 : BIOMIMETIC DESIGN OF TISSUE SCAFFOLDS

2.1 Biomimetic Design and Fabrication Approach

Load bearing bone tissue scaffolds must have certain characteristics in order to function as a true bone substitute that satisfies certain requirements which include biological, mechanical, geometrical and manufacturing constraints. Each of these constraints can be incorporated into a design solution that is specific to the required application. Table 2.1 describes the various design requirements for tissue engineered substitutes with their corresponding design solution. These design solutions can help to meet these requirements and constraints. In no order of preference, the requirements include:

1) Mechanical requirements -- The designed scaffold must provide structural support at the site of replacement while the tissue regenerates to occupy the space defined by the scaffold structure. Scaffold structures must possess the required mechanical stiffness and strength of the replaced structure. This requirement helps the bone substitute to sense load transfer through the substitute and hence be able to maintain its function. Incompatible stiffness can cause stress shielding resulting in the failure of the scaffold. This can be met by using the right biomaterial with the required stiffness and adjusting the porosity of the scaffold to obtain the desired properties.

2) Geometrical requirements -- It must be of a geometric size and shape that fits in at the site of replacement. The defect site must be imaged and will be digitally reconstructed to aid in the design of the scaffold external geometry. The geometry will be reconstructed

into a CAD model that can be used to instruct manufacturing systems for final fabrication in the required shape.

3) Manufacturing Requirements -- The selected biomaterial that satisfies the first requirement must be compatible with the available manufacturing process to fabricate the scaffold. Processes that do not use toxic chemicals and those that do not adversely alter the properties of the biomaterial are preferred. The selected manufacturing process must also be capable to reproduce the intended design in terms of required external and internal architectural features of the scaffold. Any post processing steps that may be required should not damage the scaffold or should not leave chemical residues on the final scaffold. Depending on the final application, suitable manufacturing systems that are capable to produce the final scaffold are selected.

4) Biological requirements -- The designed scaffold must facilitate cell attachment and distribution, growth of regenerative tissue and facilitate the transport of nutrients, oxygen, chemical cues and removal of wastes. This requirement can be achieved by controlling the porosity of the structure, by providing pore interconnectivity inside the structure, by selecting suitable biocompatible materials with controlled biodegradable characteristics with no undesirable byproducts. Interactions between cells and extracellular matrix are some of the key factors to study cell migration, proliferation, differentiation, and apoptosis, which all are critical functions for a tissue-engineered construct. Unfortunately, these requirements are not fully understood by researchers and are a current topic of intense research to study the complete set of biological requirements that must be satisfied before being able to function as a true biomimetic true substitute.

However, it is certain that the suggested design solution does indeed control the success of a tissue substitute.

Table 2.1: Biomimetic design requirements and possible design solutions

Design considerations	Possible design solution
1) Mechanical requirements: <ul style="list-style-type: none"> ■ scaffold structural integrity; ■ internal architectural stability; ■ scaffold strength and stiffness; 	<ul style="list-style-type: none"> ■ biomaterial selection; ■ internal architecture; ■ porosity and pore distribution; ■ fabrication method;
2) Geometrical requirements: <ul style="list-style-type: none"> ■ anatomical fitting; 	<ul style="list-style-type: none"> ■ scaffold external geometry
3) Manufacturing requirements: <ul style="list-style-type: none"> ■ Process Ability ■ Process Effect 	<ul style="list-style-type: none"> ■ Advanced Manufacturing using SFF based techniques ■ Process controlled algorithms using appropriate process planning instructions
4) Biological requirements: <ul style="list-style-type: none"> ■ cell loading, distribution, and nutrition; ■ cell attachment and in growth; ■ cell-tissue aggregation and formation; 	<ul style="list-style-type: none"> ■ biomaterial selection; ■ preferred internal architecture and layout ■ pore size and interconnectivity; ■ Vasculature

Our overall CATE design approach begins with the acquisition of non-invasive images and image processing steps of the appropriate tissue region of interest. This is followed by a three-dimensional reconstruction of anatomical structure using commercially available medical reconstructive and reverse engineering software. The next step is to appropriately devise a process by which tissue structural heterogeneity can be characterized through a homogenization technique, and to define tissue anatomic representative features for generating CAD based unit cell interior architectures. Based on the designed CAD geometrical configuration and the intended scaffold materials, finite element methods are applied to determine the corresponding mechanical properties.

The calculated properties are further compared to the replaced tissue mechanical properties characterized through qualitative computed tomography (QCT) method. The unit cells with matching properties are selected as candidates unit cells to make up the tissue scaffold. The candidate unit cells will be further evaluated according to their internal architectures and the intended biological application. Using CAD solid modeling based Boolean operations, a set of selected candidate unit cells would be integrated with the shape of the anatomic part (ex: bone) to form the tissue scaffold with specified internal architecture and structural properties to match that of the replaced tissue based on the characterization analysis. Once the complete CAD database of the bone tissue scaffold structure is in place, a process planning and tool-path instruction set will be generated based on the selected solid freeform fabrication techniques that would be able to manufacture the designed tissue structures. An overall procedure of the CATE based biomimetic modeling, design and fabrication for bone tissue scaffold is illustrated in Figure 2.1.

2.2 Design of Tissue Scaffold Macro-Architecture

To meet the geometrical size requirements, the external architecture of the scaffold must be reconstructed and represented as a CAD model for use in downstream applications. The following sections describe the techniques and steps used in the creation of the external architecture from image based data using commercially available technologies.

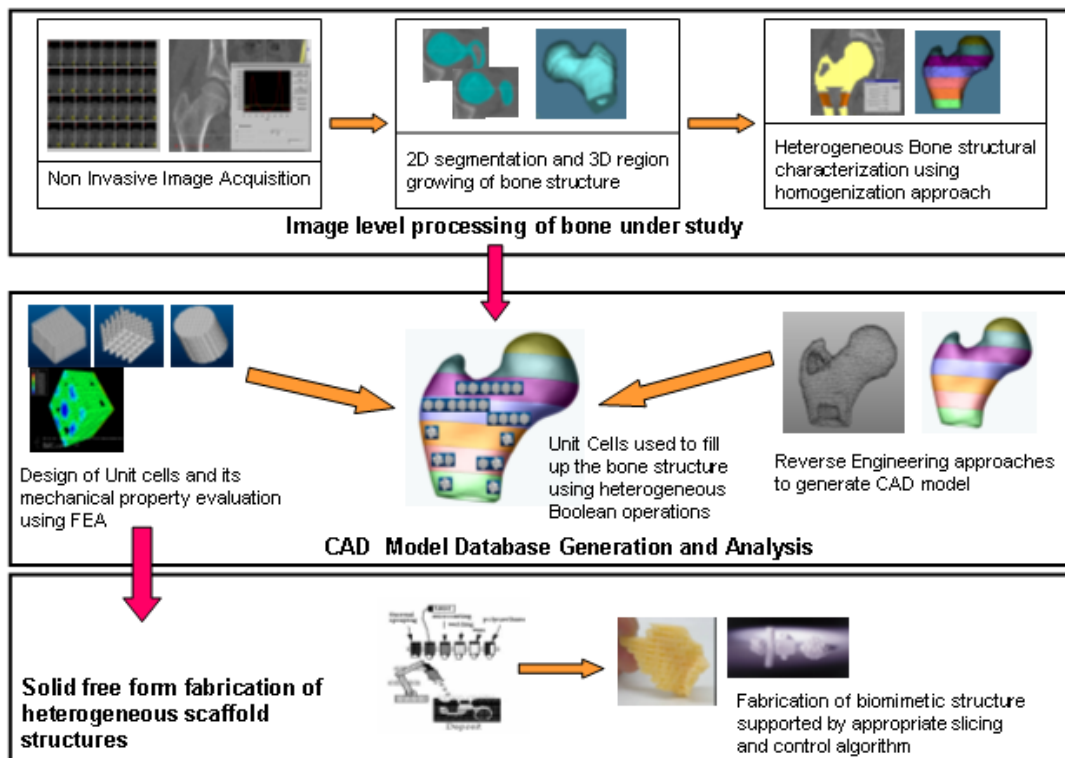


Figure 2.1: Overall procedure of modeling and design of the biomimetic bone scaffold

2.2.1 Image Based Biomodeling

Advances in imaging and software technology have prompted its use in the design of patient specific implant development. Several studies have been reported in the literature that has described the use of 3D reconstruction steps to help in a better understanding of anatomical functionality and morphological analysis. We have attempted to focus on the different methods through which a CAD model is generated from image based data. The general methodology is to reconstruct the 2D image set into a 3D voxel model and used for further evaluation, though a CAD model of the anatomic structure was never generated. This could be attributed to the fact that CAD based models were not necessary for the different applications image based modeling was used for and expensive personal computing power would be required to generate CAD models of

complex anatomic parts.. However, with the increased research in the field of tissue engineering and interest within the customized medical implant design industry, this has called for the need for Bio-CAD models to be used for advanced modeling and analysis. These image based technologies can be used in the design and fabrication of biomimetic tissue scaffolds since obtaining the outer architecture is critical to successful implantation.

Construction of a Bio-CAD model for a specific tissue often starts from the acquisition of anatomic data from an appropriate medical imaging modality. This is referred to as image-based Bio-CAD modeling in which the imaging modality must be capable of producing three-dimensional views of anatomy, differentiating heterogeneous tissue types, and generating computational tissue models for down stream applications, such as surgical analysis, planning and simulation. In general, an image based bio-CAD modeling process involves the following three major steps: 1) noninvasive image acquisition using CT/MRI imaging modalities; 2) imaging process and three-dimensional reconstruction (3DR) to form voxel-based volumetric image representation; and 3) construction of CAD-based model in an internationally accepted format.

2.2.2 Reconstruction for 3D Image Representation

Three-dimensional voxel models are reconstructed by a two step 2D segmentation and region grow process. 2D segmentation is defined as the extraction of the native geometry data using a non-invasive image acquisition technology such as a CT scan data set [Mankovich et al., 1990]. Each slice is processed independently leading to the detection of the inner and outer contours of the living tissue. The contours are stacked

upon each other in 3D and used as a reference to create the final 3D model. A roadmap for the reconstruction of three-dimensional anatomic models from CT/MRI data is described in Figure 2.2. In the process shown in the roadmap, the CT/MRI images are integrated using 2D segmentation and 3D region growing techniques. The volumetric image data represents an informative model for further analysis. The 3-dimensional anatomic view produces novel views of patient anatomy while retaining the image voxel intensities that can be used for volumetric representation and 3-dimensional image representation. These 3-dimensional images lead to the generation of anatomic models used for contour based generation and 3D shaded surface representation of the medical models. The shaded surface display of 3D objects can involve widespread processing of images to create computer representations of objects. Several visualization issues that cannot be resolved by 3D voxel models provide motivation for the construction of a prototype model. Prototype modeling is done through solid freeform fabrication technologies. The fabricated models assist in applications for surgical planning, preoperative planning, intra-operative planning in computer assisted surgery.

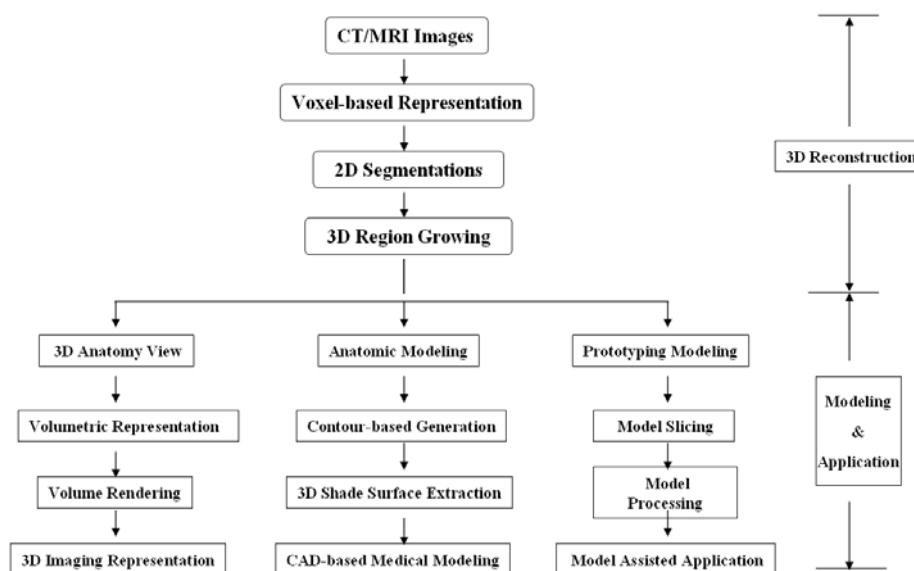


Figure 2.1: Roadmap from CT/MRI to 3D reconstruction

2.2.3 Reverse Engineering Approach

Although noninvasive modalities, such as CT, Micro-CT, MRI and Optical Microscopy can be used to produce accurate 3D tissue descriptions, voxel-based anatomical imaging representation cannot be effectively used in many biomechanical engineering studies. For example, 3D surface model require large amounts of computational power or extreme sophistication in data organization and handling; and 3D volumetric models on the other hand, while producing a realistic 3D anatomical appearance, does not contain geometric topological relation. Although they are capable of describing the anatomical morphology and are applicable to rapid prototyping systems, neither of them is capable of performing structural analysis, biomechanical simulation. In general, activities in anatomical modeling design, analysis and simulation need to be carried out in a topology-based modeling environment, such as using a Computer Aided Design system and CAD-based solid modeling, which is usually represented as 'boundary representation' (B-REP) and mathematically described as Non Uniform Rational B-Spline (NURBS) functions. Unfortunately, the direct conversion of the medical imaging data into its NURBS solid model is not a simple task. In the last few years some commercial programs, for example, SurgiCAD by Integraph ISS, USA, Med-Link, by Dynamic Computer Resources, USA, and Mimics, by Materialise, Belgium, were developed and used to construct a CAD-based model from medical images. However, none of these programs has been efficiently and widely adopted by the biomedical and tissue engineering community due to the inherent complexity of the tissue anatomical structures. Effective methods for the conversion of CT data into CAD solid models still need to be developed.

We have evaluated and compared following three different process paths for generating a CAD model from medical imaging data: 1) MedCAD interface approach, 2) Reverse engineering interface approach, and 3) STL-triangulated model converting approach. The outline of the processes is presented in Figure 2.3.

Process Path 1: MedCAD interface

The MedCAD interface, normally as a standard module of medical imaging process software, is intended to bridge the gap between medical imaging and CAD design software. The MedCAD interface can export data from the imaging system to the CAD platform and vice versa through either IGES (International Graphics Exchange Standard), STEP (Standard for Exchange of Product (STEP) or STL (triangulated) formats. The interface provides for the fitting of 3D primitives such as cylinders, boxes, spheres etc at the 2D segmentation slices. It also provides the limited ability to model a freeform surface (such as B-spline surfaces). The limitation of using the MedCAD interface is the incapability to capture detail and complex tissue anatomical features, particularly for features with complex geometry.

Process Path 2: Reverse engineering interface

The reverse engineering interface approach uses a 3D voxel model as the starting point created from the region grow process. The 3D voxel model is converted to point cloud data form and are loaded into the reverse engineering software (for example, Geomagic Studios by Raindrop Inc). The points are then used to create triangular facets to form a surface model. The faceted model is further refined and enhanced to reduce file

sizes and unwanted features. The freeform surfaces of NURBS patches are used to fit upon the outer shape of the model. Although the process does have a comparatively longer processing time, the results obtained are significantly better than the process path 1 or 3. The resulting CAD model is much more aesthetic, stable in configuration, and prone to less error in data transfer formats, particularly when imported into CAD and FEA applications.

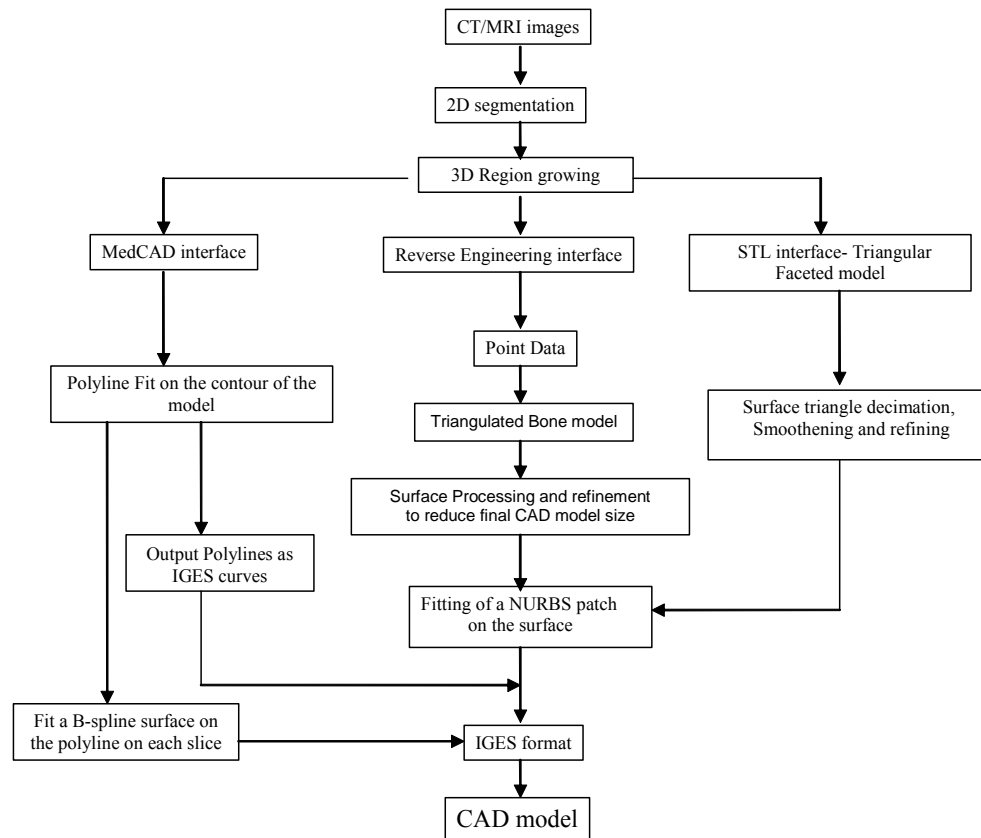


Figure 2.2: Process definition to arrive at a CAD model from CT/MRI data

Process Path 3: STL-triangulated model conversion approach

The 3D voxel model can also be converted to the STL file which contains the triangulated description of the entire voxel model. This STL file can be imported into

triangular mesh editing software for surface refinement and NURBS surface generation. The difference between the triangulated model and the reverse engineering technique is that this approach uses the STL-triangulated surface as the input rather than the point cloud data. Although the process time reqis faster, this approach, however, it inherits all of the limitations of the current STL format, particularly due to the presence of redundant triangles. Complex model shapes often give triangulation errors that result in model invalidity.

2.3 Design of Tissue Scaffold Micro-Architecture

The tissue scaffold micro-architecture is believed to influence the behavior of cells and the biological function of tissues by providing a nutritional pathway as well as a spatial distribution for cell growth and proliferation [Malda et al., 2003, Moit et al., 2005]. Several studies have indicated that cells can be coaxed to migrate and grow along the direction of the designed micro-channels/struts, through which the required cell spatial distribution and tissue function can be realized. In certain applications, certain cell types such as chondrocytes need to be restricted within void spaces [Taguchi et al., 2005] to imitate hypoxic condition which can be met by controlling the design architecture. Anchorage dependant cells are especially responsive to stress characteristics on material architecture. Circular shaped architectures have different stress profiles as compared to straight edges. The architectures also influence the shear stress experienced by attached cells by its effect on fluid flow patterns. The selection of the design of interior architecture hence plays a major role in the final effective mechanical, transport and biological properties of the scaffold.

With the advancement of SFF to be the most favorable approach in the fabrication of scaffolds for tissue engineering applications, the interior architecture of these scaffolds were either designed as a pattern of extrusions, cuts and holes across the surface of the scaffolds in a CAD platform or its interior slice layers were filled in with contours or roads to generate the interior architecture. The former method is used by 3DP, SLS and SLA based RP machines for scaffold fabrication while the latter method is used primarily by FDM and Micro-nozzle extrusion based machines. Fig 2.4(a) and (b) outlines the method by which scaffolds are designed in a CAD platform in published literature. Chua et al., 2002 has used an assembly of designed unit cells and then intersected with the scaffold to obtain the interior architecture using a Pro-E based CAD environment. Nam et al., 2004 have used a similar approach in defining the interior architecture where the whole process was done using STL based unit cell models. After final design, the model was converted to STL files as a means of data transfer to RP machines for fabrication. This method has the following limitations as outlined below:

1. STL tessellation involves approximation of surfaces with triangular facets is incapable of representing the scaffold's micro-level pore feature sizes and intricate internal architectures. For example, as model precision demands become more stringent, the number of facets required to adequately approximate the model will increase. This usually ends up having computing inefficiencies with the STL file due to the extremely large file sizes. These STL files may also contain triangular facet errors which then will require file repair tools to handle them;
2. Database in the STL format cannot include other design intents within the model, for example, topology or internal material variations, and its spatial distribution etc.

3. Expensive computing power is required when the number of features and cuts in the scaffold become large enough to cause a memory overhead for the CAD software used.

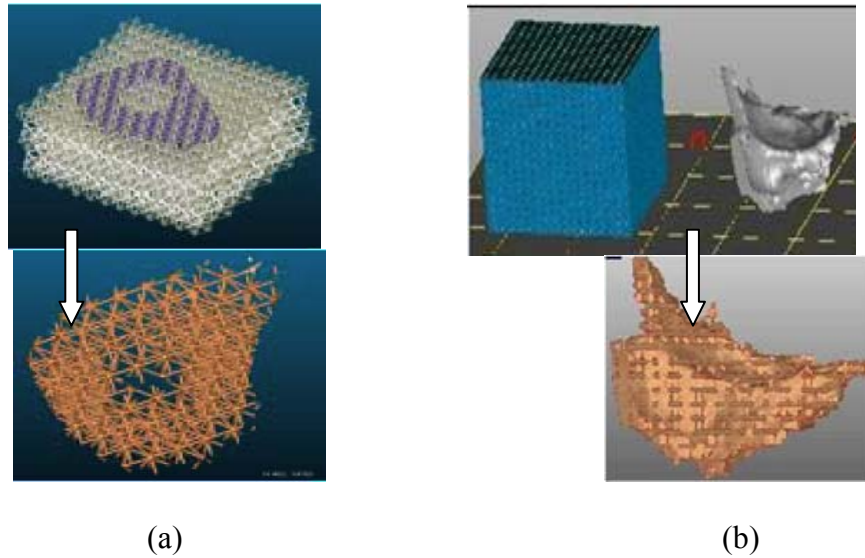


Figure 2.4: Interior scaffold design process

2.3.1 Unit Cell Design Methodology

Biological tissues are inherently heterogeneous structures. At the macrostructure level, tissue exhibits both morphological and mechanical heterogeneity and varies greatly at different anatomical and structural levels. For example, Figure 2.5 shows three different types of trabecular architectures as found at different anatomical sites in the human skeleton. In using feature primitive based CAD modeling approach, these architectures can be analogized by three different types of feature primitives: plate-like primitive (for femur), rod-like primitive (for spine), and hybrid primitive (for iliac crest). These primitives can in turn be represented by CAD unit cell solid models. These analogies are shown in Figure 2.6 [Folch et al., 2000].

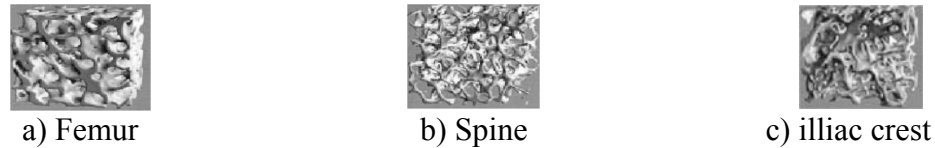


Figure 2.5: Variations of trabecular bone architecture

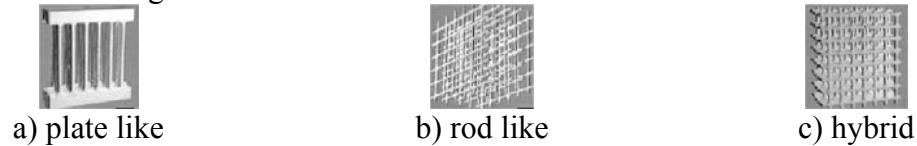


Figure 2.6: Analogized feature primitives

Using the feature primitive approach, each primitive discrete volume can be represented by a specific design feature, such as different internal architecture patterns used in common tissue scaffold design, for example, the standard weave, braided, and knit geometric feature of textile fiber patterns can be used as scaffold architectures or muscular pattern in soft tissues. Enabling computer-aided technology can then be applied to develop a CAD model based on information provided from the feature primitives, such as desirable feature patterns and architectures, desirable pores, pore sizes and shapes, and its distribution in the scaffold internal structure so that the required biophysical and biological design constraints can be met. A library of thus generated CAD-based unit cells derived from different feature primitive patterns can be generated and stored in a database for later retrieval. Sample unit cell architectures are presented in Figure 2.7. In this library, the individual unit cell is designed with different characteristics based on using different scaffolding material, feature primitive patterns, and the spatial distribution of scaffolding material to form unit cell internal architecture for porosity and pore interconnectivity considerations. With an appropriate selection of unit cells, one can design a customized heterogeneous tissue scaffold by tailoring unit cell properties, for example, using different feature patterns to design a specific porosity geometry (for pore

size and shape), arranging feature patterns in a specific 3D architecture to form a preferable pore distribution and interconnectivity (for cell growth and proliferation), and analyzing or simulating to verify if the designed model meets the scaffold strength and stability requirements (Griffith et al., 2002, Tran et al., 2004, Pirone et al., 2004).

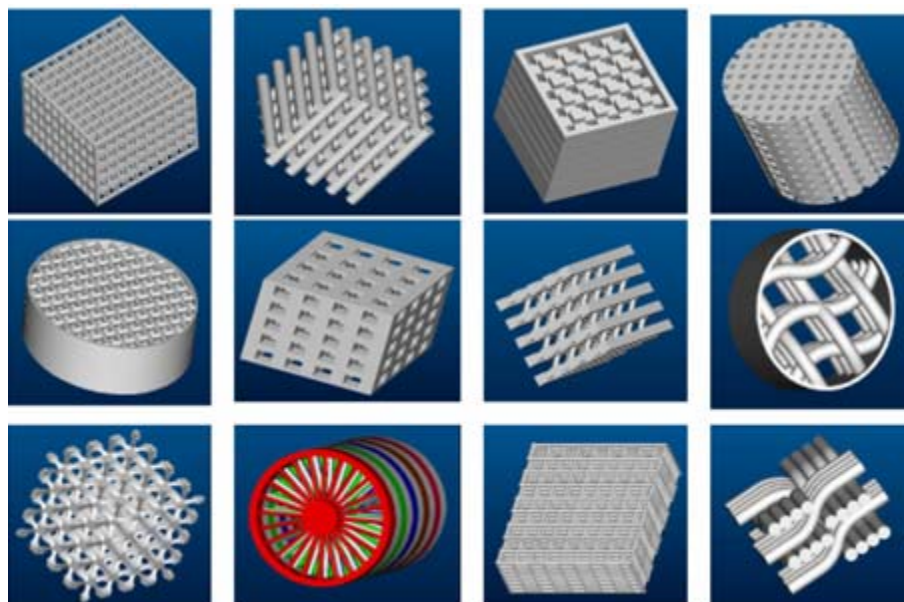


Figure 2.7: A library of designed scaffold unit cells based on different feature primitives

Most unit cell architectures shown above can be fabricated using SFF technologies that are based on the laser and printing technologies. The fast response mechanism for such systems allows material to be spatially patterned to form complex architecture. For extrusion based systems, only a certain kind of architectures can be fabricated since there is the response rate for a start-stop mechanism for the extrusion process is slow. The section below describes the use of space filling curves to design the internal architectures of scaffolds fabricated using extrusion based systems.

2.3.2 Space Filling Curves

In the previous section, a design technique that enables the design of interior architectures that could potentially mimic tissue structure using the unit cell design concept for SFF systems based on laser technology (example SLA, SLS) and printing techniques (example 3DP, TheriForm™) had been proposed. This design approach cannot be applied to extrusion based systems due to the nature of having the material extruded out through a nozzle.

Extrusion based SFF systems employ the extrusion of a biomaterial through a nozzle in a layer by layer technique. Each layer is composed of road patterns whose size, orientation and spacing can be controlled to achieve the desired level of porosity and strength characteristics. The first generation of extruded 3D scaffolds proved that cells prefer to attach themselves to the struts and grow along the orientation of the road patterns before they begin filling up pores to form an interconnected network of cell and extra cellular matrix [Zein et al, 2002, Wang et al, 2004].

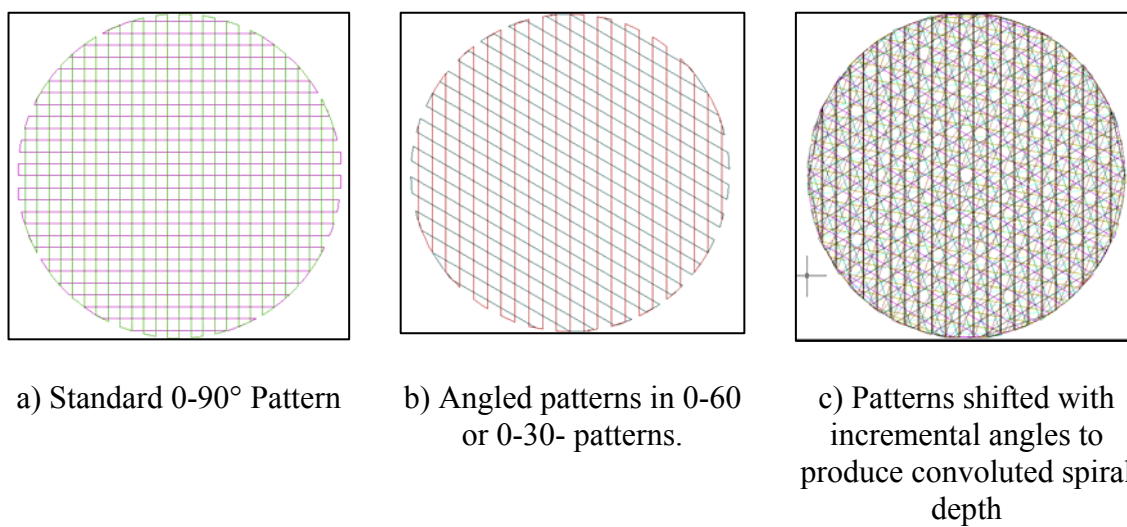


Figure 2.8: Standard 2D patterns currently produced by extrusion SFF systems

It is noted that the interior patterns themselves consisted of regular continuous road patterns whose parameters such as road width, road gap, slice thickness and orientation were changed to achieve the desired level of porosity and mechanical strength. Figure 2.8(a)-(c) shows some of the standard patterns that have been extensively used by investigators to produce the desired 3D pore structures [Moroni et al, 2004, Martina et al., 2005]. These structures were studied for its mechanical and biological properties with a variety of cell lines and have concluded that the effective mechanical properties of the porous composite scaffolds were a function of its porosity and biomaterial composition. They conclude that a higher surface area aids in faster cell growth due to better cell attachment and various configuration of patterns results in different transport characteristics. It cannot be concluded from such studies that internal patterns do not produce any significant change in cellular behavior. Different cell types behave differently in their microenvironment. For example, liver hepatocyte tissues are known for their highly organized hexagonal tissue structure and are known to organize themselves even without the presence of scaffolding materials. Therefore, there is a possibility that if the internal patterns can be arranged in a manner that can aid cellular organization, significant changes in cellular response will be obtained. We, therefore present in the following sections a family of curves that can be designed and varied to produce a whole new set of unit cell structures that can attempt to address cellular growth guidance in designed patterns.

Space filling curves are defined as curves that fill up the given space in a particular order by either continuously changing directions or passing through every

given point in the defined space [Hans, 1994]. The continuous functions that define these curves lie in the domain with a unit interval $[0,1]$, whose range lies in either the Euclidean 2-dimensional space (plane curves) or in the 3-dimensional space (volume curves). They have been extensively studied over the past century in fields of mathematics, information processing, database query, image compression. Examples of plane space curves are the Hilbert curves, Sierpinski curves, Peano curves and its different variations that have been formulated. We will limit our discussion to only plane space filling curves that satisfy the following constraints:

- a) Curves in a single layer do not intersect.
- b) Each point in the curve is a unique constant distance from each other.
- c) There is only one start and stop point of the curve in a single layer.

These three characteristics are particularly attractive for extruding polymer materials out of nozzles. The non intersecting feature allows patterns to be laid out in layer by layer fashion. The constant distance between points helps in easy characterization in terms of being able to define a unit cell that makes up the pattern. The single start and stop feature of the curves helps in preventing multiple closures of the valve in a single layer without the agglomeration of material due to delayed response times. The Hilbert and the Sierpinski family of space filling curves satisfy all of the above criteria and its design formulation is described below.

2.3.3 Hilbert Curve Patterns

The Hilbert curve was invented in the late 1890's by German mathematician David Hilbert and is perhaps the most popular of the space filling curves. The Hilbert

curve is constructed as follows. Consider the first curve shown in Figure 2.9(a), denoted as Level 1 Curve which is then replicated in every single line to form the Level 2 curve. The Level 2 curve can be considered to be the basic unit cell structure with each vertex away from each other by a constant distance. When moving to higher order levels from Level 2, the lower left quadrant is formed by rotating Level 2 curve anti-clockwise by 90° and the right quadrant by rotating it clockwise by the same angle. It is noted that the upper quadrants do not change their sense of orientation. These four quadrants together form Level 3 curve as shown in Fig 2.9(c). The process is repeated by selecting each Level 2 curve from the quadrant and performing the sequence of rotations. It can be noticed that the bounding box that encloses the curve remain the same and at each level the distance between the points gets progressively closer.

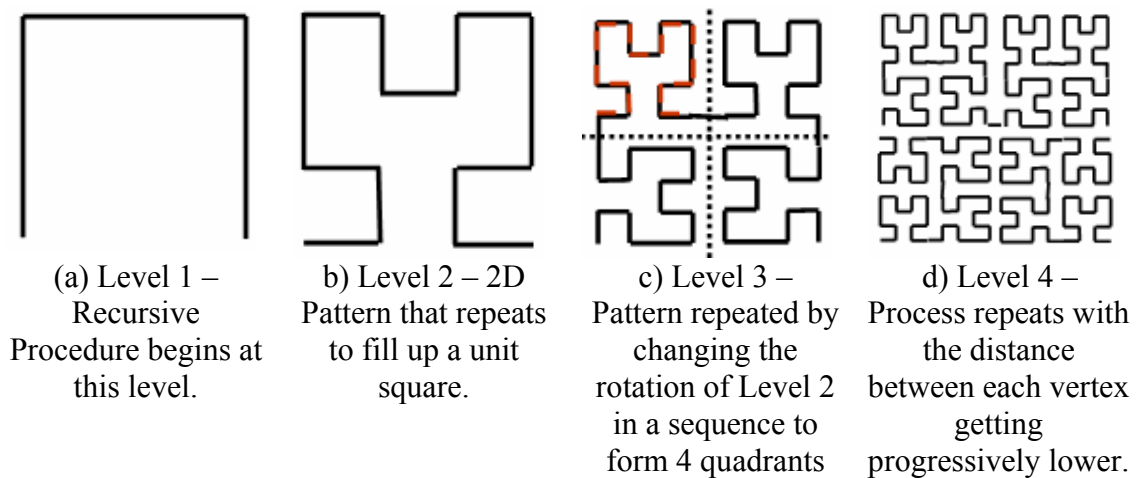


Figure 2.9: Hilbert curve recursive generation process

These curves can be used to construct the unit cell patterns required for scaffold design. Figure 2.10(a) represents the basic structure of the Hilbert curve pattern, while Figure 2.10(b) depicts the entire tool path pattern used to create the scaffold. The surface

area of these structures is similar to any ordinary 0-90° pattern, but the spatial distribution and orientation of the struts differs in regular patterned manner. The porosity of the unit cell structure can be calculated using the following relation:

$$P = 1 - \frac{\pi d}{3.428L} \quad (2.1)$$

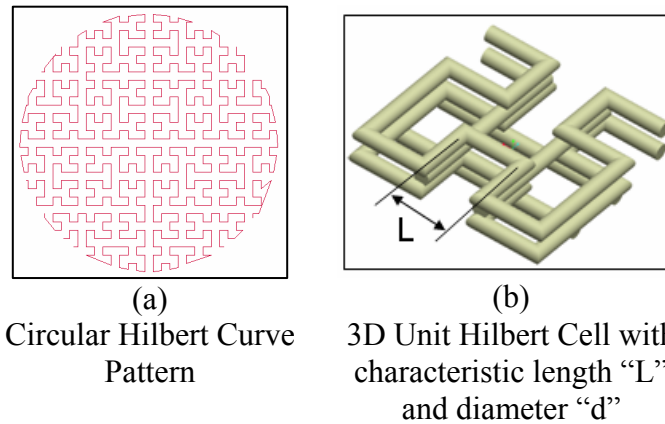


Figure 2.10: Scaffold structure with the Hilbert pattern

2.3.4 Sierpinski Curves Patterns

The Sierpinski curves were invented in the early 1900’s by Polish mathematician Waclaw Sierpinski. These curves begin with Level 1 shown in Figure 2.11(a) constructed together by four orientations of a three part curve. The second level is constructed by similar orientations of the 15-part curve and then connected together with short line segments. Each resulting pattern is a closed figure whose area is equal to 0.448 times the enclosing square bounding area [Wells 1991, Cundy and Rollett 1989]. Since the generated pattern is a closed figure, both the start and end point of the curve will be the same point during fabrication phase. Level 3 and higher orders can be produced in a similar manner.

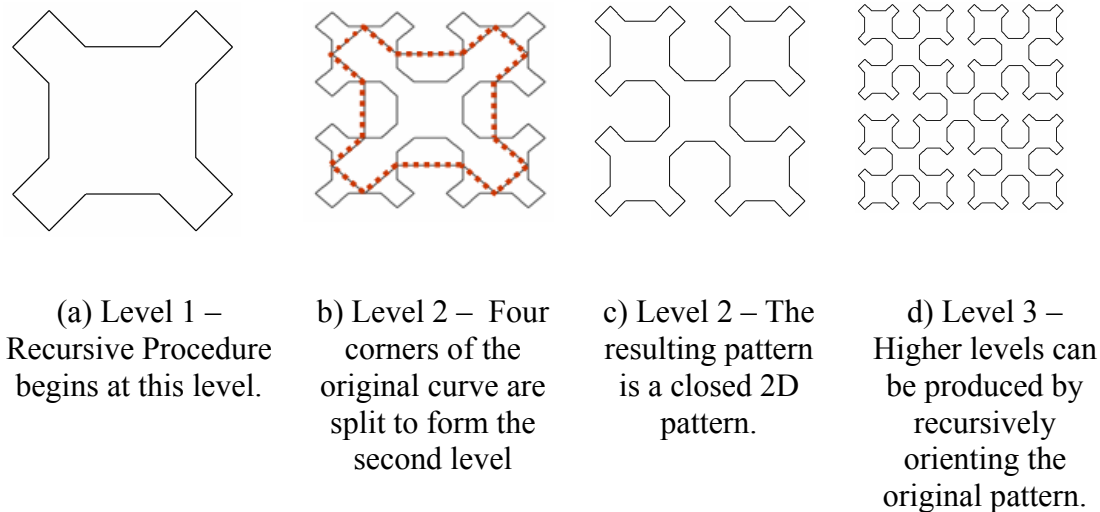
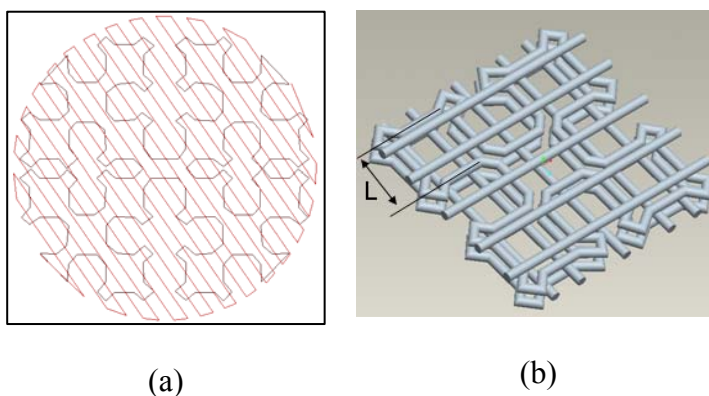


Figure 2.11: The Sierpinski curve at Levels 1, 2 and 3

Using these patterns, scaffolds with interior structure consisting of alternating straight curves and Sierpinski curves can be produced as shown in Figure 2.12. The porosity of the unit cell structure can be calculated using the following relation:

$$P = \frac{25\pi d}{128L} \quad (2.2)$$



Circular Sierpinski Curve Scaffold Structure

3D Unit Sierpinski Cells with characteristic length "L" and diameter "d"

Figure 2.12: Scaffold structure with the Sierpinski pattern

2.4 Effective Young's Modulus and Tortuosity Characterization

Tissue scaffolds designed for any application must be characterized in order to produce structures that are optimized, structures that can be reproduced accurately, be able to quantify batch variations and provide criteria for quality control and specification. Porous structures are generally characterized by their porosity, pore distribution and tortuosity factors which in turn determine the effective mechanical properties and transport characteristics of the scaffold. Traditionally, they have been studied using techniques such as the mercury intrusion porosimetry [Hu et al., 2002, Safinia et al., 2006], scanning electron microscopy [Choi et al, 1999], mechanical testing [Zein et al, 2002, Wang et al, 2004], optical microscopy etc. for scaffolds that have been produced using chemical methods of fabrication. These techniques are often destructive and hence do not provide a direct accurate estimate of the structural properties, but nevertheless they are capable of estimating properties at high resolution. However, with the use of SFF as the primary fabrication method, the virtual CAD model of the scaffold can be used for structural characterization using analytical or numerical schemes. Such characterization tools can estimate certain characteristic properties of the unit cell nature. Since these unit cells are sufficiently repeated within the structure, the global properties of the scaffold can be estimated by predicting the properties of the unit cell that makes up the structure. Hence the unit cells by themselves can be used as templates for characterization studies, namely predicting the effective Young's modulus and the effective tortuosity. Both of these structural parameters influence the overall mechanical and diffusion properties of the scaffold respectively and have been described below.

2.4.1 Mechanical Characterization: Effective Young's Modulus, E_{eff}

For load bearing tissue engineering applications, the implanted scaffold must have structural properties similar to that of the replaced tissue thereby matching the mechanical properties of the surrounding implantation site. This helps to minimize stress shielding effect as most commonly observed when metals such as titanium, chrome and stainless steel are implanted into the body. It is important to realize actual bone properties, for cases of further research study and to quantify the structure-function relationship that exists within the hierarchical structure in bone. The bone property realization would then be helpful in understanding fracture studies and for the prevention of fracture risk in cases of senile, postmenopausal or other genetic diseases. The property that is most often characterized with respect to bone is the bone density or the bone mass because this is directly related to the compressive strength of bone which then determines how susceptible bone is to fracture. Two general approaches are available to determine the bone properties i.e. density: 1) Invasive methods 2) Non- invasive assessment. Invasive methods were used in the early 1960's during the early research periods when machined bone specimens were taken and tested for its tensile, compressive and bending strength. However all of these initial investigations were in-vitro. During the early 1980's, non invasive methods of characterizing bone soon became popular due to the in-situ evaluation of bone properties and its potential in assessing bone fracture risk. Some of the non invasive methods include: X-ray, QCT (and pQCT) methods, Finite element methods, Photon absorptiometry methods, ultrasonic methods etc. Quantitative Computed Tomography is less affected by surrounding tissues and they do to an extent differentiate between cancellous and cortical bone. But they do involve high radiation

doses and may pose a health risk to the patient. However, the significant anisotropy of bone is not detectable in this application of QCT. Specific relationships between the QCT# and apparent density were suggested for human cortical and cancellous bone for different types of bones [Rosenthal et al., 1985, Bousson et al., 2006]. Their studies have concluded that a QCT assessment is not good for cortical bone as it yielded poor correlation coefficients while it is an appropriate method for cancellous bone property determination. Since cancellous bone is widely believed to be representative of bone mechanical properties, QCT method of evaluation has gained importance among researchers.

As described in Chapter 2, the region of interest is identified within the CT images and a 3D voxel model of the anatomic part under study is made. The segmented 2D image of a heterogeneous part like the femur bone is queried for its CT intensity values using image processing techniques. Using published literature values, these intensity values can be correlated to the density and Young's Modulus. As a first step, an appropriate threshold range was found that could best capture the relevant information contained in the femur. Using this threshold value, all pixels within this range were grown to a color mask and named accordingly. The segmentation was achieved using two different approaches. In the first approach, the whole proximal femur structure was grown into a single color mask representing the selected threshold range. With this approach, the average threshold value for the whole structure could be obtained. This average threshold value was in turn correlated to the quantitative computed tomography number (QCT#) represented in hounsfield units (HU) by using a simple relation as follows:

$$\text{QCT\#} = \text{Threshold Value} - 1024 \quad (2.3)$$

In the second approach, the femur structure was divided into layers and then an average QCT# for each layer found. A collection of slices of the femur was grouped as layers and segmented using different color masks. Each layer thickness was about 10mm and around 7 layers in all. An average QCT number was obtained for each layer in order to characterize the tissue heterogeneity (Figure 2.13). The QCT number retrieved from the appropriate layers is then correlated to the density of the bone by a linear interpolation using relations available in published literature. This density can in turn be then related to E, allowing the heterogeneous elasticity of the bone to be defined through the relations obtained as in [Rho et al., 1995, Rice et al, 1998].

$$\text{For QCT} < 816: \rho = 1.9 \times 10^{-3} * \text{QCT} + 0.105 \quad \text{and} \quad E = 0.06 + 0.9 * \rho^2 \quad (2.4)$$

$$\text{For QCT} > 816: \rho = 7.69 \times 10^{-4} + 1.028 \quad \text{and} \quad E = 0.09 * \rho^{7.4} \quad (2.5)$$

The structural heterogeneity of the bone can thus be defined through the associated bone Young's modulus. The characterization results are as shown in Table 2.2. The last row in the table indicates the QCT# retrieved when a single color mask was considered. The calculated E is in accordance with published data for cancellous bone- 0.5-1.5GPa. It is important to note that both cancellous and cortical bone have been considered smeared together as one structure in each layer and hence the slightly higher values obtained by this technique.

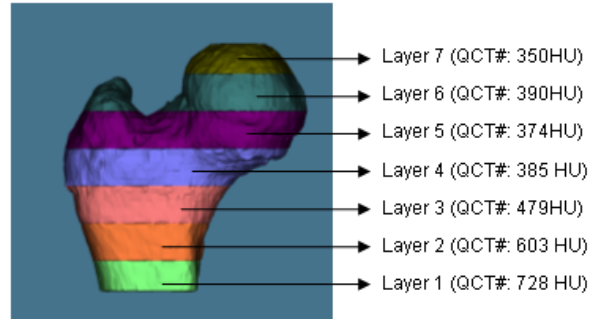


Figure 2.13: Average QCT Values Measured from CT

Cellular scaffold unit cells with varying porosity and internal architectures can provide tailored mechanical and biological properties. A feature primitive approach is utilized in which each primitive discrete volume is represented by a specific design feature, such as different internal architecture patterns used in common tissue scaffold design. We further use the concept of feature patterns derived from unit cells to design desirable interior pore architecture, pore sizes and shapes, and its distribution in the scaffold internal structure so the required mechanical and biological conditions can be met. We then select the specific feature primitive as the unit cell internal architecture according to the required mechanical or biological functions, and use the heterogeneous CAD modeling approach to construct unit cells for bone scaffold. Candidate CAD-based cellular unit cell structures that could potentially be matched up with the tissue structure are shown in Figure 2.14. A finite element method (ABAQUS) was then used to predict the unit cell effective mechanical properties as shown in Figure 2.15 for the unit cell with characteristic geometrical parameters (Fig. 2.15a), along with its applied boundary condition (Fig. 2.15b), and the contour plot of the reaction force (Fig. 2.15c).

Table 2.2: Bone Spatial Heterogeneity -7 layer model

Layer #	QCT#	Density (g/cu cm)	E (MPa)
Layer 1	728	1.4882	2053
Layer 2	603	1.2507	1467
Layer 3	479	1.0151	987
Layer 4	385	0.8365	690
Layer 5	374	0.8156	658
Layer 6	390	0.846	704
Layer 7	359	0.7871	617
Whole Layer	474	1.0056	970

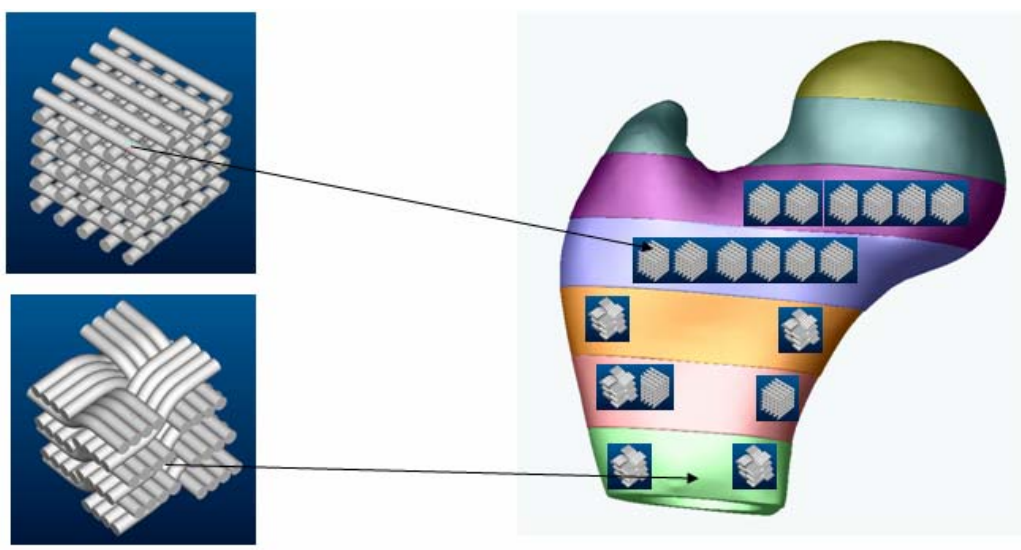
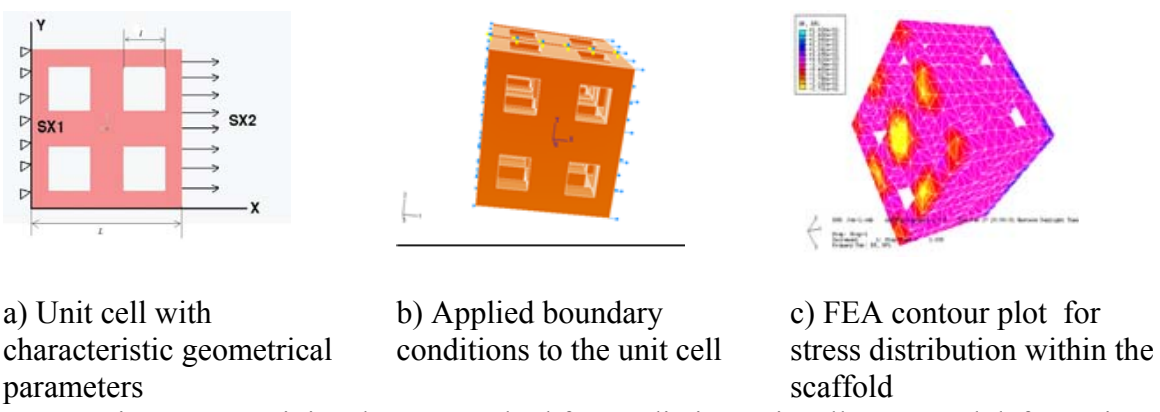


Figure 2.14: Samples of the designed scaffold unit cells



a) Unit cell with characteristic geometrical parameters

b) Applied boundary conditions to the unit cell

c) FEA contour plot for stress distribution within the scaffold

Figure 2.15: Finite element method for predicting unit cell stress and deformation

The geometry of the unit cell used in the finite element analysis is defined as a 4.5 x 4.5 x 4.5mm block with 4 open pores on each face. This cellular-like scaffold unit cell model was generated by Pro/Engineer software, and converted to IGES format and then imported to ABAQUS for finite element analysis. The relationship of the porosity with the overall geometry of the unit cell for the homogeneous square unit cell with square pores, is determined by:

$$P = \frac{N\{L * l^2 * (f/2)\} - \{(f/2 - 1) * l^3 * N/2\}}{L^3} \quad (2.6)$$

where N is the number of the pores in the unit cell; f is the total number of faces that contain pores, L is the size of square unit cell and l is the size of pore (Fig. 2.12a). A total 8353 4-node tetrahedral elements were used in the finite element analysis. A schematic illustration of applying boundary conditions and loading conditions for calculating effective Young's Modulus E_{xx} is shown in Fig 2.15(a). The face given by S_{x1} is constrained in the x-direction i.e. $U_x = 0$ and the face given by S_{x2} is given a displacement of $U_x = 0.001L_x$ which is equivalent to $\epsilon_x = 0.1\%$ where L_x is the length of the face. This boundary condition is intended to obtain a uniform displacement field throughout the model in the x- direction thus enabling us to calculate the effective E in the x –direction, E_{xx} . The effective Young's modulus of the cell can then be obtained by using the relation as given below

$$E_{XX} = \frac{\sigma_X}{\epsilon_X} = \frac{\left(\frac{R_X}{A_{SX2}}\right)}{\left(\frac{U_X}{L_X}\right)} = \frac{R_X}{0.001 * A_x} \quad (2.7)$$

where A_x is the area of cross section of the face S_{x2} and R_x is the average reaction force on the surface S_{x2} . Since the unit cell is symmetric in the x , y and z directions, we obtain $E_{xx} = E_{yy} = E_{zz} = E_{\text{effective}}$. Summary of the results predicted by finite element method for scaffolds with varying porosities at 26%, 41%, 59%, 76% and 83% levels for three different biomaterials: Hydroxyapatite, L-PGA and L-PLA, is presented in Table 2.3 and further plotted in Figure 2.16.

Table 2.3: Summary of results obtained by FEA analysis

Material	Young's Modulus, E	Effective Modulus of Unit cell at different porosity levels				
		26 %	41 %	59 %	76 %	83 %
Hydroxyapatite	2.0 GPa	1.362 GPa	0.9 GPa	0.6734 GPa	0.328 GPa	0.2764GPa
L-PLA	2.7 GPa	1.7466 GPa	1.2564 GPa	0.909 GPa	0.44 GPa	0.375 GPa
L-PGA	4.1 GPa	2.652 GPa	1.7466 GPa	1.38 GPa	0.673 GPa	0.567 GPa

From the QCT characterization of the proximal femur, the bone Young's modulus varies from 0.6 to 2.0GPa. From a biological point of view, we know that a desirable scaffold structure should have a porosity ranging from 55-70%. In this regard, the unit cell made of hydroxyapatite material with 59% porosity and effective Young's modulus of 0.6734GPa barely meets both biological and mechanical requirements. L-PLA-based unit cells with around 40 - 60% porosity do give a better option as a scaffold material for the proximal femur. Candidate unit cells can then be selected from the predicted curves shown in Figure 2.16.

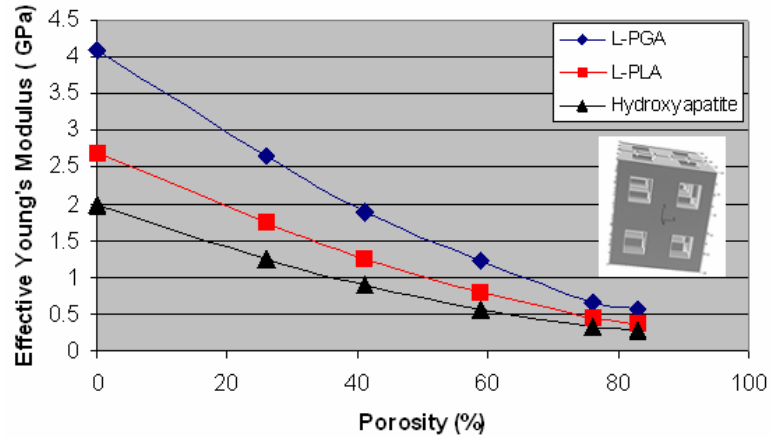


Figure 2.16: Effect of unit cell material and porosity on unit cell mechanical properties

Once the appropriate unit cell has been identified with the matched porosity, interconnectivity, and mechanical properties, a contour bone structure reconstructed from CT/MRI images will be filled in with the selected unit cell architecture. Constructive heterogeneous solid geometry algebra [Sun et al, 2002] through a mapping procedure can be used to combine the unit cell architecture and the replaced bone anatomical structure to achieve the final shape of the replaced bone tissue scaffold. This process will be further explained in Chapter 4.

2.4.2 Diffusion Characterization: Tortuosity

Besides the pore characteristics and its effect on mechanical properties, tortuosity of the scaffolds plays a major role in tissue growth and proliferation [Karande et al., 2004]. The transport properties of the designed scaffolds are based on the degree of tortuosity which determines the resistance to the transport of fluid molecules (nutrients and oxygen) through the scaffold. Tortuosity is defined as the ratio of the shortest

distance taken by the fluid particles (L_0) to the shortest straight line (L) that connects the entry point to the exit point as given by equation 2.8 and shown in Figure 2.17.

$$\tau = \frac{L_0}{L} \quad (2.8)$$

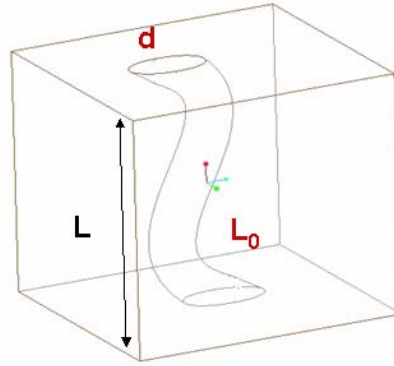


Figure 2.17: Tortuosity Definition

Several authors in their studies of porous structures have expressed this parameter based on the diffusion rates of molecules within the structure [Wakao et al, 1962, Botchwey et al., 2003, Hrabec et al., 2004, Knackstedt et al., 2006] as given by the following equation

$$\tau = \sqrt{\frac{D}{D_e}} \quad (2.9)$$

Where D = Diffusivity of molecules in bulk, D_e = effective diffusivity. The factor calculated from this expression, however, cannot be used to fully describe the nature of the tortuous effects within the structure and is applicable to symmetric architectures since it gives us a general picture of the tortuosity within the model.

From the generally accepted definition, it is clear that for a heterogeneous structure, one factor alone cannot be used to describe the nature of tortuosity. To obtain a

more realistic value for the degree of tortuosity in a 3D scaffold structure, an algorithm is developed to calculate three tortuosity factors to describe the level of resistance in the 3 principal axes of the model based on a Cartesian coordinate system. These factors are determined purely from the geometric nature of the model calculated by finding the distance a particle will travel from entry to exit. The steps to calculate the tortuosity factors are as described below and displayed graphically in Figure 2.18:

1) The 3D volumetric unit cell assembly, V , is sliced at regular intervals into layers using an image extraction process, and stacked upon each other to obtain binary sliced images of the model. This sequence is defined by the slice thickness parameter, h which is used to decompose the 3-dimensional volume, V . A finite discontinuous voxel set C is introduced to indicate the discrete image layers into which V is decomposed:

$$C = \left\{ c_k : a \leq c_1 < c_2 < \dots < c_{k-1} < c_k < c_{k+1} < \dots < c_n < c_{n+1} \leq b, k = 1, 2, \dots, n \right\} \quad (2.10)$$

where, the subscript k represents the number of the k th decomposition in a total n sliced layers, and constants a and b represent the values of lowermost and uppermost sequence respectively for a particular object V . Each voxel in C will contain a value of either 0 to indicate a pore or a value of 1 to indicate the solid material.

2) One face of the model is selected as the entry face and tracers are defined at the entry face, for example, voxels at $z=0$ plane are initialized as input tracers and allowed to propagate through the model in a preferred direction, in this case the positive z -direction. A tracer, τ continues to move along the z direction as long as it travels along a pore voxel

(0). If it encounters a voxel with value 1, a side step is taken, defined by an 8-level voxel neighborhood connectivity criterion as follows:

$$N_8(\tau) = \{(x+i,y), (x-i,y), (x,y-i), (x,y+i), (x+i,y+i), (x+i,y-i), (x-i,y+i), (x-i,y-i)\} \quad (2.11)$$

Where ($i = 1, 2, 3 \dots$). Each alternate step from the current position $\tau(x,y)$ is traversed in the order given and checked to see if a pore voxel is met. If it cannot find a pore voxel, after cycling through all of its nearest neighbors ($i=1$), “ i ” is incremented to increase the search neighborhood. The value of “ i ” is allowed to increment until the search neighborhood has met the outer bounds of the model or if a pore voxel is reached. If it cannot find a pore voxel within its search neighborhood, it is classified as a dead pore and the search is abandoned.

3) The process is repeated for all tracers on the plane $z=0$. The distance traveled by all the tracers given by the distance metric (city block distance [Ramaswamy et al., 2004]) is calculated and divided by the shortest length from the tracer entry plane to the exit plane. The average tortuosity is then easily determined in the z (T_z) direction.

4) Similarly, tracers are allowed to propagate from the planes ($x=0$ and $y=0$) and Steps 1-3 are repeated to obtain T_x and T_y respectively for any given unit cell assembly model.

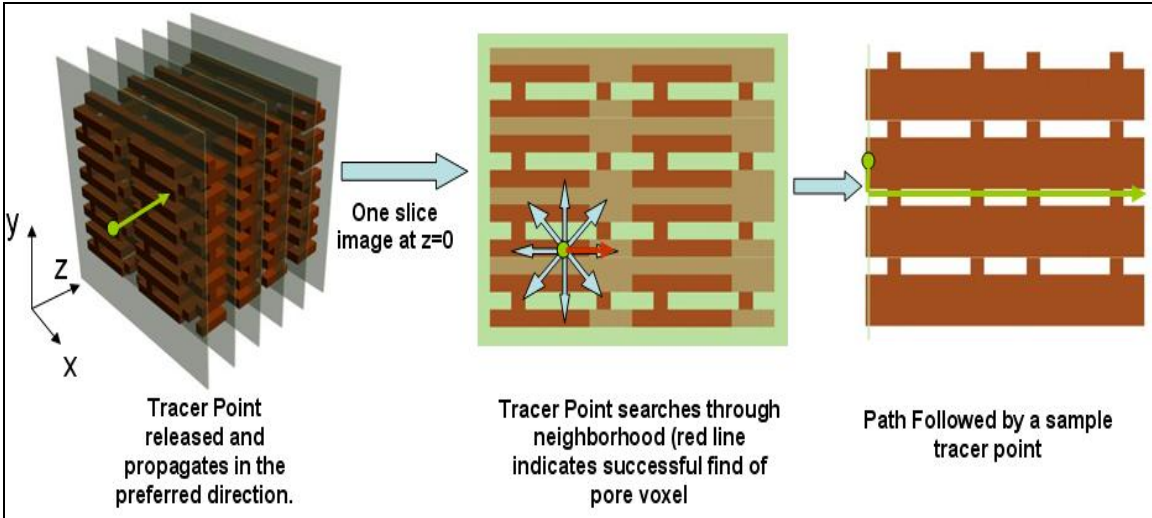
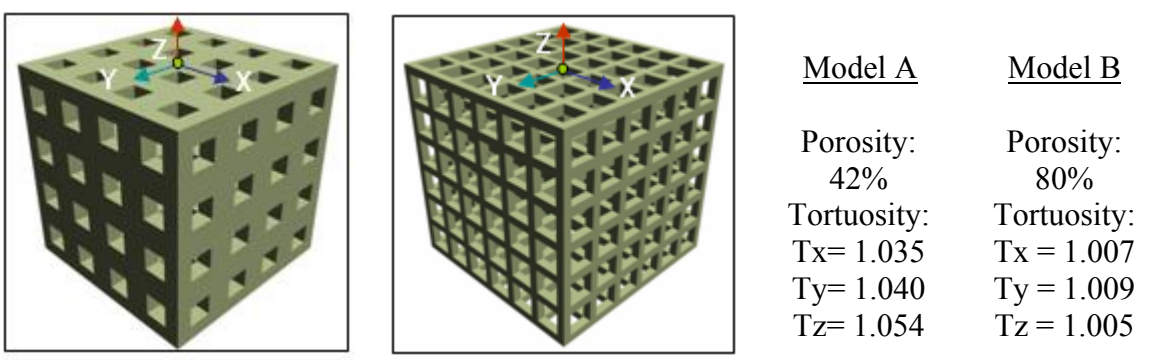


Figure 2.18: Tortuosity Measurement using Tracer Distance Metric Analysis

Tortuosity prediction has been performed for different unit cell patterns as shown in Figure 2.19. As expected, tortuosity is inversely proportional to the porosity of the model. Two unit cell structures of the same porosity can have different values of tortuosity as shown in Figure 2.20 which indicates that tortuosity also depends upon the geometric structure of the model which can be symbolically represented as the formation factor, “F”.

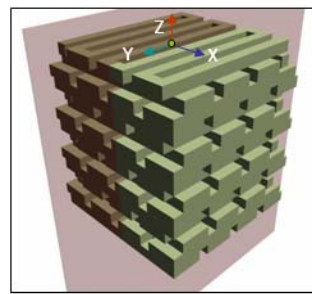


Model A

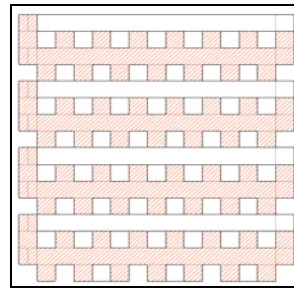
Model B

Tortuosity Comparison

Figure 2.19: Two Models with different porosity but same rectangular pore shape having different tortuosity factors.

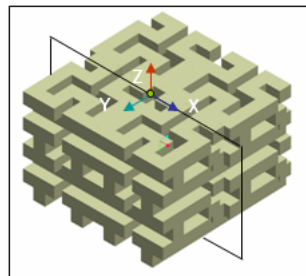


(a) Model C

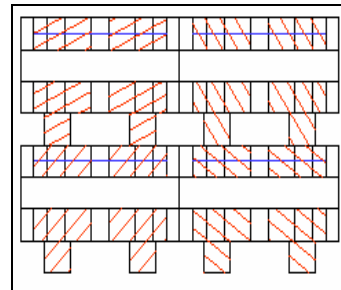


(b) Sectional View of Model C

Tortuosity: $T_x = 1.21$, $T_y = 1.35$, $T_z = 1.11$



(c) Model D



(d) Sectional View of Model D

Tortuosity: $T_x = 1.091$, $T_y = 1.035$, $T_z = 1.206$

Figure 2.20: Two models with constant porosity of 48% but different tortuosity factors due to the difference in formation factors.

In Figure 2.20, it is clear that for Model C, the transport of nutrients would take place faster in the z-axis than the x and y axis due to lower tortuosity. However, in the case of Model D, the tortuosity in z-axis is much higher than x and y axis directly indicating that proliferation rates in z-axis will be lower compared to rates along the x and y axis. By being able to selectively design the tortuosity factors in the three principal axes, directed cell growth and proliferation can be attained since the faster permeation of nutrients in a preferred direction is directly correlated to higher cellular proliferation rates. Selecting unit cell architectures in a scaffold that have varying degrees of tortuosity can also help us to understand the role played by the transport of nutrients on cellular activity as shown by Figure 2.21.

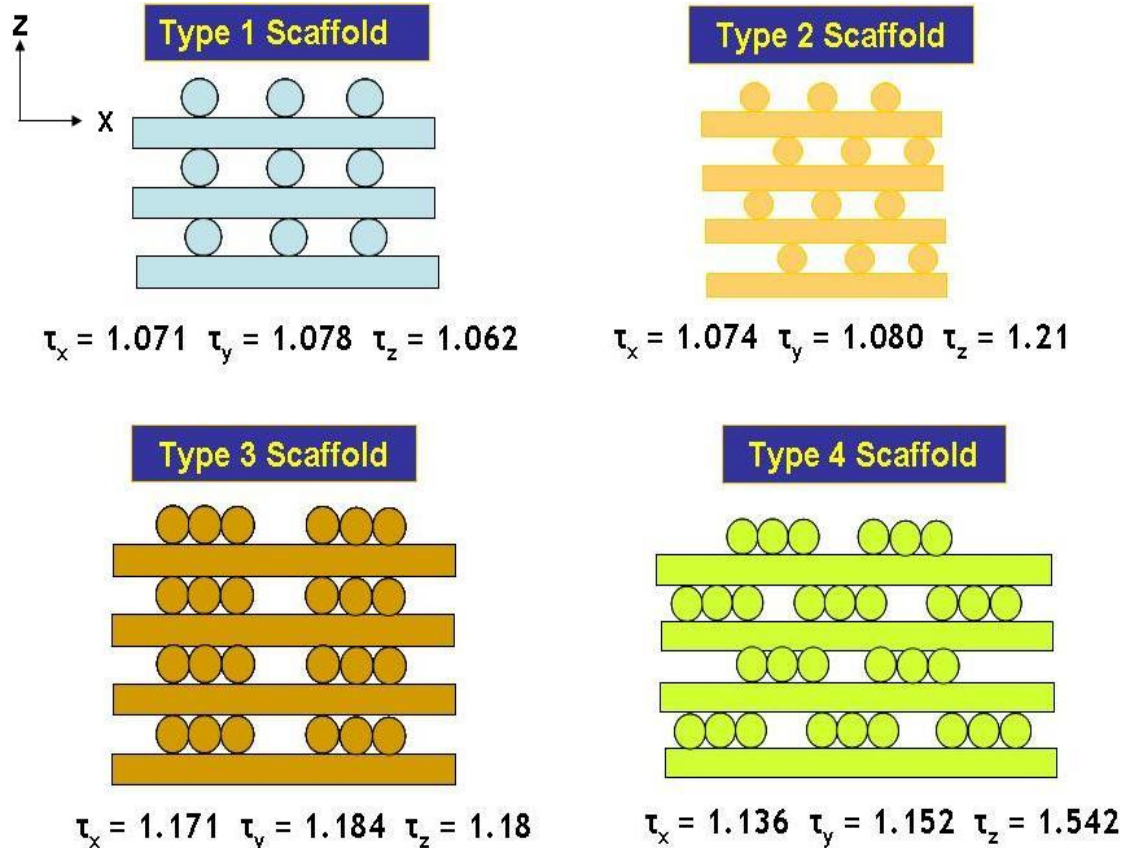


Figure 2.21: Four types of scaffolds with varying tortuosity particularly in the z-axis

2.5 Conclusions

The research work outlined here have explored the bioengineering application of reverse engineering (RE) technology in converting CT/MRI based images to CAD models and have brought forward different process paths in which this can be achieved. Each process path selected depends on the particular application it is intended for. The MedCAD process path would be suitable in the generation of surface models or models that have less overall complexity. The Reverse engineering interface would be selected when a solid model needs to be made and which would be used for further CAD based

analysis such as FEA. An iterative process of refining the surface may need to take place since mesh generation can fail in certain cases depending on the complexity of the outer surface. The STL interface is preferred when a rapid prototype of the model is needed for surgical planning or anatomical display. These Bio-CAD models can also be used for dynamic simulation to help in a better understanding of the biophysical property of the model under study. The developed approach would benefit in the efficient design of prostheses and implants. By working on actual rather than computational models, patient specific implants and prostheses can be designed that would last longer and be more comfortable.

This approach can aid in the development of biomimetic bone replacement substitutes which would be used in the design of heterogeneous scaffold structures. The CT/MRI image based reconstruction provides a technique in which the outer shape of the scaffold structure can be retrieved for appropriate anatomical fitting and compatibility. By selecting the appropriate unit cell interior structures, properties such as the effective mechanical properties, diffusion and permeability characteristics can be designed and controlled. Depending on the fabrication method used, varying complex internal patterns can be fabricated. In this section, we have presented space filling curves and heterogeneous patterns that can be fabricated by extrusion based SFF systems. Such interior architectures are extremely hard to fabricate in printing based technologies due to limitations of CAD software capability. Architectures that are possible in extrusion based SFF systems may not be able to be fabricated in printing based technologies and vice versa. The designer will have to keep this in mind before the design of such scaffolds for tissue engineering applications.

Through the use of numerical techniques, the effective mechanical properties of the unit cell architectures can be calculated and hence the global mechanical properties of the scaffolds can be estimated. Other numerical schemes such as the homogenization theory [Fang et al., 2004] can also be used in the prediction of the effective mechanical properties. Once the unit cell properties are known, they can be used as design criteria during the selection of the unit cell to fit within a scaffold assembly. We have also presented an algorithm to calculate the degree of tortuosity within a unit cell assembly. By being able to estimate the properties, it would be possible to predict the permeability and growth kinetics of cellular proliferation.

CHAPTER 3 : DIRECT SLICING FOR FREEFORM FABRICATION OF TISSUE SCAFFOLDS

3.1 Introduction

The growth of solid freeform fabrication (SFF) or layered manufacturing (LM) in biomedical applications has created the need for better technology in terms of model representation, accuracy and functionality [Marsan et al., 1998]. SFF models in medicine have been used mainly for assisting diagnosis, surgical planning, and manufacture of orthopedic implants. However, the technology has recently seen applications in the field of tissue engineering specifically in the fabrication of tissue scaffold structures. Traditionally, LM process involves the conversion of the 3D models into **STereoLithography** (.STL) format, a tessellation procedure where the model is approximated by triangles, sliced and then fabricated by the machine. The procedure worked well in the manufacturing industry which used RP to evaluate product designs and aesthetics by producing actual prototypes of the proposed design. However, the geometric description used to represent solid CAD objects significantly affects the accuracy and quality of the final parts produced especially in the case of freeform shapes. This is particularly relevant in the field of computer aided tissue engineering which involves the use of these freeform shapes to model the external shape of the scaffold that intends to replace actual body sections [Sun and Lal, 2002]. The complexity of the internal and external shape of these scaffolds [Sun et al, 2004, Hutmacher et al., 2004] requires a more direct method in conversion of CAD data to process planning instructions. The process of tessellation and representation in STL format is inadequate for designing biomimetic scaffolds with complex internal architecture. This is due to the

large number of triangles required to represent small features in the scaffold which results in failure during the conversion process. Direct slicing of CAD models without the intermediate .STL format is preferred because it helps keep the geometric and topological robustness that the original data have and no intermediate conversion process is required.

3.2 Conventional STL Based Slicing

Slicing is defined as the procedure to convert the CAD model to a layer by layer instruction file set to drive RP/SFF systems. The current industry standard of importing CAD models into RP software is through the conversion of the CAD model to a triangular mesh file using an available tessellation algorithm. The triangulation process converts the surface of the CAD model to triangular facets and the tessellated model is then written to the .stl format and then sliced to enable SFF machines to fabricate the model.

What is Tessellation?

This process involves approximating 3D shapes with a carpet of planar triangular patches. The triangular facets approximate the surface of the CAD model and are then used in the slicing procedure to calculate the layer by layer contour information. The contours are obtained by calculating the intersection points between a plane and the triangles. The use of triangles simplifies the procedure of slicing. Most CAD systems have implemented STL format conversion algorithms and has become the current de-facto data exchange standard to SFF systems. During the tessellation procedure, an “accuracy or offset parameter is input by the user, which is the defined as the acceptable

chordal error (cusp height as shown in Figure 3.1 between the approximating plane of a triangle and the surface of the CAD model. For example in a cube, the cusp height will be zero. In the case of a sphere, the lower the cusp height, greater is the accuracy of the fabricated model but which leads to larger file sizes. CAD models that have complicated curved surfaces can easily generate STL data about 100 times the size of the CAD file. Hence the use of the cusp height must be decided with precaution.

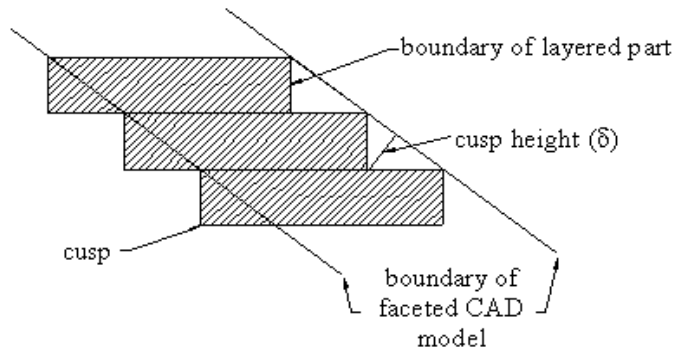


Figure 3.1: The cusp height on faceted surfaces

The advantages of tessellation include:

1. A simple method of slicing since it involves relatively simpler equations of planes and triangles.
2. It's a standard used by most RP machines and therefore universal.
3. For CAD models that make use of simple geometrical entities such as lines, rectangles, circles, arcs, it can provide small and accurate files for data transfer.

Some of the disadvantages with tessellation include:

1. The file sizes can potentially be huge, many times larger than the original CAD file for a given accuracy parameter due to the redundancies present in an STL file during triangular representation.

2. There are instances when the tessellation procedure fails that leads to degenerate triangles. Specialized repair software algorithms are required to fix such STL files.
3. Staircase effect for models which is an inherent defect in RP models is more pronounced through the use of triangulated files especially in models with a high degree of curvature.

In light of these disadvantages, researchers have looked into methods in which tessellation procedures are not required for slicing. Instead of using the tessellation process, research was carried out to slice the CAD models directly and then transfer the resulting contours to the RP machine. This process came to be known as the ‘Direct Slicing’ approach. While considerable amount of work has been done in the slicing of STL format files [Chalasanani et al., 1991, Dolenc et al., 1992, Cha Soo-Jun et al., 2002], direct slicing approach still needs to be developed especially in light of the continued development and advancement of rapid prototyping in the medical industry.

3.3 Direct Slicing of STEP Based NURBS Models

Accuracy was not a significant issue in the early days of RP since the parts could only be used for prototyping and design verification purposes. However, improving the accuracy of an RP part has become the focus of the RP community under the increasing need for prototyping functional parts with engineering properties and dimensional tolerances comparable to parts produced conventionally [Guduri et al., 1992, Bablani et al., 1995]. Direct slicing is an approach that can address this issue since it seeks to remove the drawbacks of the STL standard. The process involves the direct calculation of the slice contour using the exact mathematic equations used to represent the CAD model.

Although this may appear to be computationally expensive due to a number of feature primitives available, there are ways to get around this by expressing the entire CAD model in a common base format.

The field of direct slicing for layered manufacturing (LM) has been researched on since the middle 1990s. Some of the earliest works were applied to traditional industrial applications and did not focus on medical prototyping applications. Jamieson and Hacker have developed an adaptive direct slicing algorithm based on the Unigraphics slice modules which directly sliced models using a constant layer thickness [Jamieson et al., 1996]. Consecutive contours were compared for differences and if the error falls below a set value, they were accepted. If not, a middle slice is created and the process of comparison performed again. The procedure is repeated until the difference between any two consecutive slice contours is either small or the minimum layer thickness has been reached. Rajagopalan et al, have directly sliced NURBS based models in an I-DEAS based CAD system. The process relied on I-DEAS system functions to perform the slicing which made it package-specific. In a more recent study, an adaptive direct slicing algorithm that operates directly on NURBS based models to generate skin contours and then uses a selective hatching strategy to reduce the build time of the model [Ma et al., 1999]. All of the papers published above depend on external modeling packages to perform the slicing process which in turn limits the capability on the level of control and variety that can be achieved. Zhao et al in their work worked on an adaptive direct slicing approach independent of CAD vendors in which they make use of AUTOCAD API functions to perform the slicing operation. Using API functions does provide more

control but they have showed inappropriate slicing when applied to scaffolds with complex external shapes. Figure 3.2 shows a sample failure mode at a particular z-level during slicing of a sinus implant using the slice functions available from a major CAD vendor.



Figure 3.2: API slice errors from a major CAD vendor

Therefore the objective of this section of the thesis is to present a direct slicing approach that is independent of any CAD modeling package and that which makes use of the ISO format Standard for the Exchange of Product Data (STEP) as the starting input file of the model to be prototyped. The approach described here is feasible for both traditional manufacturing designs as well as for biomedical applications. We have currently focused on NURBS based freeform shapes to demonstrate the capability of the algorithm and the proposed methodology with regards to raster line pattern layout suited for the printing based SFF machines. However, the work can be extended to include contour slice patterns along with a hatching strategy depending on the applicable RP machine. A point that we would like to stress is that the proposed method in no way replaces the STL based method of indirect slicing which is more suited to traditional manufacturing components and that the use of the direct slicing approach is particularly well suited for freeform shapes that have complex outer geometry which in its STL representation carries drawbacks. Since the design of scaffolds for tissue engineering

applications involve complex outer geometrical shapes, the direct method of slicing would be more advantageous than the indirect method of slicing.

3.3.1 General Application Process Path

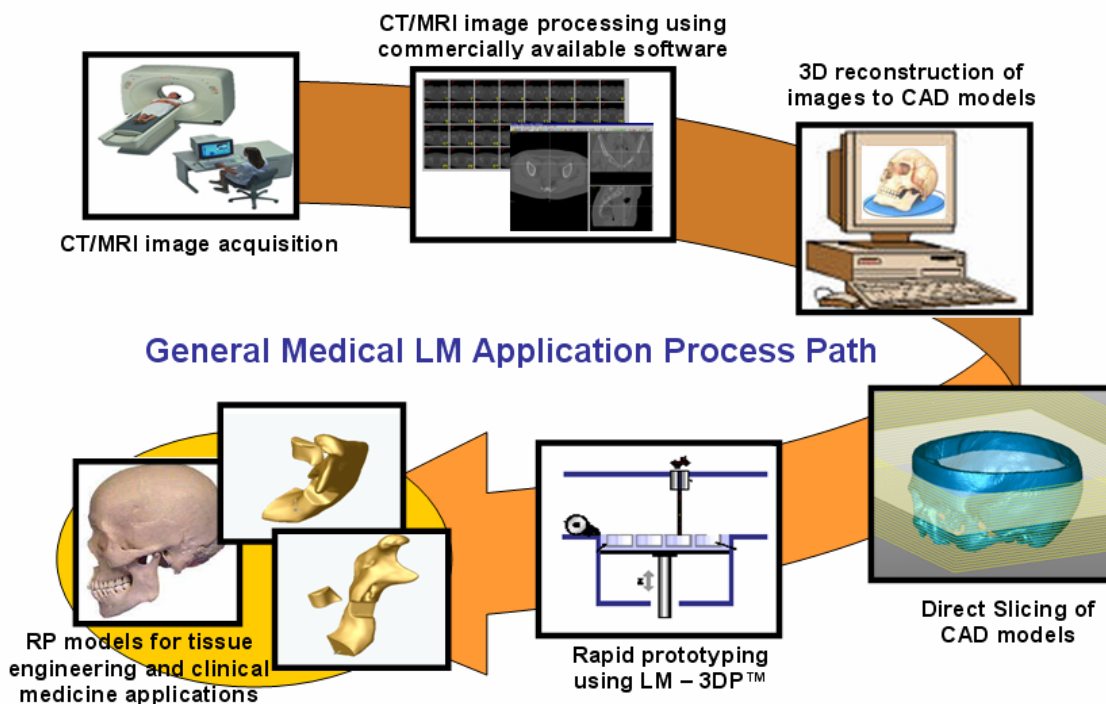


Figure 3.3: General Biomodeling and Medical Rapid Prototyping Process Path

As described in Chapter 2, the first step involves the acquisition of CT/MRI images of the bone under replacement. These CT images are loaded in commercially available image processing software to reconstruct them to CAD models through reverse engineering techniques. The CAD model is now sliced to generate process plan instructions for the relevant RP machine. The machine prototypes the required scaffold for the desired application. Although tissue engineering applications processes would involve more stages until final fabrication, the steps remain the same and a similar

process path needs to be followed. The following sections of this chapter will describe the conversion of CAD models to process planning instructions for the RP machine. Although, the conventional method is to first convert the CAD model to an STL based model, our effort is to directly slice the CAD model and transfer the information to the machine eliminating the need for the intermediate file format. The overall process path for a general medical rapid prototype production in building the external shape of a scaffold is as shown in Figure 3.3.

The process data flow is shown in Figure 3.4 that is implemented within a Fabrication Planning software framework. Initially, the CAD STEP file is input into the software framework wherein a STEP reader is implemented to extract out the model features. The B-rep features of the model are viewed using graphic kernels for easier manipulation and display. The model features in its NURBS representation is then transferred to the slicing module. Each cross sectional layer is then extracted from the model based on the slicing parameters and then converted to machine job instructions. A print job database is also maintained for database records and future retrievals.

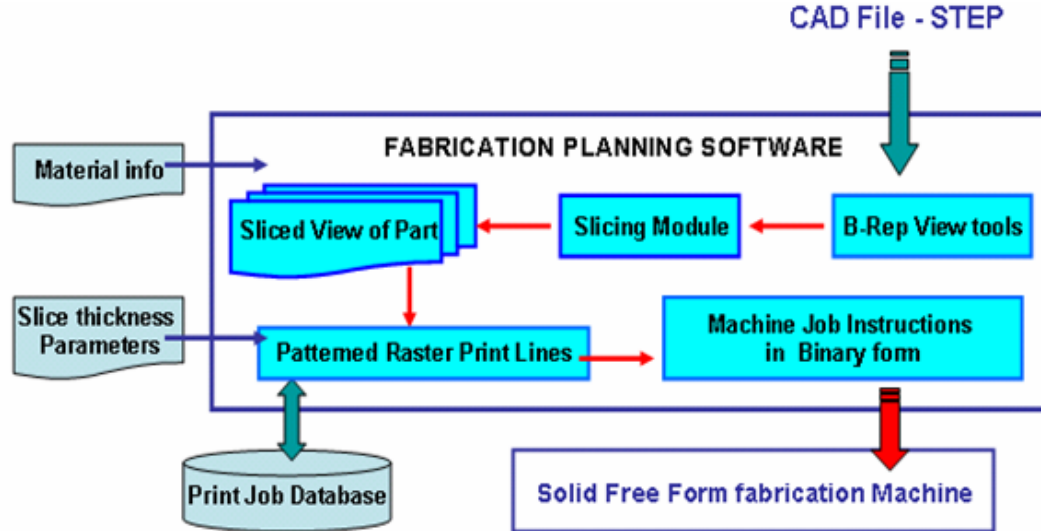


Figure 3.4: Data Flow during Fabrication

2.2.2 ISO 10303(STEP) Based NURBS representation

Non-Uniform Rational B-Spline (NURBS) are the industry standard tools for the representation and computer aided-design of freeform models [Piegl, 1997, Rogers, 2000] in the field of automotive design, ship design etc. Within STEP files, solid and surface models may be represented as rational or non-uniform rational B-spline surfaces. Unlike STL files where the facet information of the triangle is used to obtain the slice contour, direct slicing works by using the exact mathematical representation of the freeform shapes in computing the slice contours or tool patterns. A rational B-spline surface is expressed parametrically in the form,

$$S(u, v) = \frac{\sum_{i=1}^{n+1} \sum_{j=1}^{m+1} W_{ij} P_{ij} b_{ik}(u) b_{jl}(v)}{\sum_{i=1}^{n+1} \sum_{j=1}^{m+1} W_{ij} b_{ik}(u) b_{jl}(v)} \quad (3.1)$$

where parameters u and v range from zero to one, n and m the degree of the surface in u and v direction. The P_{ij} terms are 3D net control points of the control polygon and W_{ij} terms their corresponding weights, b_{ik} and b_{jl} are B-spline basis functions of order k and l respectively. The B-spline basis functions are defined by the Cox-deBoor recursion formulas as given by:

$$b_{j1}(s) = \begin{cases} 1 & \text{if } ku_j \leq u \leq ku_{j+1} \\ 0 & \text{otherwise} \end{cases} \quad b_{l1}(s) = \begin{cases} 1 & \text{if } kv_l \leq v \leq kv_{l+1} \\ 0 & \text{otherwise} \end{cases}$$

$$\text{and } b_{jk}(u) = \frac{(u - ku_j) b_{(j)(k-1)}(u)}{ku_{j+k-1} - ku_j} + \frac{(ku_{j+k+1} - u) b_{(j+1)(k-1)}(u)}{ku_{j+k+1} - ku_{j+1}}$$

$$b_{lk}(v) = \frac{(v - kv_l) b_{(l)(k-1)}(v)}{kv_{l+k-1} - kv_l} + \frac{(kv_{l+k+1} - v) b_{(l+1)(k-1)}(v)}{kv_{l+k+1} - kv_{l+1}} \quad (3.2)$$

where the values of ku_j and kv_l are defined by the knot vector associated with the NURBS surface in the u and v direction respectively. The STEP file contains all information that is required to define the NURBS uniquely and a STEP reader is employed to extract the relevant information. Figure 3.5 depicts the format of a B-spline description in an ISO10303 STEP file [Owen, 1997]. An ID is given to each control point as contained within the CARTESIAN_POINT statement. This is followed by the definition of the B-spline surface in terms of the parameters needed to define it – degree

of surface in u and v direction, multiplicities and knot vectors in u and v direction and the weight associated with each control point.

```
#Identifier ID =CARTESIAN_POINT(“ (x-coordinate, y-coordinate, z-coordinate));
.
.
#Identifier ID =(BOUNDED_SURFACE()B_SPLINE_SURFACE (degree_u, degree_v, ((control points
identifier IDs ),( ), ..UNSPECIFIED.,F.,F.,U.)B_SPLINE_SURFACE_WITH_KNOTS(( multiplicities in u),
(multiplicities in v), (knot vectors in u), ( knot vectors in v),. UNSPECIFIED.)
GEOMETRIC_REPRESENTATION_ITEM(), RATIONAL_B_SPLINE_SURFACE ((weights associated with
control points),(),...REPRESENTATION_ITEM(“)SURFACE()));
```

Figure 3.5: STEP description of a Uniform B-Spline surface

2.2.3 Direct Slicing of NURBS Surfaces Using Ray Casting

Central to the problem of slicing NURBS surfaces is the determination of intersection points between the slicing plane and the model. This problem has been researched by the computer graphics community with regards to ray-tracing of NURBS surfaces [Sweeney et al., 1986, Daniel et al., 1990,]. Ray tracing of free form surfaces are commonly used in 3D visualization of models and real time rendering of images. The basic approaches in most ray-tracing algorithms in the determination of the intersection points remain the same and only vary with regards to efficiency in terms of memory usage and the speed taken to ray trace a particular scene. Most freeform ray tracing algorithms have performed while tessellating the images to gain speed and reduce the complexity of solution. Several methods of obtaining ray-NURBS intersections have appeared in literature. Almost all of them involve some precursor method of divide and conquer before obtaining the roots of the intersection equation. Adaptive based subdivision [Sederberg et al., 1990] and curvature based subdivision processes [Martin et

al., 2000] serve well in dividing the model space into sub-patches. These sub-patches are then enveloped by bounding volumes to restrict the parameter domain in which the solution exists.

In our proposed methodology, we have used the same basic approach using the mathematical NURBS equations to solve for the intersection points. We have, however extended it to the slicing domain for use in the LM manufacturing scenario. The difference lies in the fact that in LM, intersection points both in the form of entry and exit points need to be determined along with the vector/raster layout pattern of the rays within the model. The raster pattern of the rays would involve connecting corresponding entry and exit points to define machine level instructions for layered manufacturing. Vector patterning on the other hand would involve connecting entry and exit points in such a manner that they form closed loops within the layer. These vector paths are then converted to machine instructions for fabrication. The core aspect of our approach is outlined in Figure 3.6. The NURBS surface is geometrically refined using an adaptive subdivision procedure to break them down into smaller domains of parametric values. Bounding boxes are then used to cover up the entire surface based on these smaller domains. The rays then shoot out intersecting the model at several boxes and for a box that is hit, a root finding procedure is initiated to converge at the intersection point. The procedure is repeated for all rays that are cast onto the slice plane and for every slice plane that intersects the NURBS model.

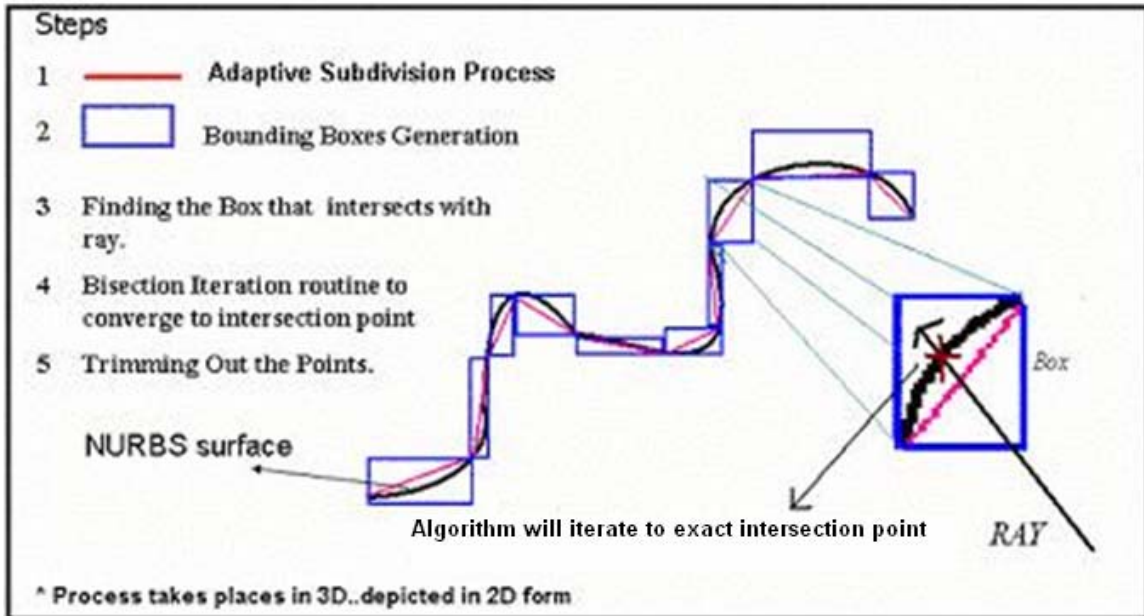


Figure 3.6: Step by Step procedure on calculation of NURBS intersection points

In the ray – casting approach, the bounding box of the model is first determined allowing the start position of the ray to be defined from any predefined corner of the box which then shoots out across intersecting the model. A ray is defined as having an origin ‘o’ and a unit direction vector ‘d’ and can be defined as:

$$r(s) = \hat{o} + s * \hat{d} \quad (3.3)$$

Using the method followed by Kajiya et al, the ray $r(s)$ can be rewritten as an intersection between 2 planes given by $\{p | P_1 \cdot (p, 1) = 0\}$ and $\{p | P_2 \cdot (p, 1) = 0\}$ where $P_1 = (N_1, d_1)$ and $P_2 = (N_2, d_2)$. The normal to the first plane is defined as

$$N_1 = \begin{cases} (d_y, -d_x, 0) \\ (0, d_z, -d_y) \end{cases} \quad \text{if } |d_x| > |d_y| \text{ and } |d_x| > |d_z|$$

$$N_1 = \begin{cases} (d_y, -d_x, 0) \\ (0, d_z, -d_y) \end{cases} \quad \text{if } |dx| > |dy| \text{ and } |dx| > |dz| \quad (3.4)$$

N_2 will always be perpendicular to the ray direction and the plane N_1 , hence

$$N_2 = N_1 \times \hat{d} \quad (3.5)$$

Since both planes contain the origin 'o', it can be deduced that $P_1(o,1) = P_2(o,1) = 0$.

Thus,

$$\begin{aligned} d_1 &= -N_1 \cdot \hat{o} \\ d_2 &= -N_2 \cdot \hat{o} \end{aligned} \quad (3.6)$$

An intersection point that needs to be calculated should satisfy the following two conditions,

$$\begin{aligned} P_1(S(u^*, v^*), 1) &= 0 \\ P_2(S(u^*, v^*), 1) &= 0 \end{aligned} \quad (3.7)$$

The above equation needs to be solved using numerical means and we have employed the Bisection Iteration routine to determine the values u^* and v^* that will satisfy (3.7) from the function as expressed in (3.8):

$$F(u, v) = \begin{pmatrix} N_1 \cdot S(u, v) + d_1 \\ N_2 \cdot S(u, v) + d_2 \end{pmatrix} \quad (3.8)$$

However, before the root finding operation begins, a number of pre-processing steps are performed. In the steps that follow, we explain the details regarding optimal orientation for the reduction of build height, refinement using adaptive subdivision, generation of the bounding volumes, root finding, evaluation and identification of output points. The generalized slice algorithm is as shown in Figure 3.7.

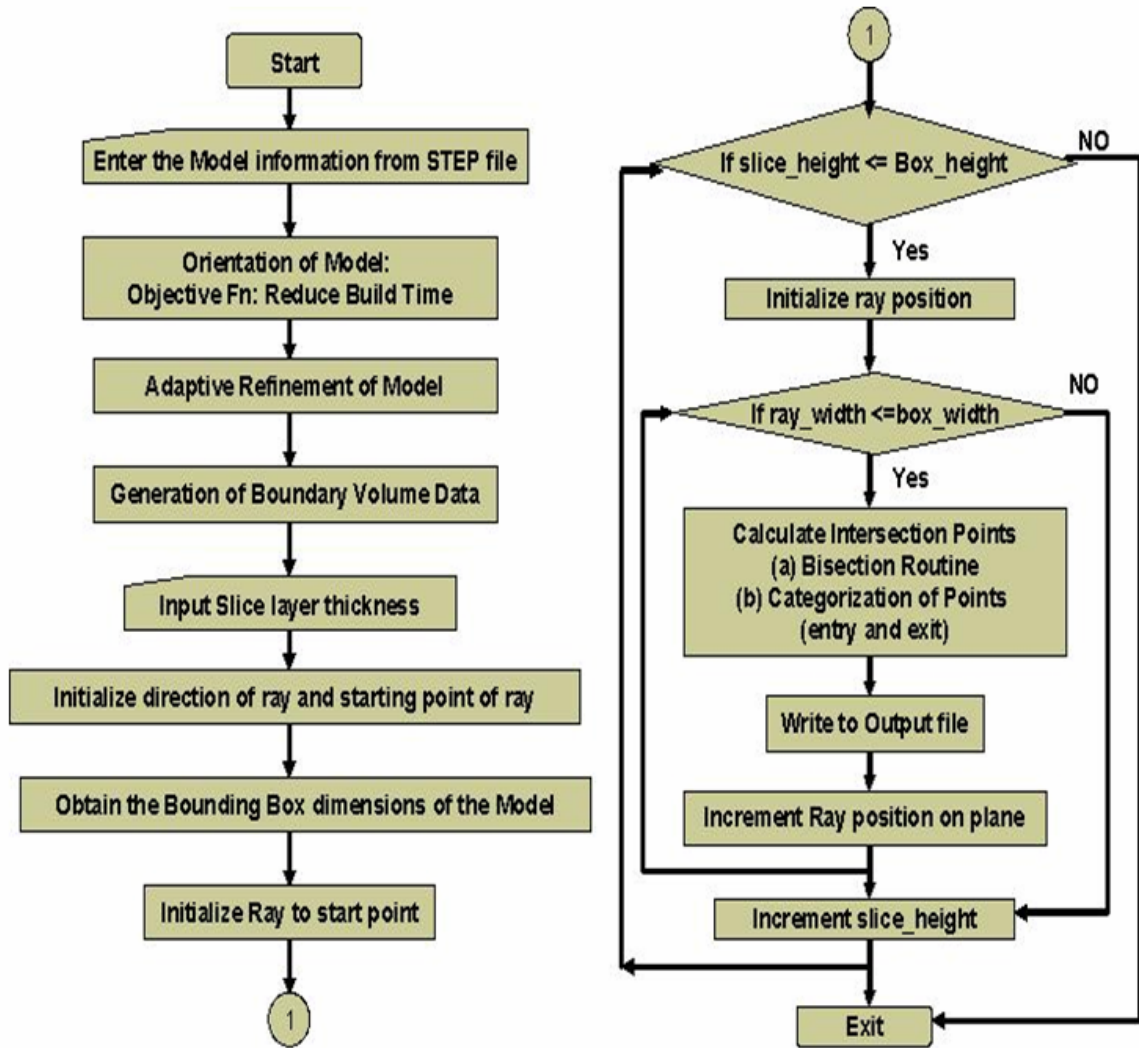


Figure 3.7: General Slice Algorithm

Step 1: Orientation of CAD Model to Minimize Build Height

The model orientation within the fabrication bed affects the build time, part strength and surface finish. Thus before the part is sliced, a minimization of certain objective criteria specified by the designer will be performed to find the optimal orientation for slicing the model. A number of orientation schemes have been devised. Some base their orientation with the largest convex hull of the object as the base [Puduhai et al, 1995], while some others orient the part based on certain critical features

of the model [Frank et al, 1995]. We have used a scheme in which the model is incrementally oriented about user specified axes to obtain the least possible build height dimension. Given a set of n NURBS surfaces $S_{i...n}(u, v)$ that is enclosed in a Bounding Box of height H (a function of orientation angle “ θ ”), the objective function can be mathematically expressed as:

$$\text{Min } Z = H(\theta) \quad \text{subject to } 0 < \theta < 360 \quad (3.9)$$

where, Z is the build height of the model and θ is the orientation of the model with respect to the object coordinate axes. The optimally oriented NURBS faces with the least height in the z -direction (build height) then act as the input to the second step.

Step 2: Refinement of NURBS Surfaces

Refinement or Subdivision of the NURBS surface is the addition of control points to a surface without changing its original shape. The process is implemented using the Oslo Algorithm [Bartels et al., 1987]. The basic idea is to take in the original set of knot vectors that make up the surface and add new knot values into them, creating additional control points corresponding to the new knot vectors. If the addition of the new knot values at the same parametric value is equal to the order of the curve, then the two new surfaces created will have the same shape as the original unrefined surface. They would each have a set of control points at the region where they join. The procedure is illustrated in Figure 3.8. This is done for the following two reasons. Numerical methods work better and faster when the parametric domain is smaller and no multiple value roots

exists within the patch. Secondly, by refining the mesh, the various sub-patches which are essentially NURBS by themselves can be enclosed using bounding volumes thereby enabling the slice algorithm to determine which sub-patch contains the actual root. This stems from the fact that it is easier to determine the collision of rays with primitive bounding volumes than NURBS surfaces. Hence by identifying the sub-patch in which the solution exists, the domain in which the numeric solver has to work is limited and hence results in better chances of finding the roots.

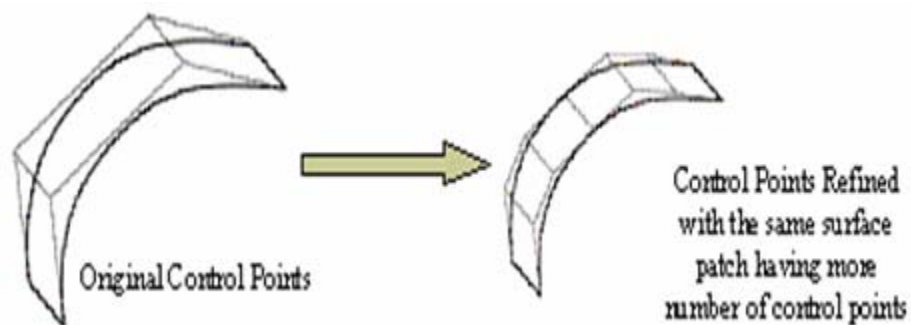


Figure 3.8: Refined Process of NURBS using the Oslo Algorithm

The adaptive subdivision of the NURBS surface continues as long as a subdivision or flatness criteria is met. Regions that have a higher degree of curvature are subdivided more than regions that have a lesser degree in curvature and hence the term adaptive subdivision. Each new sub-patch contains all information that defines the NURBS and an appropriate ID is given to it. The refinement procedure is extensively used in the tessellation of parametric surfaces and has been studied extensively by a number of researchers. However, our main criteria in refinement of the mesh as opposed to the tessellation procedure is not to ensure accuracy in representation but more in

guaranteeing that convergence will occur within the refined sub-patch. In this regard, selection of the subdivision factor is an important step and an appropriate value controls to a great extent the success of accurate slicing.

Step 3: Boundary Volume Data Structure Generation

As the refinement procedure of NURBS progresses, the boundary volume data structure gets filled up; sub-patches are stored in the data structure along with a unique id. The main idea behind the storage of these sub-patches is the generation of the boundary volume. Boundary volumes are usually primitives that enclose the sub-patch completely. Some of the candidate primitives that can be used are oriented boxes, spheres, and parallelepipeds [Yang et al., 1987, Barth et al., 1993, Fournier et al., 1994]. The selection of a primitive depends on the tightness of fit and speed of intersection calculation with the ray. We have used in our approach axis aligned boxes that are oriented with the main coordinate axis of the model. Once they are axis aligned, the process of creating the bounding volumes is easier with a ray-box intersection using up less computational power and hence faster processing times.

The bounding box is created using the control net points created from the refinement stage of the process. An important aspect to note is that the control mesh of a NURBS patch will always enclose the surface and therefore any convex shape surrounding the control net would also enclose the surface. The generation of boxes around the subpatch surface is illustrated in Figure 3.6. Failure to enclose the sub-patch surface completely results in ray hits being missed out and having gaps in the sliced model.

Step 4: Numerical Solution - Bisection Iteration Routine

There are a variety of numerical methods that are available to solve for the intersection points. Among these are bisection algorithms, linear interpolation, Newton Iteration and fixed point iteration [William, 1993] or a combination of two algorithms. Although the latter two methods are fast, in some cases they do result in solution divergence rather than convergence. This depends on the actual initial guess to the polynomial equation. Our problem reduces to finding the value (u^*, v^*) that corresponds to the intersection point of the ray and the NURBS surface. Almost all root finding techniques employ a tolerance value within which the error bound is defined. Selection of one process over the other entirely depends on processing time available and the particular equation that is intended to be solved. Though ray tracing methods in graphic applications employ Newton's iteration or its variants since it proves to be a faster process, we have used the Bisection iteration routine mainly due to its simplicity and robustness.

The surface sub-patch contained within the boxes that are hit by the ray are retrieved from the boundary volume data structure and passed onto the solver method routine. The routine works by iterating towards the solution of one variable. However, we need to solve for 2 variables (u, v) that satisfy the equation. This is achieved by keeping one variable constant and iterating towards the best value of the second variable that satisfies the equation. If the error in the points generated does not satisfy a tolerance, ϵ , the first variable is incremented by a pre-defined amount and the procedure repeated. The process continues until a solution is found, the limit of the first variable is achieved or a specified number of iterations have been completed.

We use three criteria to decide when to terminate the bisection iteration routine. The first condition is our success criteria, if the current values are closer to the desired point by some determined tolerance, ε , given by:

$$F(u_n, v_n) < \varepsilon \quad (3.10)$$

the algorithm reports a successful hit. The value of ε determines two aspects, first, the accuracy of our results and second, success in reporting a hit. A tight value might result in the routine reporting a miss due to satisfying the maximum iteration condition and on the other hand a higher tolerance will result in intersection point offset errors. The second condition is also a success criteria in which if the absolute value of successive iterations values are small enough such that it is equal to a preset tolerance, the iteration exits giving out the roots. This is expressed as follows

$$|F(u_n, v_n)| < \varepsilon^* |F(u_{n-1}, v_{n-1})| \quad (3.11)$$

The third condition is the failure criterion, and if satisfied, the routine exits reporting a miss. If during the routine, the error calculated is approximately same as the error in the previous iteration, the iteration exits reporting a miss provided the success criteria has not been met. This is mathematically written as

$$F(u_{n-1}, v_{n-1}) \cong F(u_n, v_n) \text{ subject to } F_n(u, v) > \varepsilon \quad (3.12)$$

where n denotes the n^{th} step of iteration

Step 5: Categorization of Intersection Points (Entry or Exit)

Once the intersection points are found out for every ray that is cast onto the slice planes, these points need to be classified according to its hit type. We have done this by calculating the normal of the surface at the point under consideration. This normal vector (\hat{N}) can be calculated by taking the cross product of the tangent vectors in the u and v direction evaluated at the given point. If it is assumed that the ray shoots across in the y direction, a dot product between the ray and the normal vector \hat{N} , would help in the classification of the points as to be an entry point, an exit point or an edge point. The points once classified are stored in a pre-defined format to be visually represented using a graphical interface and also use this data for conversion to machine instructions.

2.2.4 Algorithm and Implementation

The slice algorithm code was developed in C programming language under the Microsoft Visual Studio compiler environment. The different modules of the algorithm were written in separate files and all of them linked together by the main file. Figure 3.9 gives the detail functional subroutines available in each file. The functionalities of each file will be explained in a later section and will be called the slicing module. Appendix A contains the flowchart design of each major routine within the files for better understanding of the process.

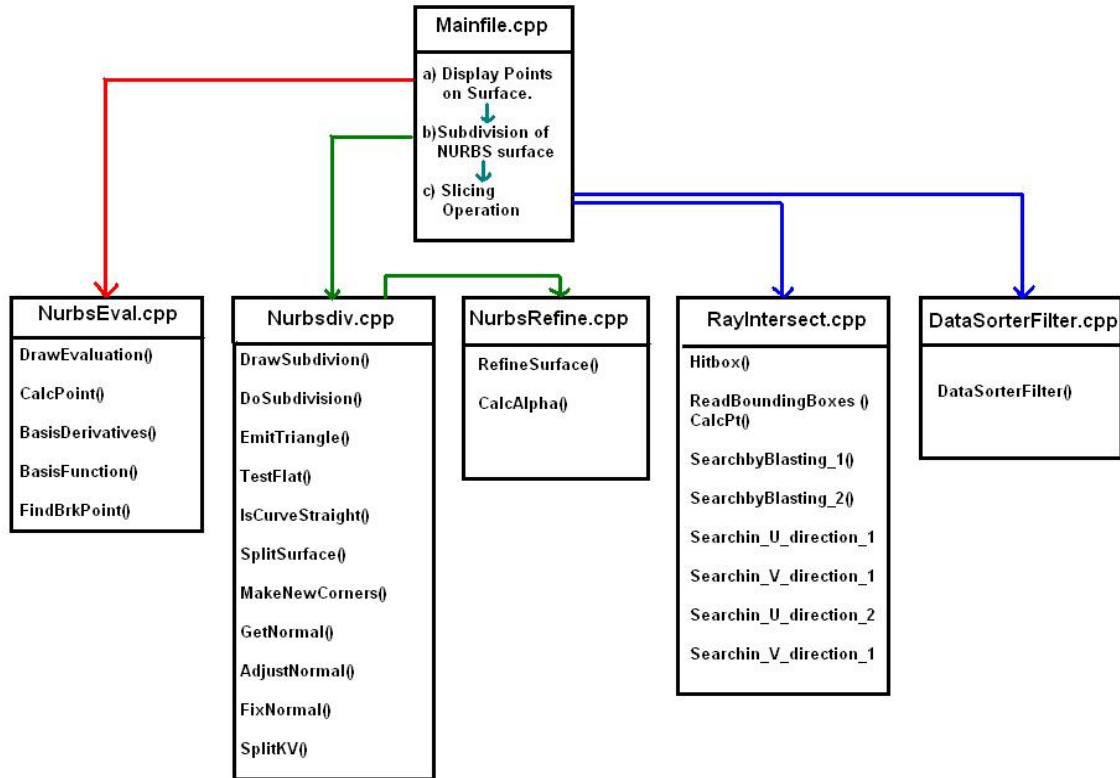


Figure 3.9: Program file organization within algorithm

Mainfile.cpp: This file contains the main () function of the slicing module. It is designed with an interactive menu system with 3 important options. The first option available is the ability to cover the NURBS model with a point cover. This option can be selected to evaluate the accuracy in initial data input to prevent unforeseen errors during the slicing operation. The procedure calls up the function DrawEvaluation() from the file.

NurbsEval.cpp. The second option in the menu is the ability to subdivide the NURBS surface to smaller sub-patches. This is done by calling the function DrawSubdivision() available from the file Nurbsdiv.cpp. This is the initial preprocessing step required before the actual slicing operation. The third option available is the actual slicing operation to

calculate the intersection points. Function calls are made to the different bisection routine methods defined in **Rayintersect.cpp** file. Besides that, a function call to `datasorterfilter()` defined in **Datasorterfilter.cpp** file is made to organize and output the calculated intersection points in the required format.

NurbsEval.cpp: The procedures defined in this file produces a uniform cover of points evenly spaced out on the surface of the NURBS CAD model. The number of surface points generated can however be controlled by assigning different values to the variable “**Granularity**”. The default value has been set to 100. It evaluates the surface points at specific values of knot parameters u and v by iterating through the parameter values, the surface points are generated.

Nurbsdiv.cpp: This file contains the procedures that perform the task of subdividing the original NURBS data to smaller sub patches. An adaptive subdivision procedure of the surface takes place and continues until it meets the subdivision criteria factor given by the variable “**SubdivTolerance**”. The value ranges from 0.1 to 0.01, depending on the size of the model and complexity in its outer contour surface. Lower the tolerance value, more number of subdivisions with subsequently higher number of sub patches. Careful selection of this value is needed and the user gains experience in the appropriate value to be chosen. The procedure **EmitPatches()** saves the output sub-patches in a defined format onto a text file.

RayIntersect.cpp: The file contains all the function responsible for the slicing operation. The major functions include reading bounding boxes that contain the sub patches, determination of the bounding box that has been hit by the ray and bisection iteration routine procedures. The output from these functions are the intersection points and they are sent to the main file using the variable pointer “**hitpoint**”. The bisection routines are 4 in all each with a different characteristic in searching for the intersection points. Not all routines are called and each new bisection routine is called only if the function above them fails to find the intersection point. If the 4 bisection routines functions fail to find any point, then 2 other functions named the Search_by_Blasting function is activated. This is a time consuming procedure where the small sub patch of the NURBS surface is flooded with large number of points. The function then finds the point that satisfies the intersection point criteria. The difference between the two Search_by_Blasting functions is that one of them has its condition of success criteria relaxed while the other a bit more restrictive. If none of the 6 functions are able to find an intersection point, a NULL value is returned to the main program signifying a NO HIT status for the ray.

DataSorterFilter.cpp: All intersection points that are returned by the Rayintersection.cpp file to the main program for one slice level is stored within an output data structure. This data structure is sent to the function datasorterfilter() contained within this file. The collection of points is then filtered by a set of conditions to classify it to be an Entry or Exit Point. The conditions are based on a number of factors that include direction of normal, magnitude of normal, condition of Hit etc. Once the data is filtered,

the points are written out to a format readable by the Fabrication Planning software with appropriate points marked as Entry or Exit.

The slicing module integrates itself within a complete framework in which CAD data is first acquired through the CAD vendor Solidworks. A Macro has been written to acquire the NURBS data of the CAD model from the solid modeling kernel and is output in a predefined text format. This input file is read by the slicing module and the appropriate print path instructions are generated. These instructions in the form of a machine dependant output are read by the Fabrication Planning Software to display the raster pattern of the slice layers that make up the model. Figure 3.10 gives the overall implementation from the CAD model to the raster display of the different slices.

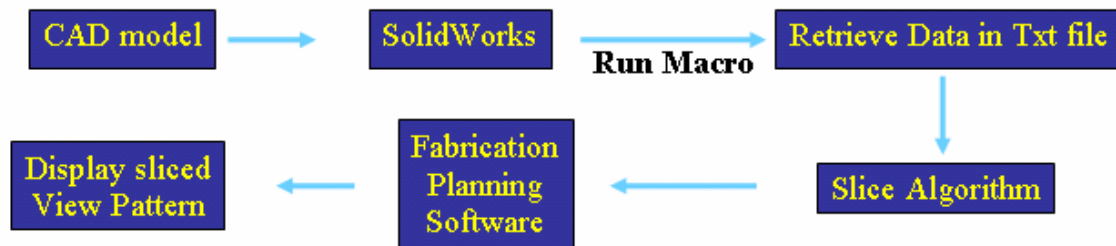


Figure 3.10: Data Flow of the CAD model data

3.4 Model Case Studies

The developed algorithm was tested for 10 different kinds of models each with certain characteristics of its own to test the capability of the algorithm. Given below are the test case results and its various process parameters. Model #1 has been explained in detail on how to run the algorithm right from the initial CAD input to final raster display.

3.3.1 Step by Step Procedure in Execution of Algorithm - Model #1 – Sphere

We have tested the algorithm's capability to slice the sphere with accuracy and quality. Figure 3.11 gives an example of a sphere model that is composed of 14 NURBS surfaces. Given below is the step by step procedure in testing the algorithm.

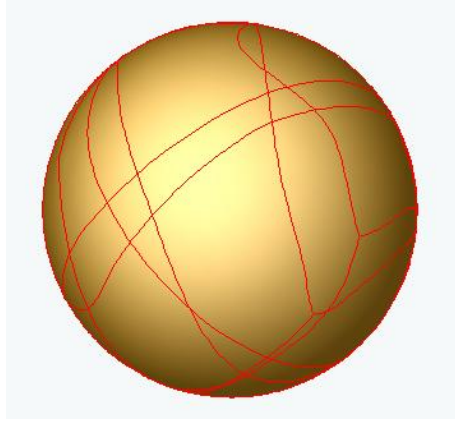


Figure 3.11: 14 NURBS patch sphere

Step 1: Open the .STP CAD model file in SolidWorks. Open up **Tools->Macro->Run->Splsurf.swp**. The macro should take only a few seconds to run. Browse to the directory that contains the Macro and a file named “**FACES.txt**” should be visible. The file format is shown in Figure 3.12. The first Number indicates the total number of NURBS definitions within the file. The second number below gives the Surface ID# of the NURBS definition that follows beneath. The third number gives the number of trimming curves associated with the model. The fourth line contains 2 numbers both indicating the number of control points in the U and V direction. For ex. the number 6 and 6 suggest a 6x6 matrix of 36 control points defining the surface. The fifth line contains the order of the NURBS surface in the u and v direction. The sixth line describes the knot vector

values in U and the seventh line describes the knot vector values in the V direction. The rest set of lines give the coordinate values of the control points along with their weights.

This file then forms the input to the Slicing module.

```

14 -----> Total Number of NURBS surfaces
1 -----> Surface ID#
0 -----> No. of Trimming Curves
6 6 -----> No. of Control Points in the U and V directions respectively
4 4 -----> Order of the NURBS surface in U and V direction.
0 0 0 0 0.333333333333 0.666666666667 1 1 1 1 -----> Knot Vectors in U direction
0 0 0 0 0.333333333333 0.666666666667 1 1 1 1 -----> Knot Vectors in V direction
638.362042532721 X - coordinate values of the control points. 376.973254238598 Y. coordinate values of the control points. 35.5724284984094 Z. coordinate values of the control points. 1.0
628.170921454705 385.553716791075 28.8454439530912 1.0
523.798014799386 408.962476151517 1.314704979297 1.0
365.895790604415 388.442166606188 23.3123865340618 1.0
278.551826510066 362.951225528533 72.7417118290362 1.0
240.408896376572 343.246294508705 105.446459119944 1.0
628.170921454705 385.553716791075 28.8454439530912 1.0
638.011139257669 423.20228327624 22.3974635319836 1.0
534.556578151812 452.286518152358 6.2108039286086 1.0
367.208573845722 434.553179937114 11.9086643604494 1.0
274.496364207571 407.290023095617 59.9981035221204 1.0
233.634789973631 387.360058209881 91.809862124638 1.0
714.335627190582 378.240362218652 59.6175046472262 1.0
713.878223982784 437.179024675965 44.3539085379288 1.0
610.431021054668 484.012343052245 2.5474014508054 1.0
424.538092030627 495.815856825333 10.4192239212768 1.0
310.659237075991 485.633513353535 28.1957809544772 1.0
557.105479096634 470.067091504164 57.7120911710410 1.0

```

Figure 3.12: Data Output Format from the Solidworks Macro

Step 2: Open up the code in Microsoft Visual C++ environment. Compile and Run the code. A menu with different menu choices shows up. The menu has different options and each can be selecting by simply selecting the number of each menu choice. Type in “2” to select **Tessellate Surface** menu option. The menu then prompts you to enter the Filename that contain the data input; type in “**faces.txt**”. Once this is done, the code then begins subdividing all of the NURBS surfaces defined in the input file. Figure 3.13 shows a captured image as the algorithm works in subdividing the NURBS surfaces. The subdivided NURBS sub-patches are stored in the file “**SubdividedNURBS.txt**”

```

E:\Therics\slicealgo\B spline\TheriformSlicev1.0\Debug\graphicsgems.exe
***** W E L C O M E   T O   S L I C E 2002 *****
 1. Evaluate Points
 2. Tessellate Surface
 3. Calculate Intersection Points
 4. Delete all files
 5. Rotate Faces
 6. Exit
Enter your choice :2
Enter the filename :faces.txt
Subdivision in process .....1
Subdivision in process .....2
Subdivision in process .....3
Subdivision in process .....4
Subdivision in process .....5
Subdivision in process .....6

```

Figure 3.13: Subdivision Procedure

Step 3: After the subdivision process, the menu shows up once again and type in “3” to select the “Calculate Intersection Points” menu option. The procedure opens up the sub-patch file and stores them in data structures. It calculates the Bounding Box dimensions of the model and displays it as shown in Figure 3.14. It also displays the total number of NURBS sub-patches, ray increment and slice increment values. The results at the end of this step are stored in the file “machineformat.txt”. The format of the file is shown in Figure 3.15. This format is necessary for it to be read by the Fabrication Planning Software.

```

E:\Therics\slicealgo\B spline\TheriformSlicev1.0\Debug\graphicsgems.exe
***** W E L C O M E   T O   S L I C E 2002 *****
 1. Evaluate Points
 2. Tessellate Surface
 3. Calculate Intersection Points
 4. Delete all files
 5. Rotate Faces
 6. Exit
Enter your choice :3
No of box :7722
Bounding Box Dimensions of Model :998.958 999.766 998.524
Bounding Box Dimensions of Model :0.3459 3.13194 0.524883
RAY INCREMENT :13.3148 SLICE INCREMENT :16.6333
Calculating at height 0.524883 .....
Calculating at height 17.1582 .....
Calculating at height 33.7915 .....
Calculating at height 50.4248 .....
Calculating at height 67.0582 .....
Calculating at height 83.6915 .....
Calculating at height 100.325 .....

```

Figure 3.14: Slicing Operation

```

machineformat - Notepad
File Edit Format View Help
Assembly Name = sphere.stp
Date Saved = 11/13/2002 4:32:51 PM
Operator =binil
Time and Date of Scan =wed Nov 13 16:33:29 2002
Maximum Assembly Dimensions =10, 20 ,0 by 40.0, 53.22, 25
Bodies in Assy =02044-1
Scan Parameters = 0 StartX, 0 StartZ, 50 EndX, 50 EndZ,13.3148 XIncrement, 16.6333
ZIncrement
Stagger Parameters =
386.476, 444.219, 17.1582, 0, 0, 0, 1, FACE ENTER
386.476, 552.97, 17.1582, 0, 0, 0, 1, FACE EXIT
532.939, 378.74, 17.1582, 0, 0, 0, 1, FACE ENTER
532.939, 621.537, 17.1582, 0, 0, 0, 1, FACE EXIT
546.254, 383.299, 17.1582, 0, 0, 0, 1, FACE ENTER
546.254, 617.484, 17.1582, 0, 0, 0, 1, FACE EXIT
626.143, 476.306, 17.1582, 0, 0, 0, 1, FACE ENTER
626.143, 526.792, 17.1582, 0, 0, 0, 1, FACE EXIT
599.513, 352.292, 33.7915, 0, 0, 0, 1, FACE ENTER
599.513, 648.315, 33.7915, 0, 0, 0, 1, FACE EXIT
626.143, 369.569, 33.7915, 0, 0, 0, 1, FACE ENTER

```

Figure 3.15: Format of Ray Cast File for FPS

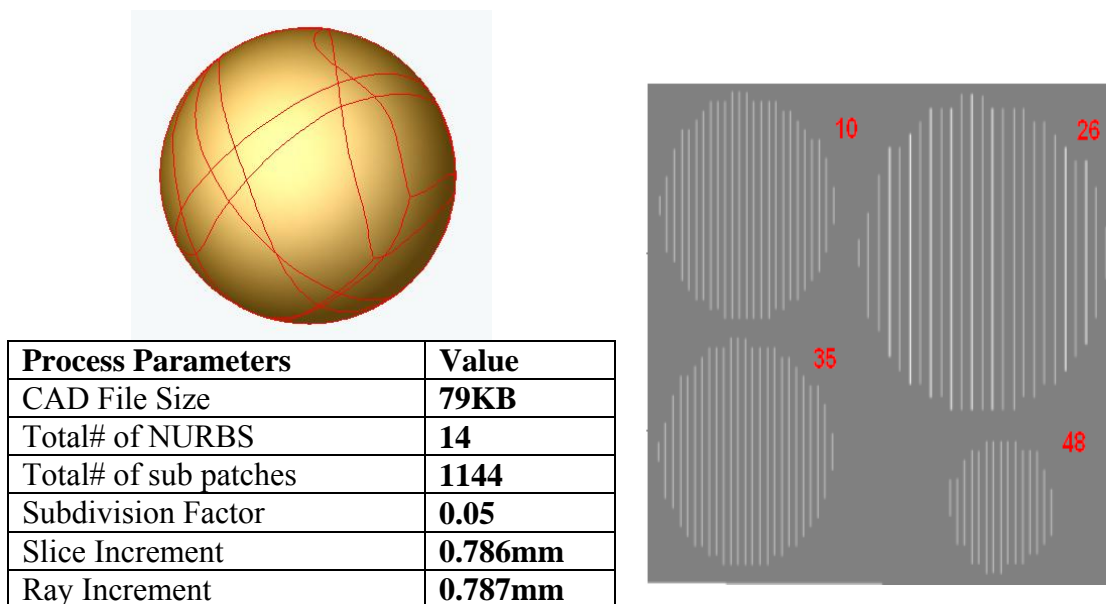
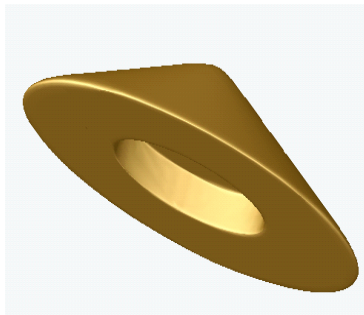


Figure 3.16: Raster Pattern for the sphere

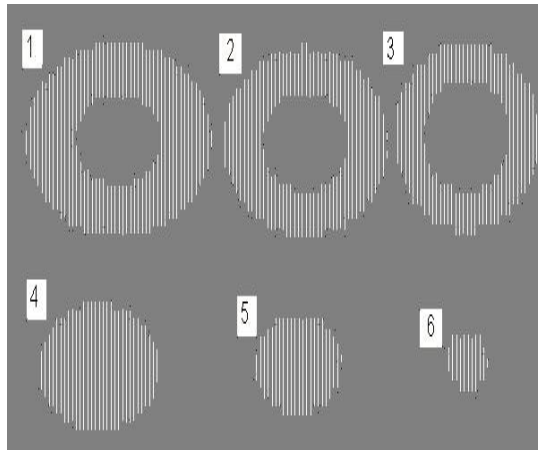
Model 2 - Cone: This model consists of about 44 NURBS surface definitions which were extracted from the STEP input CAD file using a STEP reader. A subdivision factor of 0.01 and a tolerance value of 0.01 were used for adaptive refinement and root finding respectively. The model tests the capability of the algorithm to detect interior cavities as

depicted by the hole in the cone at the bottom surface. Figure 3.17(b) shows each of the raster patterns at different slice levels.



Process Parameters	Value
CAD File Size	861KB
Total# of NURBS	44
Total# of sub patches	3745
Subdivision Factor	0.01
Slice Increment	0.31mm
Ray Increment	1.08mm

(a)



(b)

Figure 3.17: Raster Pattern for the cone

Model 3 – Foot

This model consists of about 19 NURBS surface definitions which were extracted from the STEP input CAD file using a STEP reader. A subdivision factor of 0.1 and a tolerance value of 0.01 were used for adaptive refinement and root finding respectively Figure 3.18. The model tests the capability of the algorithm to detect relatively flat surfaces within the NURBS definition as depicted by the flat bottoms and cut out regions in the foot model

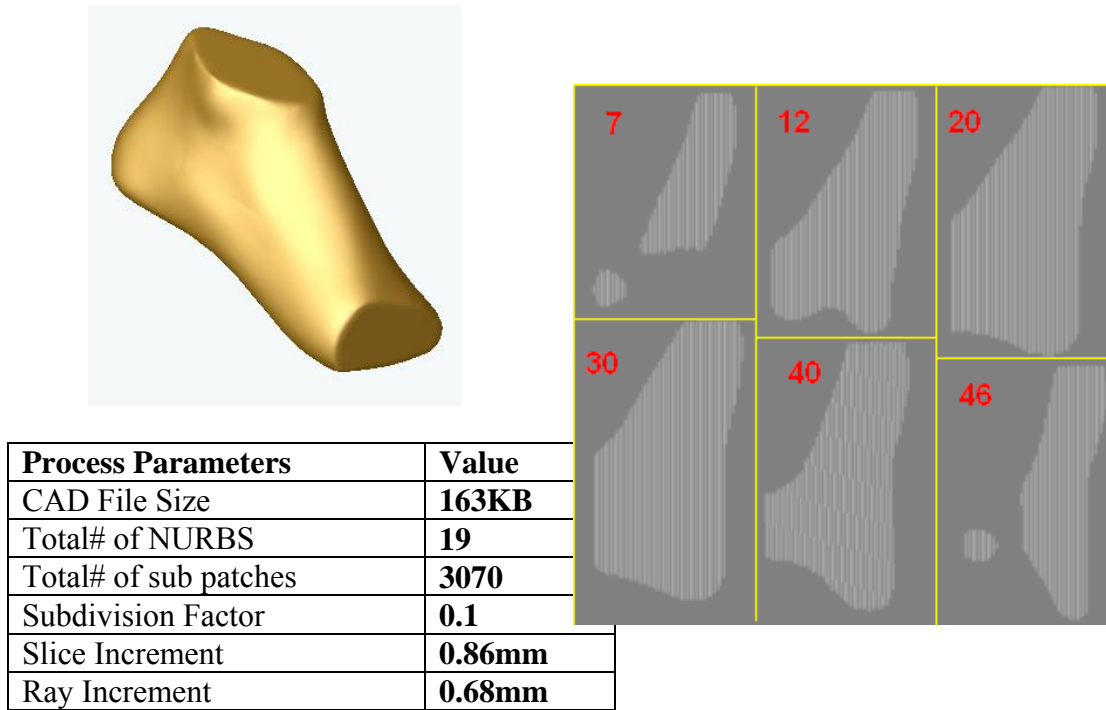
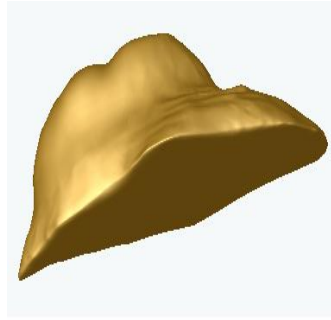
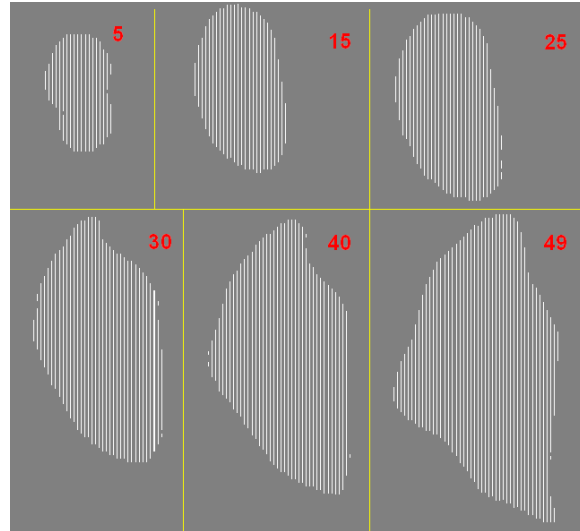


Figure 3.18: Raster Pattern for the foot

Model 4 - Sinus Graft Model 1: The second model contained 102 NURBS surface definitions, extracted through the same method using the reader and the data transferred to the algorithm. This model has the characteristic of having more complex curved NURBS contours along with multiple entry and exit points. In this case a subdivision factor of 0.1 was sufficient for appropriate slicing with no perceivable slice errors during part layout. The same tolerance value of 0.01 was used for the root finding routine. Figure 3.19(a) shows the model optimally oriented and figure 3.19(b) illustrating the sliced model part layout at different slice levels.



Process Parameters	Value
CAD File Size	2.70MB
Total# of NURBS	78
Total# of sub patches	4990
Subdivision Factor	0.1
Slice Increment	0.35mm
Ray Increment	0.22mm

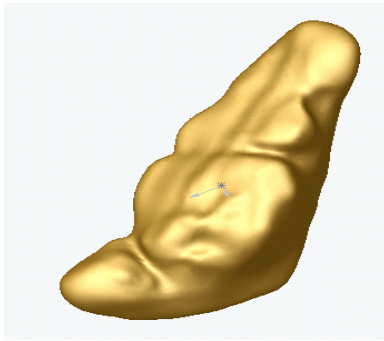


(a): Model and Process Parameters (b): Raster Pattern of Sinus Graft in FPS.

Figure 3.19: Raster Pattern for the sinus graft model 1

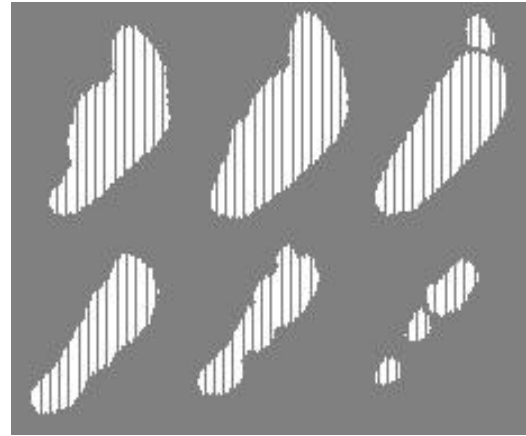
Model 5 – Sinus Graft Model 2:

The second model contained 102 NURBS surface definitions, extracted through the same method using the reader and the data transferred to the algorithm. This model has the characteristic of having more complex curved NURBS contours along with multiple entry and exit points. In this case a subdivision factor of 0.1 was sufficient for appropriate slicing with no perceivable slice errors during part layout. The same tolerance value (ϵ) of 0.01 was used for the root finding routine. Figure 3.20(a) shows the model optimally oriented and Figure 3.20(b) illustrates the sliced model part layout at different slice levels.



Process Parameters	Value
CAD File Size	1.08MB
Total# of NURBS	102
Total# of sub patches	5302
Subdivision Factor	0.1
Slice Increment	0.548mm
Ray Increment	0.29mm

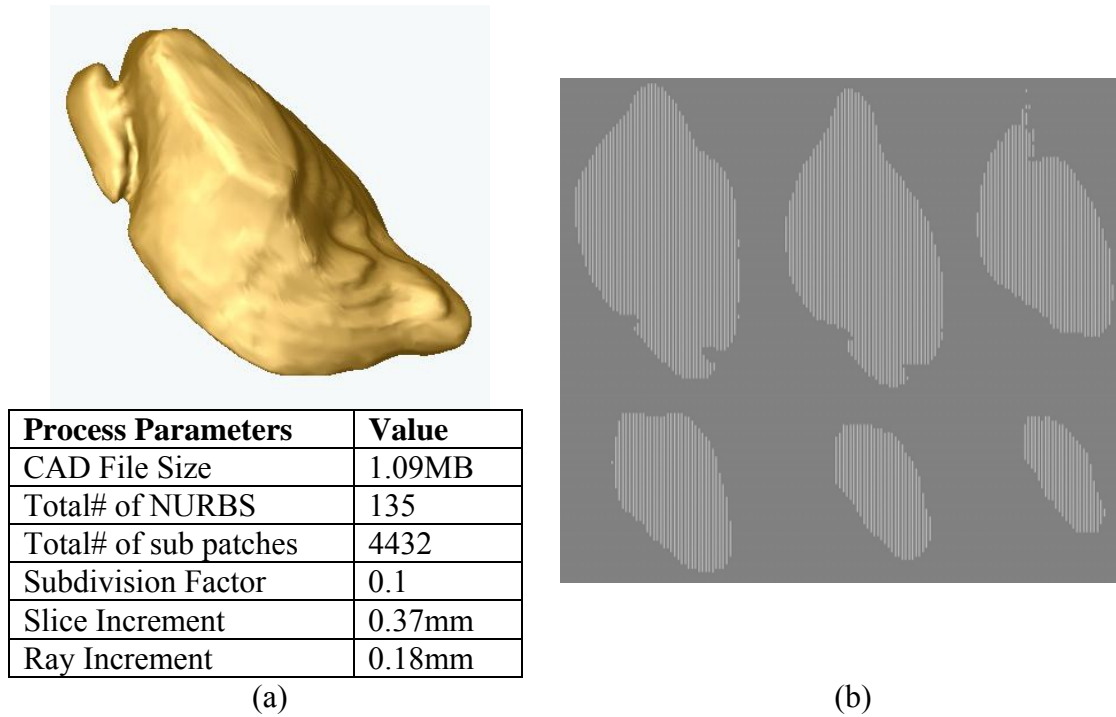
(a)



(b)

Figure 3.20: Raster Pattern for the sinus graft model 2

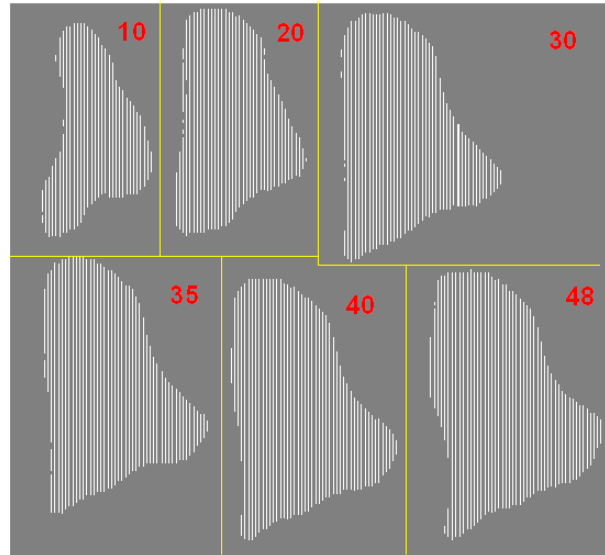
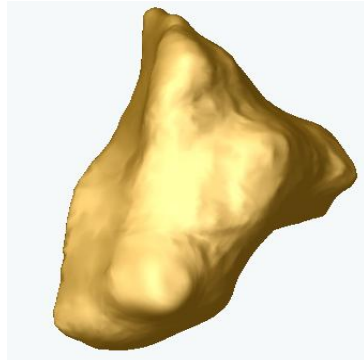
Model 6 - Sinus Graft Model 3: The third model is more complex not only in terms of having more number of NURBS surface but also in terms of its overall shape. This model depicts the capability of the algorithm to handle multiple entry and exit points that are close to each other as well as accurate slicing procedures at tangent edges of the model. A subdivision factor of 0.1 and a tolerance value of 0.01 were used for the process. Figures 3.21(a) illustrates the model and fig 3.21(b), the corresponding slice layout on the fabrication bed for different layers. It can be seen that the algorithm did work well with key features detected at the slice plane shown.



(a) (b)
Figure 3.21: Raster Pattern for sinus graft model 3

Model 7 – Sinus Graft Model 4:

The fourth test model data is neither complex nor is it a large file. The model contains 78 NURB surfaces and was used to highlight how the proposed method has overcome errors caused due to STL conversion. This particular model had failed to slice using commercially available slice software. The parameters and tolerance values were 0.1 and 0.01 respectively. Figure 3.22(a) illustrates the model and Figure 3.22(b), the corresponding slice layout on the fabrication bed for different layers.



Process Parameters	Value
CAD File Size	5.5MB
Total# of NURBS	263
Total# of sub patches	5216
Subdivision Factor	0.1
Slice Increment	0.47mm
Ray Increment	0.26mm

Figure 3.22: Raster Pattern for the sinus graft model 4

Model 8 – Bone with Holes:

This model is not complex in its outer shape but was selected to see if holes drilled within the model were captured during slicing operation. The model had a fairly high number of NURBS surfaces at 200 with about 13198 sub patches generated by using a sub division factor of 0.05. The model was fairly long at the z-level hence the slicing algorithm was tested for any memory deficiency issues during the process. The raster patterns of the model are shown on the right and it can be seen that it has fairly captures most interior and exterior detail of the model.

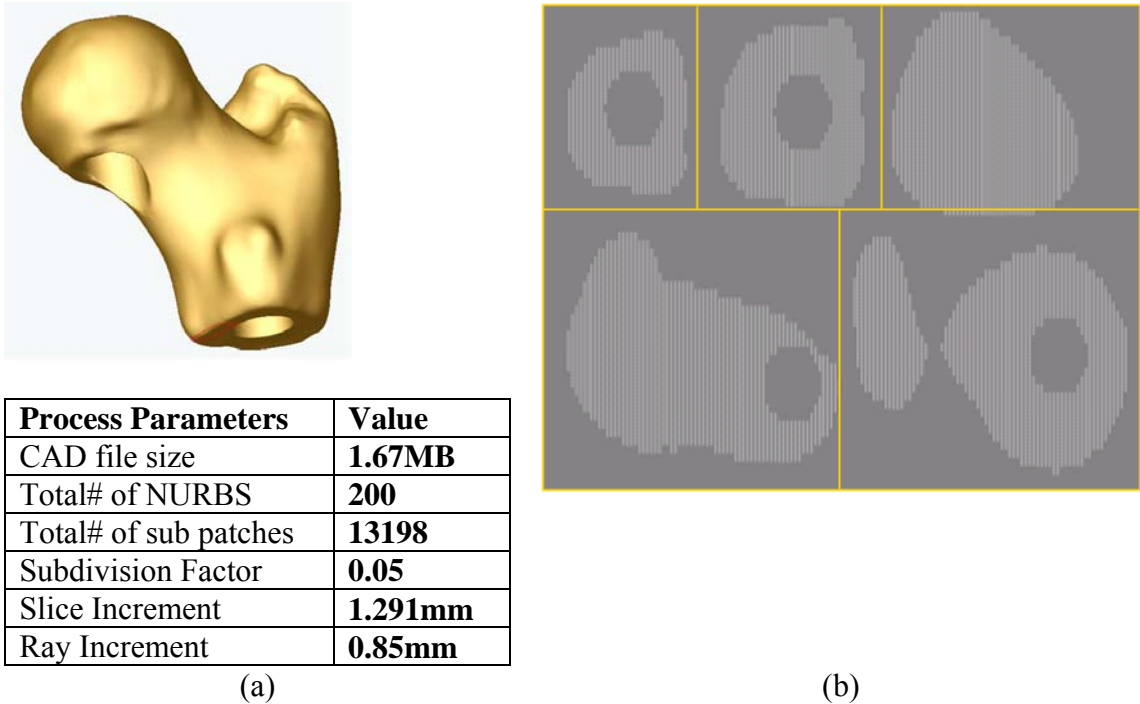


Figure 3.23: Raster Pattern for the bone with holes

Model 9 – Combination Bones:

This particular model was made by combining two complex bone shape architecture and fusing them together to obtain the overall CAD model. It has fairly complex contours on its outer shape along with internal hole features. The model is comparatively huge with about 252 NURBS surfaces, subdivided with a fairly low subdivision factor at 0.05. This value was needed to obtain good results in the raster patterns. The figure bellows show various process parameters of the slicing process and the raster patterns of the model at different slice levels. Slice layer 10 shows how a particular inner feature of a hole was captured quite clearly showing the quality of slice levels that can be achieved.

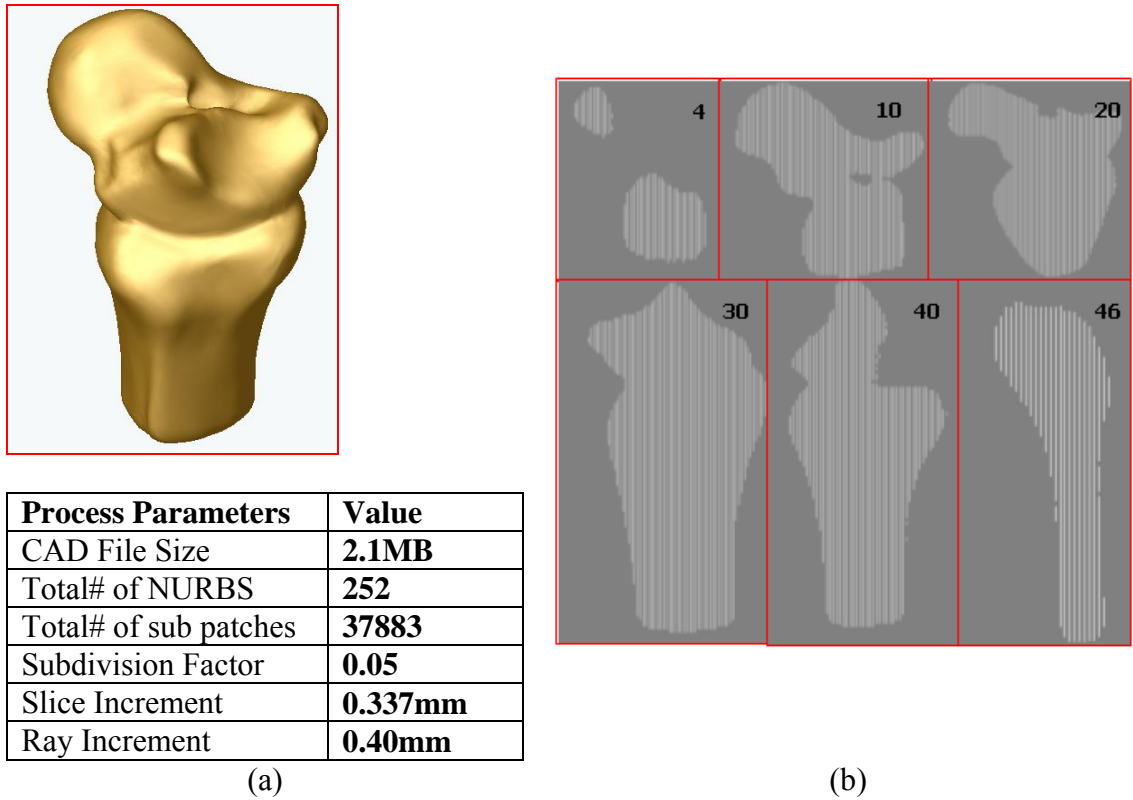


Figure 3.24: Raster Pattern for the combination bones

3.5 Conclusions

The advantages and disadvantages offered by the STL and STEP based methods can be seen as displayed in Table 2.4. A comparison has been drawn by the two methods of slicing in terms of file storage and processing time. All results are obtained from a Pentium4 2Ghz, 1GB RAM system. While direct slicing takes more time to process, it has comparatively less storage space and requires no use for file check routines. Though the STL format is the quickest method to slice models, they involve higher storage costs and may require file checks and repair routines depending on the complexity of the surface.

Table 3.1: STL and STEP based slicing comparisons

Name	Format	Features	File Size	Time*
Foot	STEP	19 NURB	164KB	48 sec
	STL	200,000 tri	45.9MB	6 sec
Sinus Graft Model - 1	STEP	78NURB	924KB	72 sec
	STL	33878 tri	8.55MB	Failed
Sinus Graft Model - 3	STEP	135NURB	1.09MB	76 sec
	STL	333120 tri	23.2 MB	2 sec
Sinus Graft Model - 4	STEP	263 NURB	485KB	73 sec
	STL	120,000 tri	32MB	5 sec
Cone	STEP	102 NURB	860KB	71 sec
	STL	52,868 tri	12.25MB	2 sec
Sphere	STEP	14 NURB	78.5KB	53 sec
	STL	77,999 tri	18.6MB	3 sec

Direct Slicing of CAD model promises to offset the disadvantages posed by the STL format particularly with freeform shapes. The limitation of the current STL format of the CAD model can be summarized as follows:

- Tessellation involves approximation of surfaces with triangular facets which is undesirable in general, particularly when we are dealing with models that contain freeform shapes.
- As model precision demands become more stringent, the number of facets required to adequately approximate these freeform shapes will increase. This would account for huge STL file sizes increasing the chances of errors.

- Many CAD systems fail to generate valid model tessellations and often involve manual fixing of errors raising the need to improve tessellation procedures. However, this calls for implementing robust and efficient procedures which may be difficult and would be computationally expensive to implement.

The direct slicing method does not involve file repair routines and file sizes are much smaller to handle. It also throws up the possibility of slicing multi material volumes or heterogeneous models, a definite advantage over STL files. Since the exact representation is used, complete design information is carried over to the fabrication stage with no loss in information. Although direct slicing does take longer time to slice, this problem can be offset by efficient algorithms in terms of reducing memory usage and faster computing power. A point to note is also a careful selection of the subdivision factor and the tolerance value. We have found that under continued trials, an intuition is developed on the selection of the right parameters which works best for the models. Future research would involve the development of a direct slicing method on heterogeneous multi-material models with an appropriate slice layer format. The procedure would also be extended to leverage the benefits offered by direct slicing in designing biomimetic scaffolds for tissue engineering applications.

CHAPTER 4 : FREEFORM FABRICATION OF TISSUE SCAFFOLDS

4.1 Internal Architecture Design of Tissue Scaffolds

Although we can use CAD models to represent individually designed unit cells, CAD is not generally capable of representing a unit cell assembly, for example, using different unit cells to fill in the femur structure as shown in Figure 4.1(c). Since each unit cell is designed with a complex set of features, the combination of hundreds of unit cells will result in the formation of an intricate scaffold internal architecture which is beyond the capability of many current commercial available CAD systems [Chua et al., 2002, Nam et al., 2004]. In addition, the STL format which serves as the current industry standard for the data exchange between CAD and freeform fabrication machines cannot be used to efficiently transfer data for such complex intricate structures as described in Chapter 2.

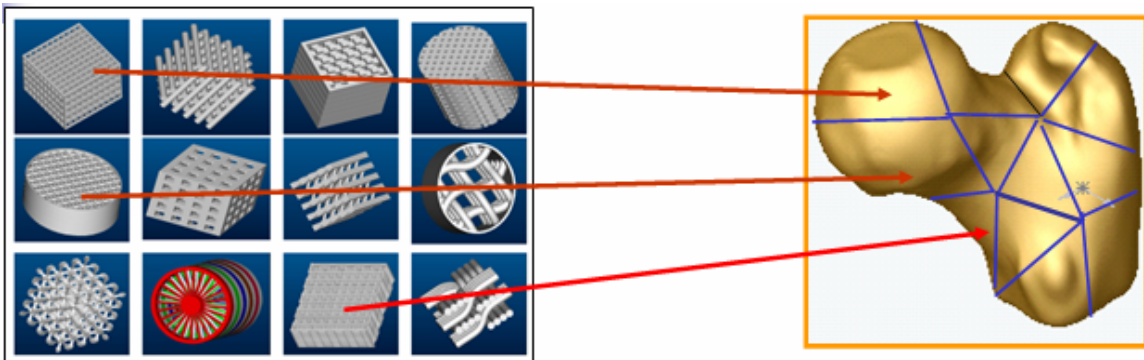


Figure 4.1 : Unit cell assignment within scaffold structure

Therefore, there is a strong demand to develop new methods to transfer the information of biomimetic designed scaffolds to a process tool path data for final fabrication. We propose to develop a novel solution, an Internal Architecture Design (IAD) approach, to generate process planning instructions for freeform fabrication of

biomimetic designed tissue scaffolds. The novelty of the IAD approach is that it allows the generation of the scaffold process planning instruction set without the creation of a unit cell filled 3D CAD scaffold model, thus avoiding the difficulty of using CAD to represent the assembly of the unit cell models. The IAD approach stems from the principle of the decomposition and material accumulation of layered manufacturing principle [Lin et al., 2001]. The approach uses the characteristic patterns to represent the individual unit cell 2D interior architectures, and assembles the individual characteristic pattern to form a 2D layered pattern for the scaffold. The processing tool path is generated for every layer based on the layered scaffold pattern, and is then applied to instruct freeform fabrication machines to build 3D scaffold layer by layer. In this way, we do not have to create an explicit 3D CAD based scaffold model, but with the implicit representation be able to design and control the internal architecture of the scaffold. Detailed development of the IAD approach is outlined as follows.

4.1.1. Process Methodology

Step 1: Determine the layered processing plane ($\varphi(x, y, z)$)

The 3D volumetric scaffold V is sliced into layers during the model decomposition, and stacked back with materials during the material accumulation in an ordered sequence. The sequence is a number dispersal in 3-dimensional space V in which the layered manufacturing process is realized. Let us introduce a finite discontinuous real number set C to indicate the discrete layers which V is decomposed:

$$C = \left\{ c_k; a \leq c_1 < c_2 < \dots < c_{k-1} < c_k < c_{k+1} < \dots < c_n < c_{n+1} \leq b, k = 1, 2, \dots, n \right\} \quad (4.1)$$

where subscript k represents the layer index in a total n layers, and constants a and b represent the values of lowermost and uppermost sequence for a particular object V .

Therefore, corresponding to each C_k , we can define a sequence function $\phi_k(x, y, z)$, and assume it is equal to the ordered number c_k , as shown in Figure 4.2(a), we thus define a series of planes in V :

$$\phi_k(x, y, z) = c_k, \quad k = 1, 2, \dots, n \quad (4.2)$$

We call those planes the layered processing planes and represent them by a set of scale function $\phi_k(x, y, z)$, with $k = 1, 2, \dots, n$. It is important to note that the layered processing plane $\phi_k(x, y, z)$ represents both the indication of the processing layer, and the layered exterior geometry represented by CAD model for the scaffold. In the model decomposition process, the layered processing planes intersect and slice the designed 3D scaffold. In the material accumulation process, the layered processing planes form the processing layers on which material will be added. For example, in the TheriForm fabrication process [Wu et al., 1996, Kim et al., 1998], the layered processing plane is the plane on which the fresh biomaterial powder is spread and printed, while in Drexel's multi-nozzle biopolymer deposition process, the layered processing plane is the plane on

which the biopolymer is extruded and deposited. The concept of the decomposition and accumulation, and the layered processing plane is further depicted in Figure 2.

On each thus defined layered processing plane $\phi_k(x, y, z)$ in the volumetric scaffold, we define S^k as a 2D layered scaffold pattern, which can be considered as unions of the partitioned unit cell characteristic patterns:

$$S^k = S_1^k \cup S_2^k \cup S_3^k \cup \dots \cup S_i^k \quad (4.3)$$

For simplicity, we assume that the thickness of the slicing layer for unit cells and for the scaffold are all uniform and the same.

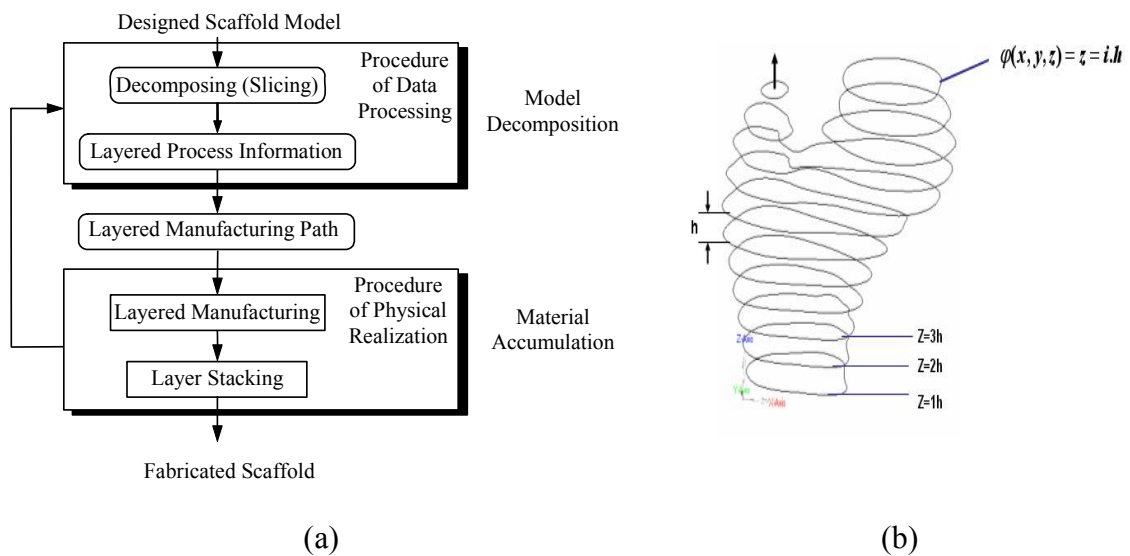


Figure 4.2: Decomposition and accumulation for layered manufacturing

The external shape of the scaffold is defined by Non-Uniform Rational B-Spline (NURBS) surfaces. We use a direct slicing method as described in Chapter 4 to

determine the intersection curves of the NURBS model with the given layer (k). Using the process, we can determine the layered processing plane ($\phi_k(x, y, z)$) and hence determine the outer scaffold shape.

Step 2: Generate Toolpath based on Internal Architecture Design (IAD)

The layered processing toolpath for freeform fabrication is then generated based on the 2D layered scaffold pattern. The above process can be briefly summarized into the following major steps:

1. Define sub-volume V_i (unit cell) and the spatial position P_i ; the discrete layers of V , layered thickness, and the layered processing plane $\phi_k(x, y, z)$ for scaffold exterior geometries (as defined in Step 1).
2. Determine the unit cell characteristic patterns S_i^j ($i = 1, 2, \dots, m$, and $j = 1, 2, \dots$) by slicing them;
3. Form a 2D layered scaffold pattern S^k ($k=1, 2, \dots, n$) (or layered Interior Pattern) for a given scaffold sliced layer by a union of all the unit cell patterns;
4. Perform a intersection Boolean operation $S^k \cap \phi_k(x, y, z)$ between the 2D layered scaffold pattern and the exterior scaffold geometry given by ϕ to remove the unwanted regions of the scaffold sliced layer;
5. Conversion of the Interior Scaffold Pattern to process tool path information for freeform fabrication.
6. Repeating Step 3 to Step 5 till $k = n$.

We use a square block type unit cells with open pore in the center (as shown in Figure 4.3 as examples to illustrate the above process. Assume that the designed scaffold consists of m unit cells with 4 unit cells being assigned to the top of the scaffold volume (Figure 4.3). Assuming that the number of slices of the scaffold has been determined, the layered processing planes $\varphi_k(x, y, z)$ ($k = 1, 2, \dots, n$) for the scaffold exterior geometry are known, and the characteristic patterns of the unit cells S_i^j corresponding to the $\varphi_k(x, y, z)$ have been computed and available in the database. The unit cell id P_i within different regions on this layer is used as a key to retrieve the appropriate unit cell characteristic patterns. A scenario has been illustrated as shown in Figure 4.4 by taking the case of 2 scaffold slice layers shown as slice layer 1 and slice layer 2. The 2D layered scaffold patterns for scaffold layer 1, S^1 , and layer 2, S^2 , are generated by union of four unit cell characteristic patterns S_i^1 and S_i^2 ($i = 1, 2, \dots, 4$), respectively and are shown in the right side of Figure 4.4. Printing maps consisting of the geometric raster pattern for the slice layer 1 and slice layer 2 are then generated based on S^1 and S^2 .

By applying intersection Boolean operation between the Interior Scaffold Pattern and the layered processing plane $\varphi_k(x, y, z)$, we then obtain the layered manufacturing maps which will be used for the process tool path generation. The tool path can be generated based on the particular SFF process used. The proposed algorithms is currently implemented in the 3DP™ based SFF technology with possible extension into contour based multi nozzle deposition system. The interior scaffold pattern is used as the initial starting point to generate a raster pattern by determining the entry and exit points for the print head in the case of the 3DP based machine. The calculated intersection points will serve as the starting point for the tool path information for a 3DP based SFF machine. For

vector contour based machines, the same scaffold pattern will be used to generate contour vectors by joining the intersection points in a linear technique and forming closed loop vector tool paths. The data flow chart is shown in Figure 4.5.

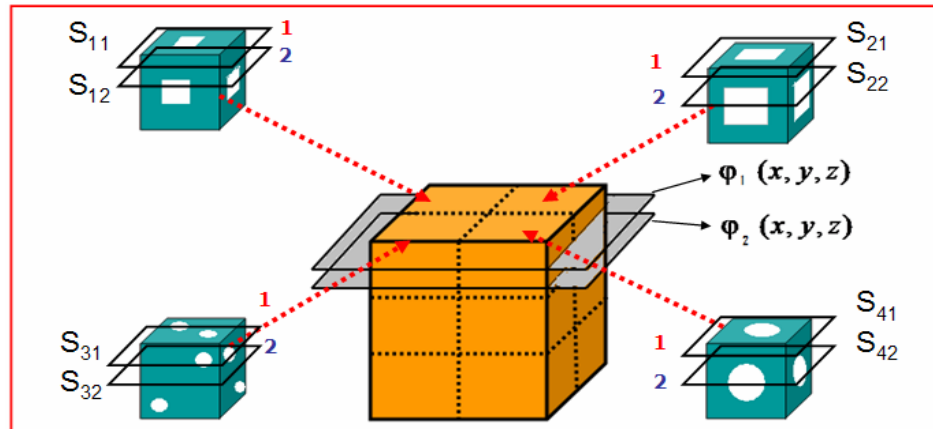


Figure 4.3: Slicing of Unit Cell and Scaffold and associating them to specific regions

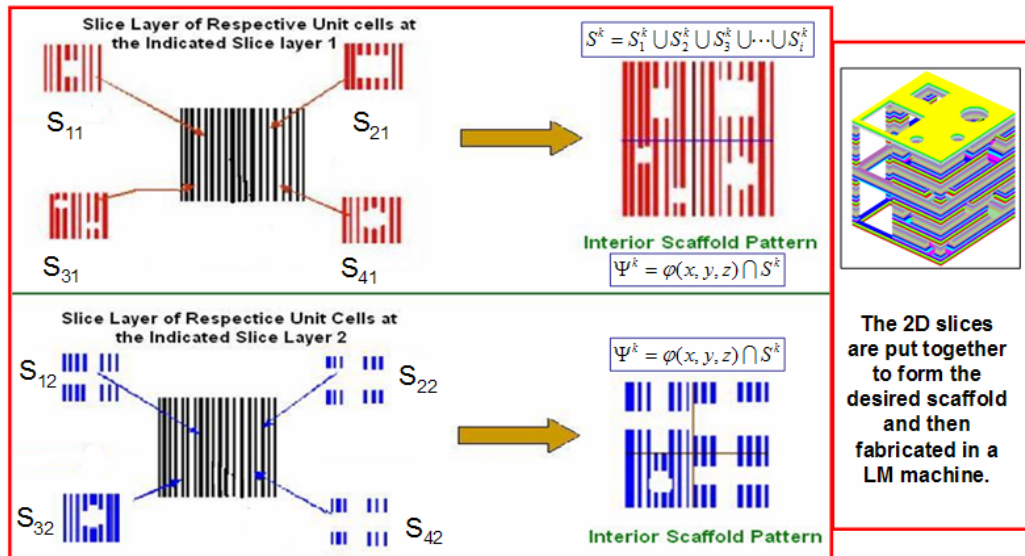


Figure 4.4: Intersection of 2D slice patterns onto Scaffold 2D pattern to form 3D structure

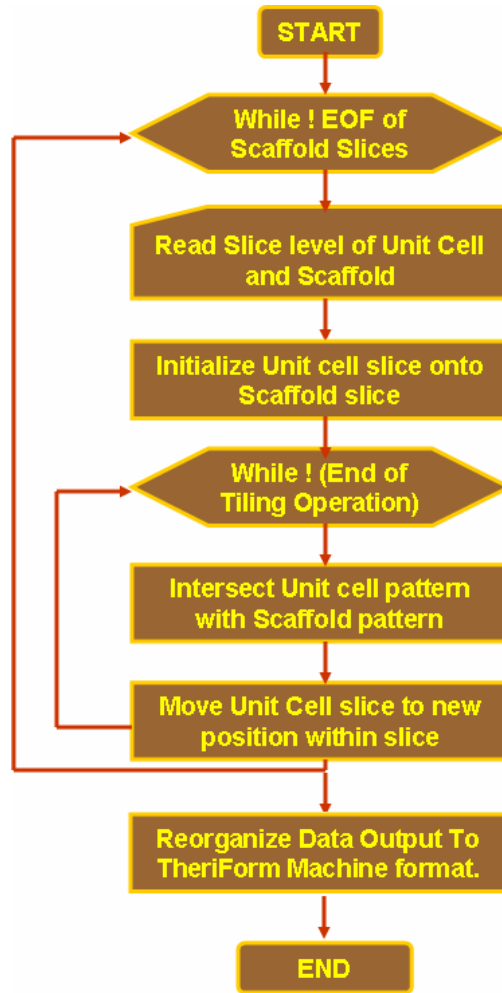


Figure 4.5: IAD algorithm

4.2 Design Manufacturing Interface

A sample process-planning scenario to design and fabricate tissue scaffold structures is depicted in Figure 4.6. In the custom implant planning stage, the CT/MRI images of the defected region are obtained and reconstructed by the method as we have already outlined in the previous section. Through reverse engineering techniques, a CAD model of the region of interest is made. Simultaneously, mechanical characterization techniques would be employed to obtain the mechanical properties of the region to be

replaced. Based on the characterization process and biological requirements, an appropriate unit cell is designed and along with constructive heterogeneous solid geometry techniques an appropriate scaffold structure obtained. The CAD file is then converted to a STEP file format with designed geometrical and material information. Using an appropriate 3D modeling kernel, the scaffold implant reconstructed from the STEP definitions is then sliced depending on the slice parameters set using the slice module of the software. The slice module based on the direct slicing approach (Chapter 3 of this thesis) would work based on the B-rep structure in the STEP file. The slicing is achieved by the ray-casting method where the object is sliced by a series of parallel planes and each plane having rays cast out across them. The intersection points of the ray with the object define an entry point and exit point. A set of these points defines raster lines. The slicing module defines the slice layers as scan raster lines to support the open-end architecture that is required for the scaffold structures. Once these scan lines are defined, complete information that consists of the slice layers as well as the material information is stored in a print job database that serves as a temporary storage as well as for future retrieval. The scan lines are converted to machine code instructions, which are then sent to the machine for fabrication.

The steps and algorithms outlined above are implemented within a fabrication planning software to control the different parameters of the fabrication process. The algorithms are implemented in Microsoft's .NET development environment using C# as the programming language. Figure 4.7 gives the different component modules with the functional flow of data within the fabrication preprocessing environment.

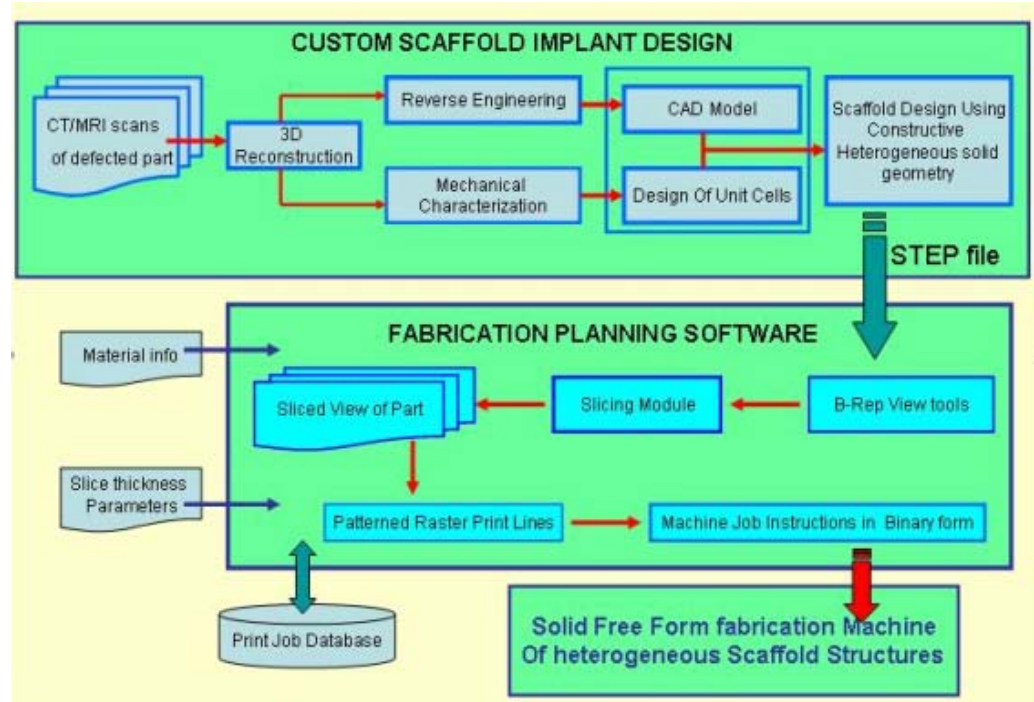


Figure 4.6: Flowchart of process planning for fabricating tissue scaffold

Slicing Module: Once the STEP file of the Scaffold CAD model is read, its geometry and topology will be maintained by the 3D Kernel by which the NURBS surfaces of the model with their topology information will be extracted for the slicing process. Direct slicing of the NURBS surfaces is performed by a Slicing Module, of which the results are packaged into a Slicing Object. The B-rep features of the model are viewed using graphic kernels for easier manipulation and display. Tools are provided for viewing the model and verifying slice layer information for errors that may result in erroneous fabrication. Each cross sectional layer is then extracted from the model based on the slicing parameters and then converted to machine job instructions. A print job database is also maintained for database records and future retrievals.

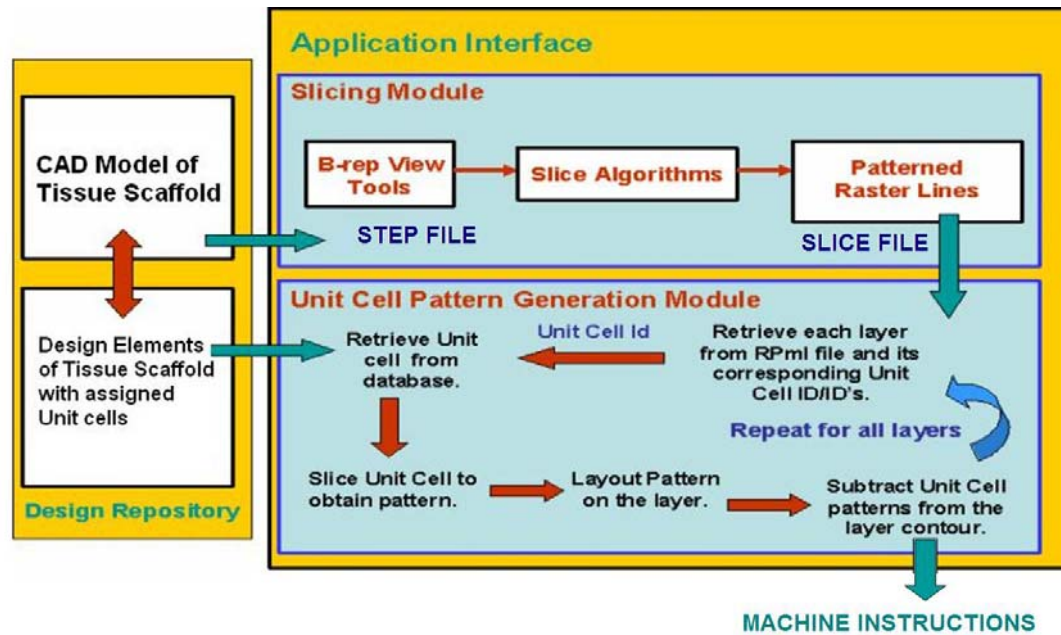


Figure 4.7: Fabrication Planning Modules

Unit Cell Pattern Generation Module: The slice file (containing tool path) from the previous module acts as the input file in this stage. Each layer is extracted from the file along with the microstructure cell ID/IDs it is associated with. The unit cell corresponding to the unit cell ID is retrieved from the design repository and is sliced to obtain the 2-D unit cell pattern. This unit cell pattern is then layered out onto the retrieved layer through a pattern generation algorithm as explained in Figure 4.4. Once this is completed, the new pattern is intersected with the original pattern of the CAD model retrieved from the slice file to obtain a new set of pattern raster/contour lines. These new set of patterns can be stored in a new machine file format that which are then converted to machine job instructions to run an SFF based RP machine. The flowchart described in Figure 4.7 describes the process flow information pathway. Two loops

control the process. While the outer loops reads in the scaffolds slices, the inner loop reads in the appropriate unit cell patterns and performs the tiling and intersection operation. At the end of the complete patterning and intersection operation, the data is reorganized and transformed to bring it down to machine level instructions.

4.2.1. Case Study Models

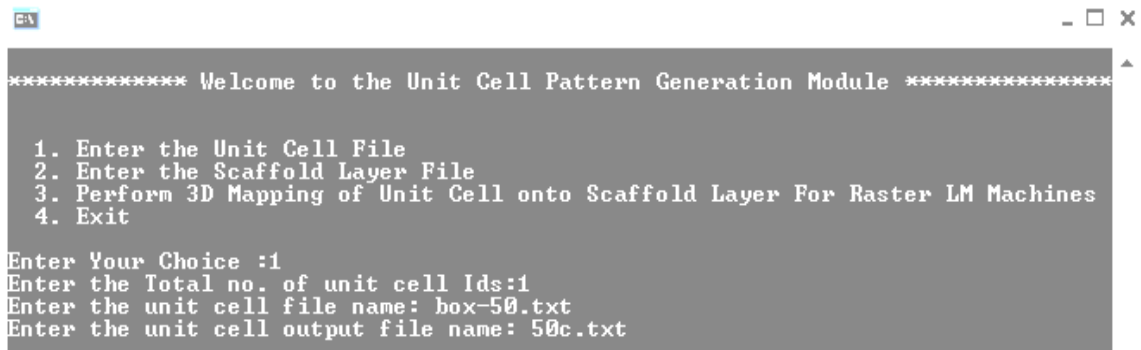
The developed algorithm was tested for 7 different kinds of models each with certain characteristics of its own to test the capability of the algorithm. The algorithm was tested with a couple of simple to complex models as shown in Figures 4.10-4.16. The size of the selected unit cell is arbitrarily selected to be a 5mm cube with characteristic shapes of either a square pore or a cylindrical hole within them. The blocks define the outer shape of the scaffold while the unit cells define the interior architecture of the scaffold. Both the blocks and the unit cells were sliced at equal intervals and stored in files. Given below are the test case results and its various process parameters. Model #1 has been explained in detail on how to run the algorithm right from the initial slice input to final print instruction display.

Model #1 – Square Unit Cell with Square block

Step 1: Unit cell Input

Select the first choice to enter in the unit cell information (Figure 4.8). The program prompts for the total number of different unit cells that are assigned to the different regions in the model. Enter in the appropriate number, say N. The next prompt would be

the file name of the unit cell slice file. This slice file would be in a specific input format and should be present in the working directory. The program prompts for the 'N' unit cell file names. It also simultaneously asks for the output file name for the file after processing of the unit cell info.



```

***** Welcome to the Unit Cell Pattern Generation Module *****
1. Enter the Unit Cell File
2. Enter the Scaffold Layer File
3. Perform 3D Mapping of Unit Cell onto Scaffold Layer For Raster LM Machines
4. Exit
Enter Your Choice :1
Enter the Total no. of unit cell Ids:1
Enter the unit cell file name: box-50.txt
Enter the unit cell output file name: 50c.txt

```

Figure 4.8: Unit Cell Input Files Interface

Step 2: Scaffold File Input

After the unit cell slice information have been passed into the program, the program then prompts for the main menu and in this step, choice #2 is selected to pass in the scaffold slice information. The program prompts for the scaffold slice file name and this again should also be in the working directory.

Step 3: Begin 3D Internal Design Process Command

At this stage, both the unit cell and scaffold file info have been passed in. The next step is to begin performing the mapping of the unit cell onto the scaffold and prepare the output file for the TheriForm machine. Fig 4.9 gives the process that would be involved. At the end of the mapping process, the program prompts for the ray increment and slices level increment within the unit cell and scaffold files. The values entered in

should be similar to the ray increments and slice increments present in the input files. After the values have been entered, the program performs a reorganization of the output data after which the data is converted to the required TheriForm info. The results are displayed in Figure 4.10

```

1. Enter the Unit Cell File
2. Enter the Scaffold Layer File
3. Perform 3D Mapping of Unit Cell onto Scaffold Layer For Raster LM Machines
4. Exit
Enter Your Choice :3
Reading At level :0 ... complete
Reading At level :0.5 ... complete
Reading At level :1 ... complete
Reading At level :1.5 ... complete
Reading At level :2 ... complete
Reading At level :2.5 ... complete
Reading At level :3 ... complete
Reading At level :3.5 ... complete
Reading At level :4 ... complete
Reading At level :4.5 ... complete
Reading At level :5 ... complete
Reading At level :5.5 ... complete
Reading At level :6 ... complete
Reading At level :6.5 ... complete

```

Figure 4.9: 3D Unit Cell mapping process command window

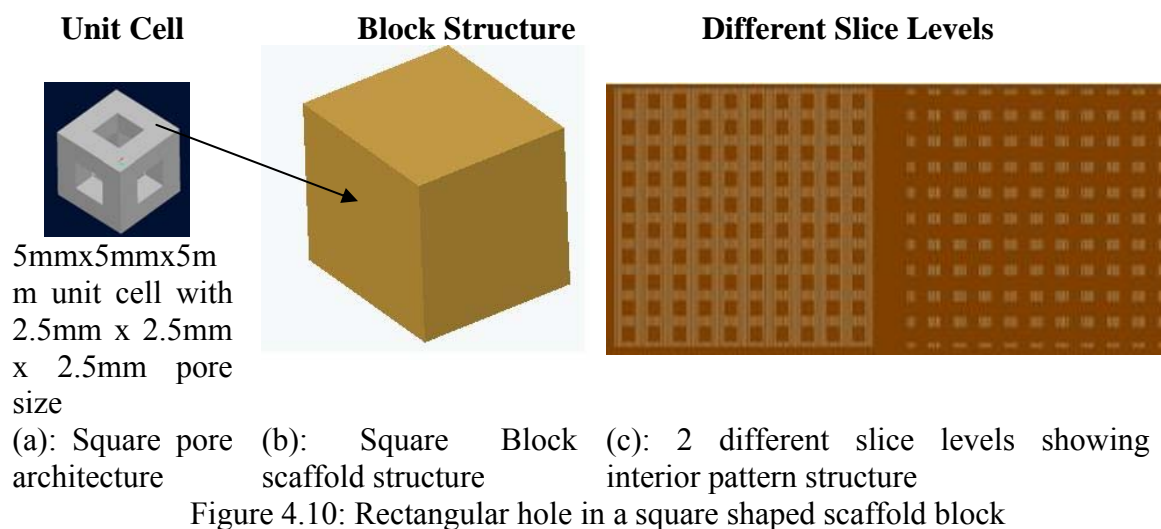


Figure 4.10: Rectangular hole in a square shaped scaffold block

Model #2: Circular Unit Cell assigned to a Cylinder scaffold

In this model, curvature models have been tested. As shown in Fig 4.11, the circular patterns have been mapped into the cylindrical scaffold in a well uniform manner. The culling of the unit cell on the outer edges of the model is important to ensure proper interconnectivity within the scaffold.

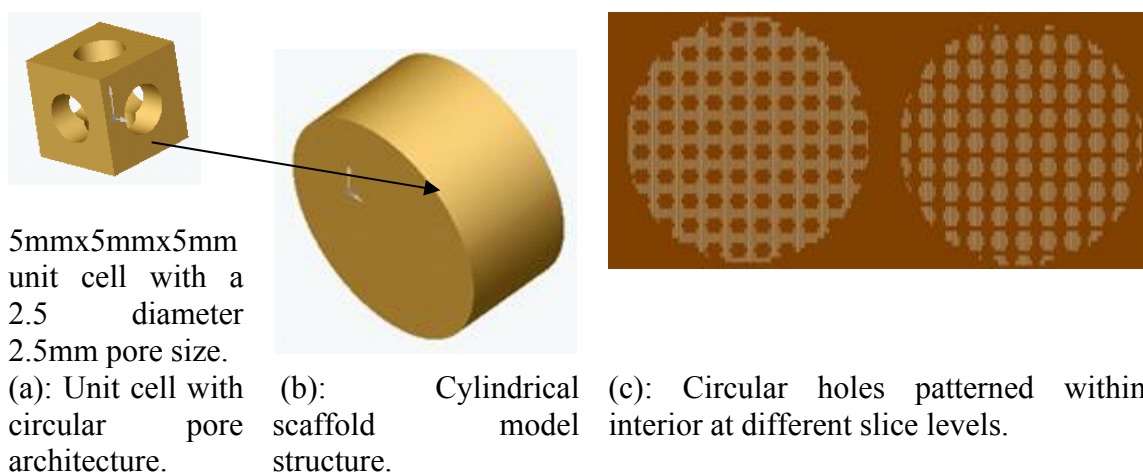
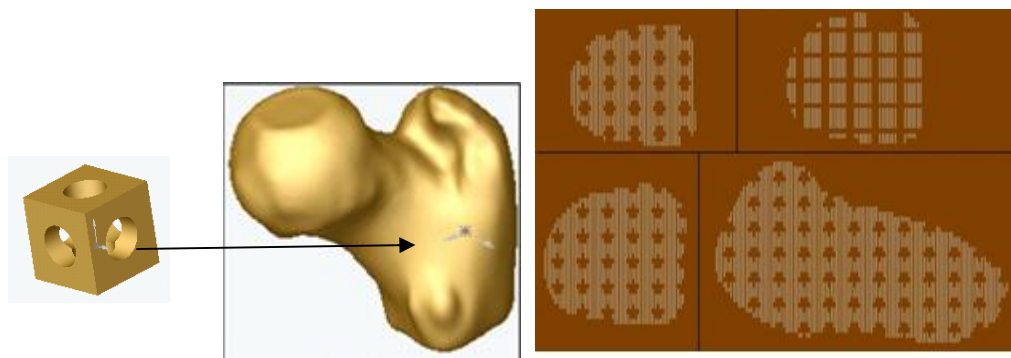


Figure 4.11: Circular hole in a cylindrical scaffold

Model #3: Circular Unit Cell assigned to a Bone Architecture scaffold.

This model case study tests the ability of the algorithm to position itself correctly when the scaffold slice levels change. The results displayed in Fig 4.12 show the pattern at four different slice positions within the final scaffold. The unit cell positions do not change and always ensure a through hole connectivity within the scaffold.

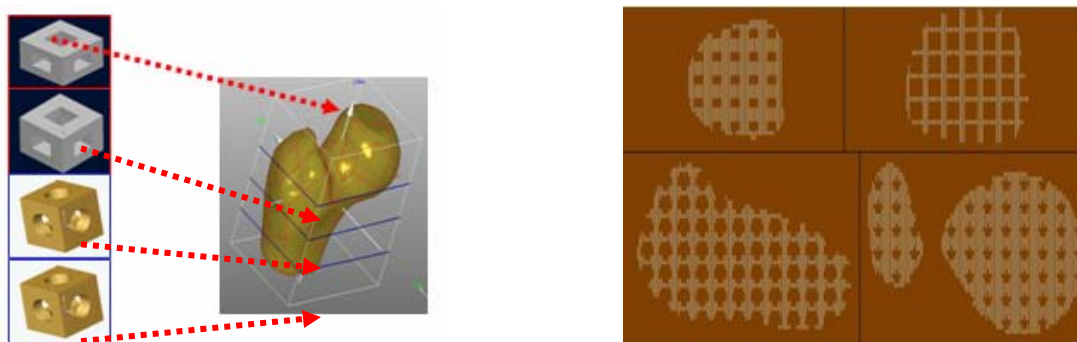


(a): A circular pore architecture unit cell structure. (b): Irregular model structure such as Bone. (c): Four different slice levels of the bone scaffold structure showing circular holes.

Figure 4.12: Circular hole in a bone structure

Model #4: Multiple Unit cell Architecture assigned to the Bone structure

In this case study, the bone had been divided into 4 different sections. Each section is grouped together to form an assembly and is assigned a specific unit cell. Based on the id that each section has been assigned, during the mapping stage, the appropriate ID is retrieved and patterned onto the slice file. Fig 4.13 shows the four different interior architectures present at different slice levels of the bone structure.



(a): Bone structure divided into four different levels with 4 unique unit cell structures assigned. (c): Four different slice levels showing four different unit cell patterns.

Figure 4.13: Multiple unit cell architecture in the bone structure

Model #5: Multiple Patterns within a single slice

In this case study, we have two different unit cell architectures that are assigned to a single slice layer. As seen in Fig 4.14, a circular unit cell has been assigned to the cylindrical sub-region of the scaffold, while a square scaffold has been assigned to the rectangular block region of the scaffold. As seen in Fig 4.14, multiple patterns exist within the single slice layer. Also note the sudden change in architecture at the interface region of the two sub regions.

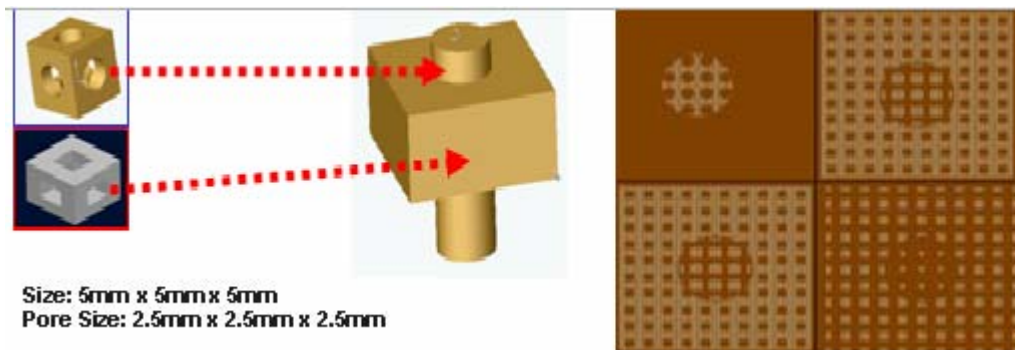


Figure 4.14: Two different pore architectures assigned to a model structure with multi patterns in a single layer

Model #6: Sweep regions within Scaffold

This model shown in Figure 4.15 particularly shows how complex internal architectures can be achieved quite easily with no complicated CAD operations. Such internal architectures are impossible to be designed with conventional CAD software. Two unit cells architectures have been assigned to sweep like sub regions within the scaffold.

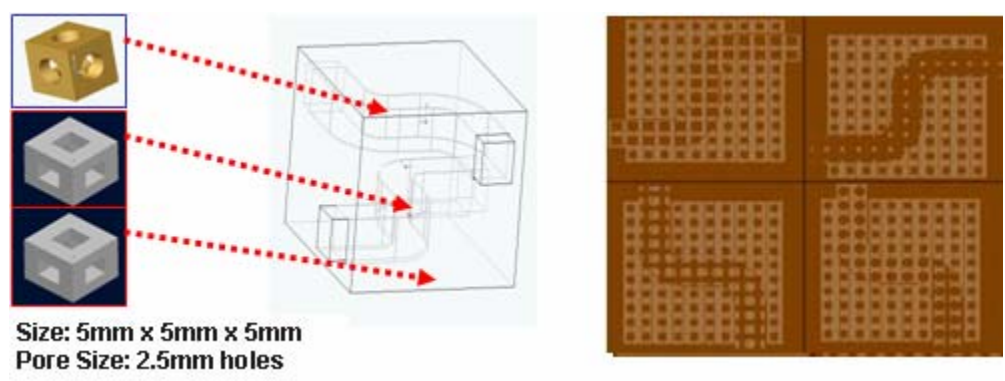


Figure 4.15: Three Pore architectures assigned to a shaped scaffold

Model #7 – Area Selection Criterion

This particular model shows a unit cell architecture assigned to a cone model. An area selection criterion has been applied. If the area of the scaffold slice layer falls within a preset value, patterning does not take place and is left alone. This type of scenario may be useful when considering the structural integrity of small features within the scaffold. The algorithm however does not work for multiple small features within the model. It calculates the entire area of the slice level based upon which decision to pattern or not takes place.

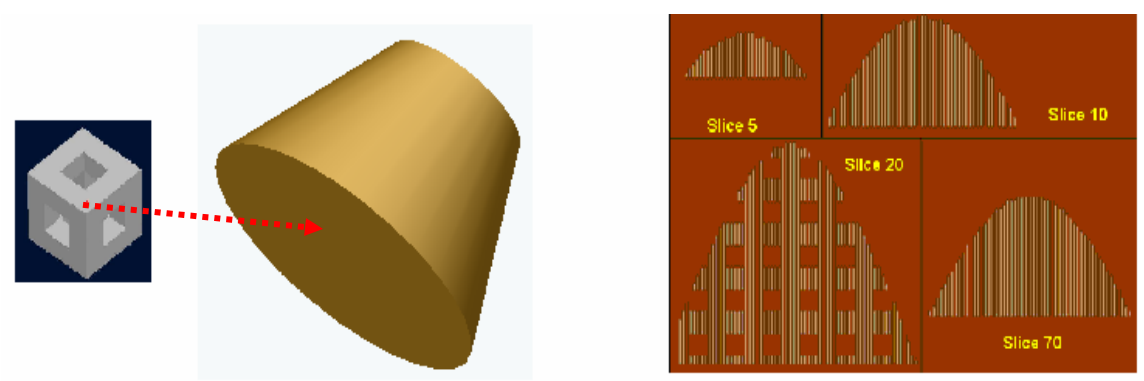


Figure 4.16: Slices 5, 10, 70 do not meet the area selection criterion and hence no patterning is observed

The developed algorithm does not require any huge memory requirements and its run time only depends on the number of slices that make up the block. The size of the unit cell can go further smaller and its size is selected depending on other factors such as the desired pore size, the capability of the selected RP machine and material particle size.

4.3 Fabrication using 3DP™ and PED Systems

4.3.1. 3DP™ System: TheriForm™

Models in Figures 4.11 and 4.12 have been fabricated using the TheriForm fabrication machine. The principle of operation works similar to that of any 3DP based RP machine and is shown in Figure 4.17. The powder bed consists of a biomedical grade material which is fused together by heat and a binder solution. Each layer in the build bed is incrementally pushed up by a fixed slice thickness depending on the type of material used, surface finish and accuracy needed, functionality of the required product. The nozzle through which the binder ejects is controlled by an x-y positioning system which is in turn controlled by the machine instructions generated from the models to be fabricated. In this case, the IAD algorithm generates the machine level instructions for fabrication of the internal micro-architecture of the models. Each entry and exit point defined by the ray instructs the machine to start and stop dropping the binder respectively. Deposition of binder in one complete layer defines the material space for the model in its current layer and the process is repeated until all the layers have been fabricated.

Figures 4.17(a) and (b) shows a cylindrical shaped and a bone scaffold designed using the IAD methodology and fabricated using the TheriForm™ machine. The

scaffolds were made out of alumina with a slice thickness of 0.48mm and sintering temperature at 80C. As can be seen, the scaffolds have the required internal architecture as defined by the unit cell. A CAD model of the entire model with all the complete pores in them do not exist but merely an association made Redefinition of the unit cell model architecture results in a different interior structure for the scaffold models.

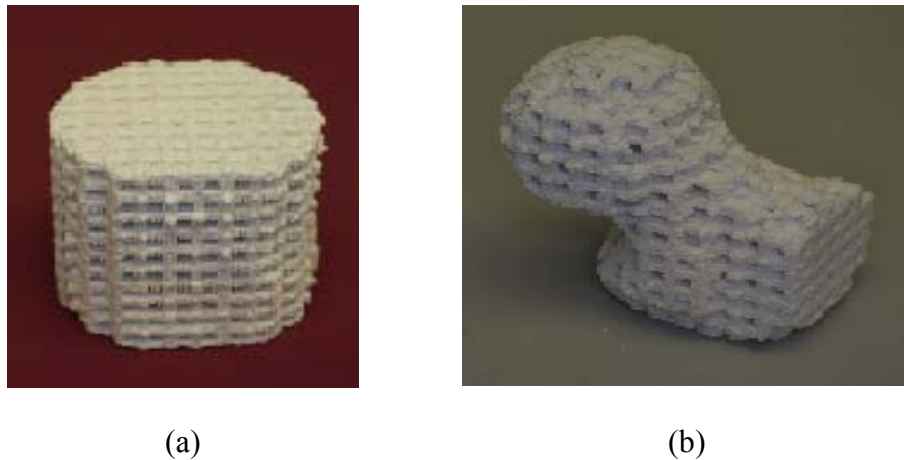


Figure 4.17: Cylindrical and bone shaped scaffold

4.3.2. Precision Extrusion Deposition System

The interior architecture concept has also been implemented in the Precision Extrusion Deposition system that has been developed at Drexel University. The basic set of operations works similar to the FDM concept, except here, no filaments are required and material can be added in the form of pellets or powder. This difference helps in avoiding filament preparation steps and aids in selecting more candidate materials for scaffold fabrication. Due to the extrusion process, possible interior architecture are different and only a certain class of unit cell architectures can be used. We have used poly-e-caprolactone (PCL, Sigma Aldrich, Inc., Milwaukee, Wisconsin) to demonstrate

the design of the space filling curves and heterogeneous patterns. The PED system consists of an XYZ position system, a material extruder system, a temperature control system, a data processing and system control software. The nozzle through which the material is extruded is controlled by the x-y positioning system which is in turn controlled by machine instructions generated from the models to be fabricated. The system control software monitors the deposition of material through the material extruder system according to the process tool path layer-by-layer to construct 3D porous scaffold. Samples of the designed scaffold with the space filling curve with feature sizes of around 250 μ m scale level are shown in Figures 4.18.

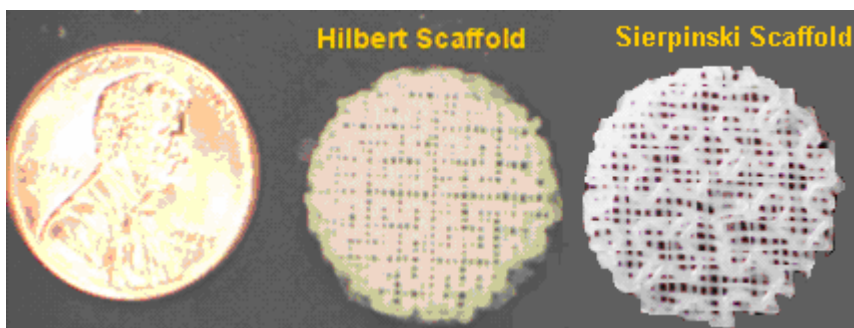


Figure 4.18: The Hilbert and Sierpinski Patterned Scaffold

In addition, using the tools developed, we have also implemented new patterns that produce different internal structures. For example, Figure 4.19 shows a spiral pattern with alternating structures having circular roads passing through the internal structure. Circular struts exhibit a different surface morphology and a different level of micro-stress characteristics than road struts that are extruded in straight lines. This can possibly change the cellular response when cells adhere and grow on the surface during in-vitro studies providing an insight on whether micro-stress plays a role in cellular growth. Figure 4.20 presents a pattern with varying porosities within the structure. This kind of pattern can most certainly mimic bone structure in terms of the highly porous cancellous

core and the highly dense outer cortical structure. These patterns if used in cell studies can help in the study of cellular behavior at interfaces that show a sudden change in morphology.

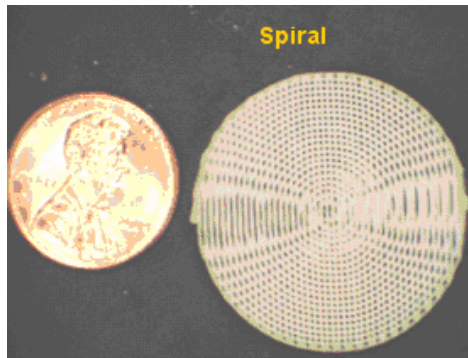


Figure 4.19: PCL scaffold with spiral pattern

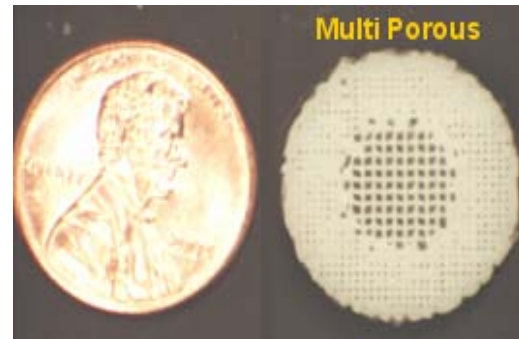


Figure 4.20: Multi-porous regions in the PCL scaffold

4.4 Conclusions

The developed IAD methodology facilitates the creation of more advanced scaffold designs that cannot be achieved using conventional CAD since each layer can individually be designed to have the desired layer pattern. This pattern is obtained from the assigned unit cell to the scaffold outer architecture to form the desired scaffold. With the combination of all layers put together, the selected interior unit cell architecture is fabricated within the scaffold structure. The advantages of this design process include:

- The developed approach can help in the design of scaffolds with complex interior architectures which by current techniques are impossible to create using CAD software or other 3D software. The developed approach does not exclude the use of

commercial CAD software but uses it as an ancillary tool in the design of scaffolds with macro and micro architecture.

- The interior architecture of scaffolds can be designed and controlled along with the provision of multiple material specifications by associating the information to the unit cell. During the pattern layout stage, the information is translated to instruction set that can recognize the different materials regions;
- Direct transfer of CAD model data to RP machines avoids the bottleneck inherent in the use of the STL format.
- The design of outer scaffold shape and the design of its interior are separated and hence do not present a memory overhead for CAD software. By separating their designs, new architectures with varying properties can be designed and hence aid in the fabrication of better scaffolds for tissue engineering applications.

The 2D characteristic patterns from the IAD algorithm are designed with a reason and are generated from the unit cells that have been pre-selected. The unit cell that is assigned within the block (scaffold) structure is selected based on factors such as the required mechanical and biological properties which have already been pre-defined. The IAD process defined here assumes that this selection process has been carried out prior to the generation of process planning instructions. Further details into how these unit cells are selected are described in Sun et al and the readers are referred to them.

A point that we do not like to disregard is the notable limitations of the process. The IAD approach described here presents an implicit evaluation of the CAD model. The entire scaffold assembly is defined by stand alone CAD models with the unit cells being referenced into the interior of the scaffold. This process, therefore, will not result in an

explicit CAD model and hence cannot be used for visualization purposes. The user will not be able to visually see the final scaffold in 3D and the “final product” is only seen after fabrication. This may result in costly errors especially when multiple complex unit cells have been used in the interior architecture. However, the application interface helps to avoid such errors by providing tools for the visualization of the 2D patterns that make up the scaffold. One of the major advantages of having a CAD model is being able to use it in downstream FEA analysis packages. Due to the unavailability of an explicit CAD model, scaffolds designed using this IAD approach cannot be subjected to FEA techniques in the conventional manner. However, an indirect method of analysis for effective property characterization can be done using homogenization based theories [Fang et al, 2005].

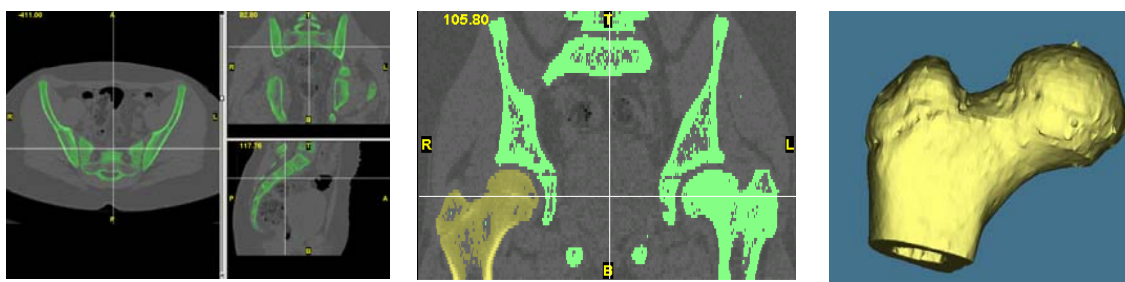
The IAD process described in this paper facilitates the fabrication of heterogeneous models in the structural sense by the inclusion of heterogeneous unit cells. Using a combination of different material architectures within the same structure, true heterogeneity with respect to material and structure can be achieved. By assigning specific material information for each unit cell, the process unlike STL based methods will carry this information throughout to the point of fabrication. A framework for heterogeneous modeling has been formulated [Sun et al., 2000, 2002] and a future extension of the IAD process may be to incorporate material heterogeneity within the scaffold structure. Process planning instructions generated from the IAD algorithm will then be able to fabricate them using scaffold bio-fabrication systems [Khalil et al., 2005]. The described process can be further extended to generate process planning instructions for contour based RP machines such as the FDM and PED. Although the library of unit

cells that can be fabricated with these machines are limited, the authors believe that by proper selection of varied contour patterns and sizes, the desired scaffold properties can be obtained. The IAD process developed for the TheriForm™ machine will further extend its reach to include contour based SFF machines capable of fabricating scaffolds with new biopolymer materials and in micron ranges.

CHAPTER 5 : APPLICATION EXAMPLES FOR VIRTUAL RECONSTRUCTION AND PROTOTYPE MODELING

5.1 A CT/MRI Based Reconstruction of Anatomic Parts

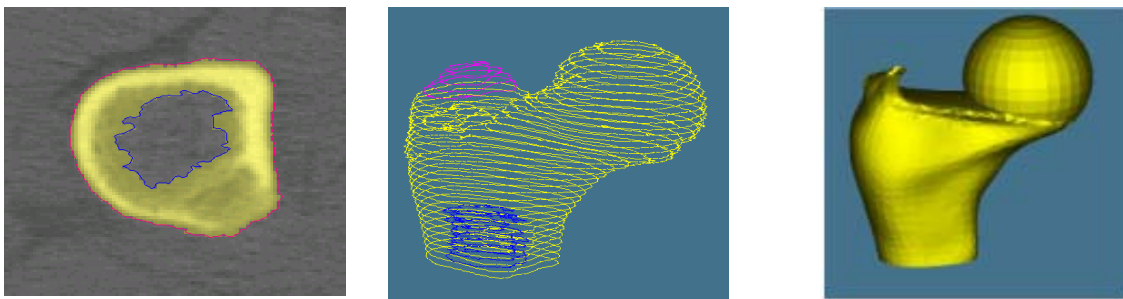
This study used the CT images of a proximal femur bone from a small child. In all, 34 slice images were obtained with each of 2mm sliced segmentation for a height of 68mm. Once loaded into the MIMICS software, all images were properly registered and aligned for its orientations (Figure 5.1(a)). Next, the region of interest (ROI) was identified and a 3D voxel model of the femur was made. In doing so, an appropriate threshold range was found that could best capture the relevant information contained in the femur. Using this threshold value, all pixels within this range were collected to a color mask within the given segmentation level (Figure 5.1(b)). A region growing technique (available in the software) was applied to form a 3D femur anatomic representation (Figure 5.1(c)).



(a) CT images are loaded into and properly registered b) ROI is identified as appropriate differentiating color mask. c) 3D voxel-based femur model

Figure 5.1: Image Registration, 2-D segmentation and 3-D reconstruction process

All three different process paths described above were used to test the CAD model generation. Results are shown in Figure 5.2 (MedCAD interface approach), Figure 5.3 (reverse engineering approach) and Figure 5.4 (STL converting approach), respectively. In the MedCAD example, we have used both primitives and freeform shapes (B-spline) to model the femur anatomy. Since there was a lack of appropriate primitive features, a sphere primitive feature was used to represent the top of the femur.



(a) Polyline contours used to demarcate boundary (b) Polyline were grown through the segmented images (c) B-spline surfaces and primitives (sphere) used to construct the model

Figure 5.2: CAD model construction using MedCAD interface

Figures 5.3(a) to 5.3(f) show the process of using reverse engineering approach to construct a 3D femur model. The imported points from the 3D voxel model (Figure 5(c)) first need to be cleaned in order to eliminate the noise points. A decimation of points sometimes is also necessary depending on the number of the initial points (Figure 5.3(a) and 5.3(b)). The points are then triangulated to form a faceted model (Figure 5.3(c)). Further surface refining and enhancement (Figure 5.3(d)) is often required for reducing the file sizes and unwanted features. Figures 5.3(e) and 5.3(f) show the NURBS patches used to fit across the outer shape of the model.

Due to the limitation of STL in representing geometry with small, detail and complex features, the CAD model of the femur bone was not well reconstructed as shown in Figure 5.4. To overcome this, we need to refine the surface by adding more triangles in STL before the modeling process, or to edit the surface in a CAD environment after the initial model being constructed. In either way, this can lead to a very time consuming process. For models that do not involve complicated features, the STL interface approach can be used to efficiently generate CAD models.

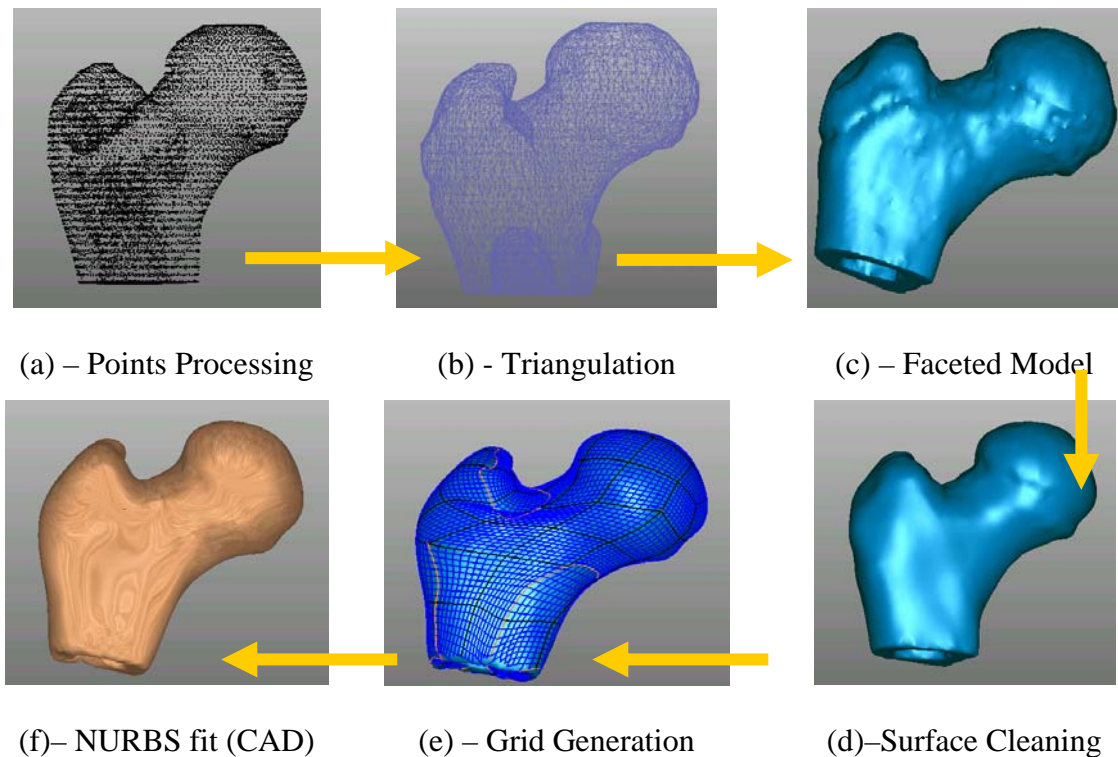
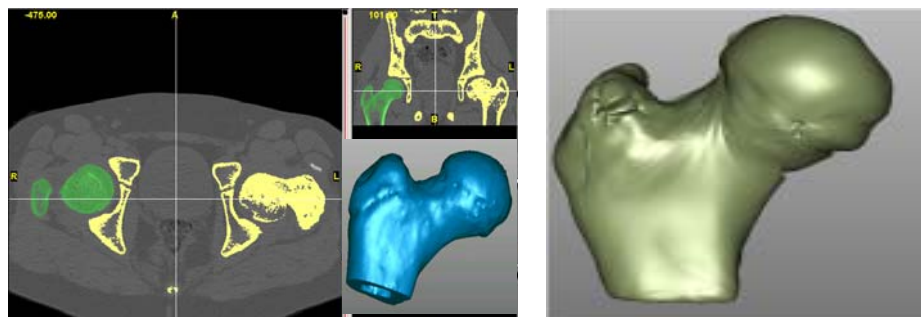


Figure 5.3: CAD model construction using reverse engineering approach



(a) Voxel model converted to STL based models (b) Improper reconstruction from STL based models

Figure 5.4: Conversion from Voxel Model to CAD model via STL interface

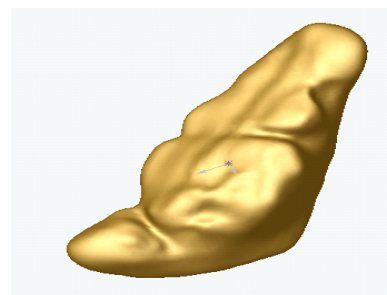
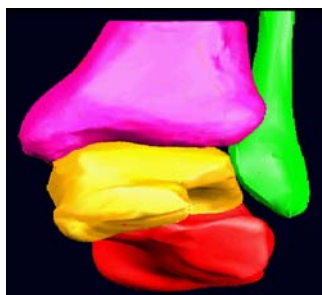
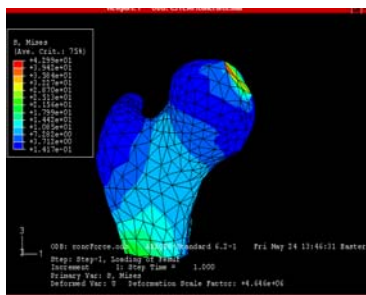
As can be seen from Table 2, the MedCAD process can be used if the available primitive is applicable. The reverse engineering approach is a preferred modeling approach because of the accuracy, structure fidelity, and the versatility in data transfer to STEP or IGES. The STL process is suitable when medical rapid prototypes need to be made as long as the STL format remains to be the industry standard for medical rapid prototyping. A comparison of three approaches for construction of the femur CAD model is given in the following Table 5.1

Once the CAD models are generated and saved in an IGES or STEP format, these can be used for a variety of other different down stream design applications. For example, the femur bone can be used to design patient specific hip implants using CAD software. A particular example is detailed in where the CAD model of a knee was used to design a knee implant. The CAD model can also be used for FEA or dynamic force analysis using CAD based software. Figure 5.5(a) depicts a stress analysis performed on the femur bone using FEA software ABAQUS and Figure 5.5(b) gives an example to show the CAD model of the hind foot reconstructed from CT/MRI images was used for dynamic force analysis using ADAMS™. Figure 5.5(c) displays a sinus graft model that was designed

based on CAD model reconstructions of the sinus region. All of these models were generated using point cloud data and reconstructed to form a CAD model using NURBS surfaces.

Table 5.1: Process Comparison – Conversion from CT/MRI images to CAD of the proximal femur

Process	Qualities	File Size Comparisons	Overall
MedCAD interface	Easiest and quickest, but may not be suitable for complex models.	file sizes is small only IGES conversion IGES : 266KB CAD (Pro-E) : 309KB	Poor
Reverse engineering interface	A longer process but suitable for complex shapes since control is achieved at every level.	Initial file sizes in the point form are not high but final CAD model may involve comparatively higher file sizes. Point : 256KB (7732points) IGES : 266KB (102 NURBS patches) CAD (Pro-E) : 298KB	Best
STL interface	Quick method to arrive at a CAD Model but may not work if triangulated surfaces contain errors.	Initial STL file size maybe high resulting in more CAD model IGES file size. STL : 1.82 MB (38252 triangles) IGES : 9.83MB (2316 NURBS patches) CAD (Pro-E) : 10.3MB	Average



(a) FEA analysis of femur using ABAQUS™

(b): Dynamic analysis of hind foot using ADAMS™

(c): Sinus graft model designed with the help of CAD

Figure 5.5: Models generated for downstream CAD applications

5.2 Real Time Surgical Planning and Quality Control

Despite scientific advances in our understanding of the biology of the craniofacial skeleton and its associated tissues and despite many technological advances in imaging and instrumentation, the surgical correction of the deformities associated with craniosynostosis remains a craft. With each particular case, based on aesthetic sensibility and technical experience, the surgeon must make qualitative and quantitative judgments regarding which features of the deformity require correction and how much correction to attempt. Modern digital technologies have the potential, however, to put preoperative planning and surgical execution on a quantitative footing through the marriage of extraoperative simulation and intraoperative image-guidance. We report a single case that illustrates a particularly simple example of such a marriage employing a method not previously described for transfer of the simulated reconstruction into the clinical environment.

The patient's data is obtained using any of the standard image acquisition systems such as CT/MRI. These images are then imported into medical image processing software capable of reconstructing the patient's anatomy. This model is then used as the basis for virtual reconstruction using any of the available STL manipulation software. At this stage, both the surgeon and CAD operator would work in unison to virtually reconstruct the skull. After this has been accomplished, the STL model is then prototyped using any of the available rapid prototyping systems. After the model has been fabricated, the reconstructed prototype model is then rescanned using a CT machine with same parameters as the original CT scan. The new image dataset is then superimposed on the original data set so that differences between the two can be measured and identified. This

new image data set is also imported into an image guided surgical system that would allow a real time evaluation of the procedure during surgery. The following section describes the process in detail.

5.2.1 Virtual Reconstruction

A 7-year-old male child was brought to attention by his mother because of a facial deformity. There was flattening and recession of the left inferior frontal region and superior orbital margin. The orbital margin was elevated. There was a prominence in the left temporal region. The nose was rotated clockwise in the plane of the face as viewed by the examiner. There was no significant deformity of the right frontal or orbital regions. The clinical diagnosis was anterior plagiocephaly due to left coronal synostosis. The degree of the deformity was relatively mild, and in view of the patient's age, correction of the inferior frontal flattening with an on-lay bone graft and hydroxyapatite paste was planned.

Computed tomographic (CT) scanning of the head was performed with 1.5mm cuts and 3-dimensional reconstruction thereafter. The imaging dataset was transferred to a commercial neurosurgical image-guidance workstation (VectorVision®; BrainLAB AG, Heimstetten, Germany) over the hospital's local area network (LAN), where it was saved as a DICOM file on a Zip disc without any patient identifiers. On a workstation outside the operating room, the DICOM file was imported using medical image processing software MIMICS® (Materialise Inc) where in all images were imported, stacked upon each other and registered for its orientations. The region of interest was identified by appropriate color masks and grown into a 3D voxel representation of the

deformed patient's skull. Figures 5.6 gives two different views of the 3D rendered voxel model.

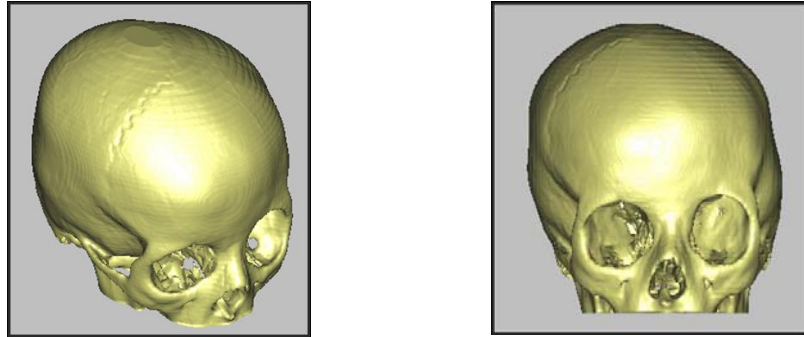


Figure 5.6: Different views of the voxelized skull model

The voxelized model was converted to an STL based format and imported in the STL manipulation software MAGICS RP® (Materialise Inc) where the model was used as a starting point for the virtual reconstruction. The STL model was modified in terms of cutting out unwanted regions of the skull and smoothing out the surfaces to reduce the number of triangles and hence computer memory usage. The patient's right side has been used as template for reconstructing the left side of the skull. The surgeon identified a midline plane along the nose-bridge. The deformed left side of the representation was deleted and the relatively normal right side was reflected across the midline plane to create a mirror representation, which was fused with the original right hemi-image to create a symmetrical, digitally reconstructed skull. The process is shown in Figure 5.7.

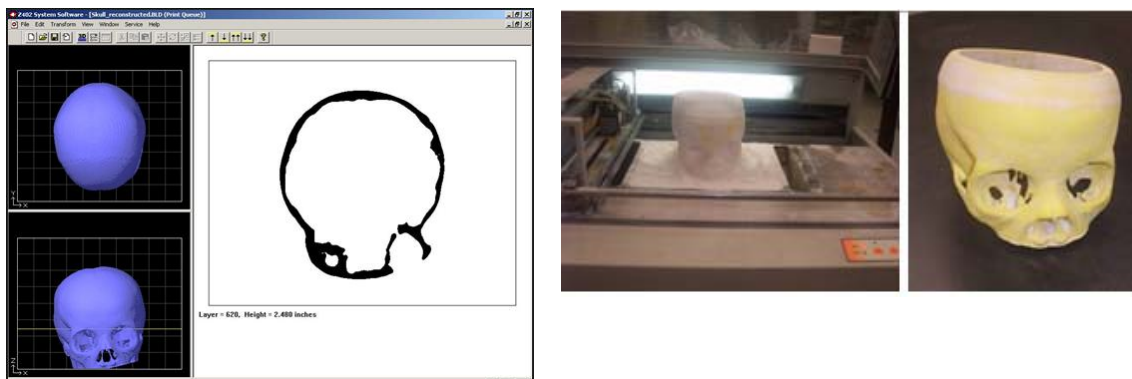


(a): Relatively good half is mirrored across a defined mid-plane. (b): Reconstructed model with better symmetry on the patient's forehead region.

Figure 5.7: Virtual reconstruction process

5.2.2 Quantitative Assessment

The goal of the prototype creation of the digital reconstruction was to serve as an intraoperative template for application by means of the image-guidance system to be used during surgery. However, the CAD software package did not allow for the reconstructed dataset (skull model) to be saved as a DICOM file readable by the image-guidance workstation. A physical transfer of the reconstruction was therefore undertaken. The reconstructed dataset was transferred to a three dimensional printer (ZCorp 420 3D Printer; Z Corporation, Burlington, MD), and a plaster model of the virtual reconstruction was created (Figure 5.8(a) and (b)). The model was fabricated in a laminar fashion by the printing of 0.076mm axial cross-sectional layers over 16 hours. Plaster was chosen as our material in order to render the reconstructed skull prototype radio opaque. The plaster model was then subjected to CT scanning using the same protocol as the original clinical scan. The CT dataset describing the digital reconstruction was transferred to the image-guidance workstation through the hospital LAN, as had been the original clinical dataset.

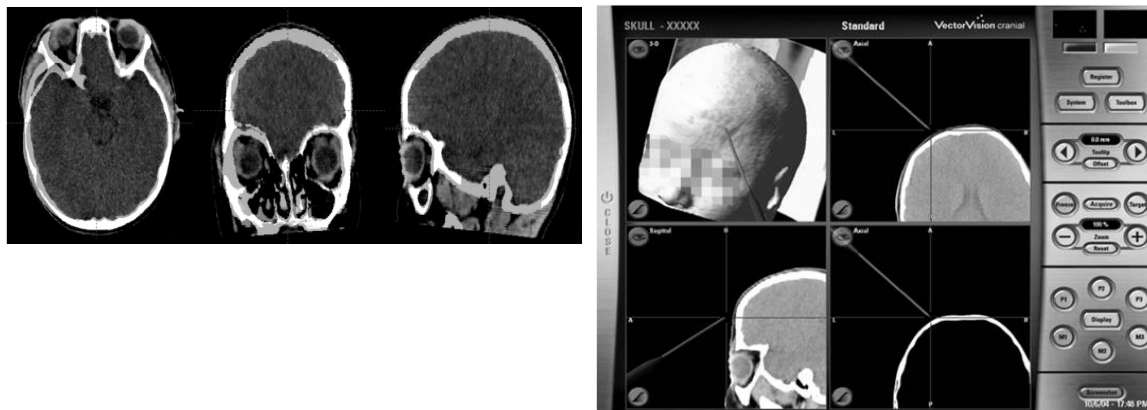


(a): Fabrication Layered Manufacturing View (slice parameters: 0.003in, plaster material, build time: 16hrs) (b): Prototype Fabricated using Z402 system

Figure 5.8: Prototype fabrication using ZCorp 3DP™ system

On the image-guidance workstation the surgeon fused the data set for the clinical image with the dataset for the digital reconstruction. The right orbits, which were identical in both images, were superimposed (Figure 5.9) to create the surgical plan. In the operating room the patient's head was immobilized in a 3-point pin head-holder and registered with the image-guidance system using the soft tissue windowed, 3-dimensional reconstruction of the clinical CT image and a laser-scanning device (Z-Touch®; BrainLAB AG, Heimstetten, Germany). When the frontal bones, the left superior and lateral orbital margins, and the left temporal bone had been exposed through a bicoronal incision, the prominent squamous temporal bone was harvested for an on-lay graft for the inferior frontal region. The graft was secured in place by means of through-and-through absorbable screws, and it was supplemented with hydroxyapatite paste. As the augmentation of the inferior frontal region and the orbital margin proceeded, it was checked against the digital reconstruction using the bayoneted image-guidance probe (Figure 5.9). At the conclusion of the procedure, the frontal regions and the superior orbital margins were symmetrical as judged both by the eyes of the surgeon and by the

extraoperative digital surgical plan. Therefore the virtual/prototype model have been not merely as a qualitative assessment alone but more importantly a quantitative measurement on the accuracy of the surgery performed. This therefore can be used as a real time quality control function for reconstructive surgeries.



(a): Fusion of Original and Reconstructed dataset to illustrate the difference between the 2 sets in a quantitative manner. (the brighter regions indicate the data set from the reconstructed plaster model.

(b): Real time image guidance using bayoneted probe to find out the accuracy of the reconstruction. The image on the bottom right half of the screen shows the reconstructed plaster skull data set.

Figure 5.9: Real time quality control interface

Treatment of this older child's relatively mild facial deformity lent itself to extraoperative simulation and intraoperative control using a popular computer-assisted design package and a commercially available image-guidance system. Software incompatibility created a vexing problem with data transfer that was solved by fabrication of a plaster model of the simulated reconstruction.

Routine application of this paradigm to the more severe deformities typically encountered in infancy requires a number of refinements. A safe and dependable method for immobilization of the infant skull is necessary for registration with the image-

guidance system. More powerful CAD software is necessary to support complex manipulations of the craniofacial skeleton compatible, ideally, with the physical properties of bone in infancy. And this CAD software must save its work product in either a digital form or, as in the current case, a physical form that can be accessed by the neurosurgical image-guidance system. The technical challenges presented by the application of CAD methods and image-guidance in the correction of craniofacial deformities have been reviewed by Hassfeld (2001) and Vannier (1996). The individual components of this paradigm have been developed to varying degrees of sophistication by groups working predominantly in oral and maxillofacial surgery and reconstructive plastic surgery. Initial efforts focused on fabrication of stereolithographic biophysical models from clinical CT datasets [D'Urso et al., 1998, Lambrecht et al., 1990, Levi et al., 2002, Muller et al., 2003] for a physical qualitative assessment of the patient defect. Many surgeons have found such models to be useful qualitative aids in the study of deformities and the planning of reconstructions. The models themselves can be measured, marked, cut, and reassembled to create an analogical surgical simulation. Increasingly elegant software systems have subsequently been described for quantitative digital simulation of craniofacial reconstructive surgery [Xia et al., 2000, Burgielski et al., 2002, Girod et al., 2001, Troulis et al., 2002, Meehan et al., 2003]. The most sophisticated of these systems offer a set of basic surgical maneuvers, such as ablation of bone, osteotomy, translation and rotation of osseous fragments, and even bending of osseous surfaces [Jans et al. 1999, Munchenburg et al., 2000]. Soft tissue contours can be laid onto the reconstructed craniofacial skeleton to create life-like previews of cosmetic results. Commercially available software systems for manipulation of biomedical images

have been reviewed by Vannier (1996). The problem of transfer of a digitally simulated reconstruction to the clinical setting has been attacked in various ways as well. The use of photographs and the creation of sterilizable metal templates have been reported [Mommaerts et al., 2001]. Unlike the MAGICCS® system employed in the current case, some of the medical CAD software systems allow work product to be saved as DICOM files that, in theory, can be opened by many commercial image-guidance systems. Alternately, unlike the VectorVision® system employed in the current case, some commercial image-guidance systems apparently incorporate rudimentary CAD functionality and thus negate the transfer problem entirely for relatively simple reconstructions [Vougioukas et al., 2004]. So far as the authors are aware, the use of radio-opaque rapid prototyped models to transfer a digitally simulated reconstruction to a surgical image-guidance system has not been described before. The precision of the rapid prototyping fabrication process has not been analyzed quantitatively, but the ease with which the shared sections of the clinical and the reconstructed images could be superimposed and “fused” on the image-guidance workstation suggests that it is sufficient for the correction of calvarial deformities. Although its dependence on access to hardware and software systems for rapid prototyping limits its general clinical applicability, the authors believe that enhancements to the commonly available commercial medical image processing software such as MIMICS® can help avoid the need for any rapid prototyping system. This therefore can be used by hospitals and can be adapted to any commercially available surgical image-guidance system. Figure 5.10 illustrates the process that would be ideal. This also presents a cost effective approach to surgeries conducted in third world countries.

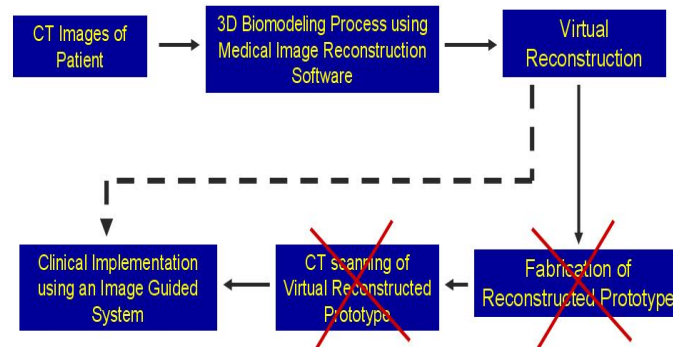


Figure 5.10: Direct conversion of the STL model to DICOM format

The ability for surgeons to have a real time quantitative assessment will certainly aid in his judgment during the surgical procedure without relying on past experience. Hence such processes involve a proficiency in both technical as well as artistic creativity skills. The image guided reconstructive surgery aims at reducing the artistic component in such surgical procedures allowing them to correct deviations from the reconstructed template in real time. Discrepancies between the planning performed at the CAD workstation and the actual surgical execution can be detected and corrected on the spot. The image guided reconstructive surgical procedure provides the surgeon with a tool aimed in reducing surgical errors and thereby increase the rate of successful reconstructive procedures with minimal post operative treatments.

CHAPTER 6: CONCLUSIONS AND RECOMMENDATIONS

1.1 Summary

Modeling, design and fabrication of tissue scaffolds to meet multiple biological and biophysical requirements is always a challenge in tissue engineering. This is further amplified when designing load bearing scaffolds for bone and cartilage tissue application. In these cases, tissue scaffolds need to be designed with intricate architecture, porosity, pore size and shape, and interconnectivity in order to provide the needed structural strength, transport nutrients, and the micro-environment for cell and tissue in-growth. By selecting the appropriate unit cell interior structures, properties such as the effective mechanical properties, diffusion and permeability characteristics can be controlled. Depending on the fabrication method used, varying complex internal patterns can be fabricated.

The application case studies also show the capability and potential of computer-aided tissue engineering. CAD in conjunction with advanced modeling and freeform fabrication technology can create scaffolds that go beyond conventional designs currently used in tissue engineering. It can create complex structures with functional components that are difficult, if not impossible to create with conventional chemical based tissue scaffold fabrication techniques. The application of CATE to tissue engineering also allows, for example, controlling and designing the overall shape of the scaffold to match a patient's CT or MRI data; the internal architecture (pore size, porosity, and interconnectivity) by using the power of CAD techniques; heterogeneous scaffold with

different mechanical and geometrical properties, and to freeform fabricate the designed scaffolds.

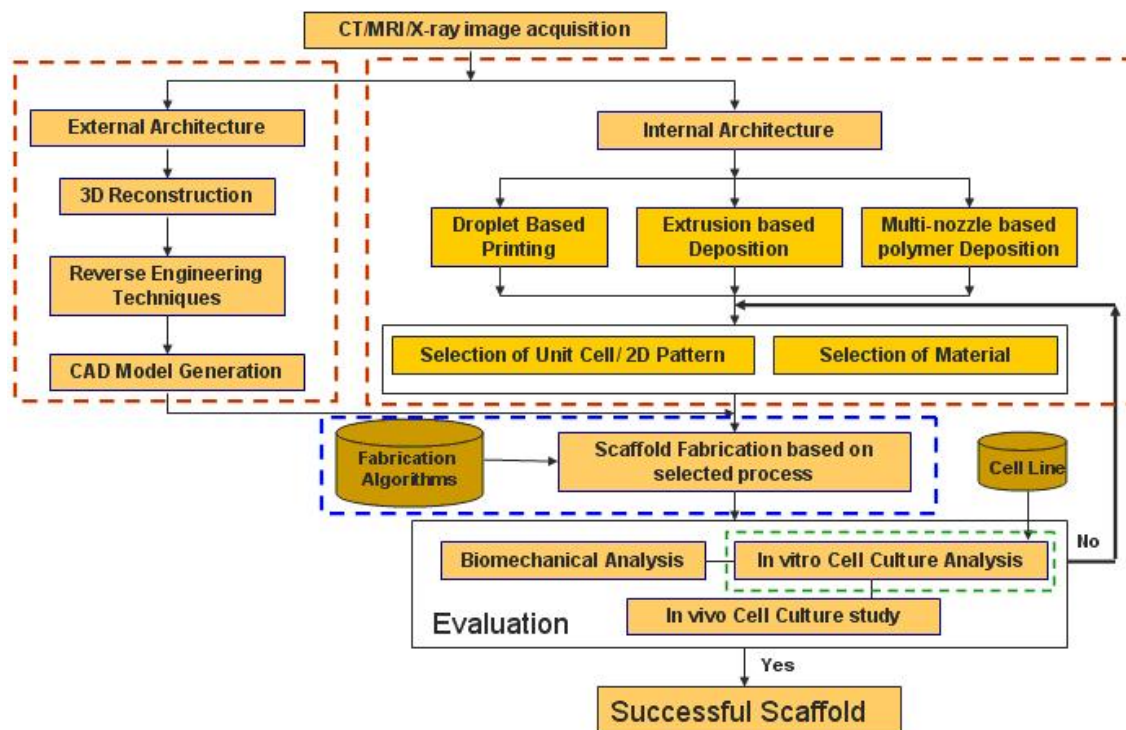


Figure 6.1: Process flow path from images to final scaffold

Figure 6.1 shows a graphical representation for the fabrication of a scaffold using CT/MRI scans of the defect site as the input. The CT/MRI scans are first used to reconstruct the external architecture of the defect site through available reverse engineering techniques and a CAD model is generated. Simultaneously, the CT/MRI scans can also serve as a template for the selection/reconstruction of the interior architecture. A unit cell based inclusion or stochastic modeling based methods can be used in the process and based upon the kind of manufacturing system that is used,

appropriate patterns of the interior architecture are mapped onto the entire scaffold structure. With the aid of fabrication algorithms, the CAD model of the scaffold architecture is obtained from the system and is send out to the evaluation phase where it is seeded with the applicable cell line and monitored for cellular response for an extended period of time during the course of the biological study.

This thesis has attempted to devise process mechanisms, developed in-house algorithms, usage of enabling technologies for the design and fabrication of the scaffold as highlighted by the dashed lined boxes. Considerable work can yet be done to improve upon the techniques used at various stages of the process and are highlighted in section 3 of this chapter.

1.2 Research Contributions

The contributions of this research are summarized as follows:

(1) The development of a BioCAD modeling technique for the design and representation of patient specific 3D tissue models based on non-invasive medical image data. The developed 3D BioCAD models can be used for analysis, simulation, surgical planning, and design and fabrication of patient specific implants and medical devices.

(2) The development of a biomimetic design approach for the design of load bearing tissue scaffolds subject to multiple biophysical, geometrical and manufacturing requirements, including the design of unit cell micro-architectures based on tissue morphology, unit cell characterization and evaluation of the mechanical and transport properties, and the use of the unit cells as building block to design anatomic tissue scaffold replacement. Characterization techniques using in-house developed algorithms

to predict effective mechanical and tortuosity properties of the various unit cell architectures may provide important information for future study of a design induced cell-scaffold interaction and the influence of transport properties on scaffold cellular tissue engineering behavior.

(3) The development of a CAD based path planning procedure through a direct slicing algorithm which can convert a neutral ISO (full definition) standardized STEP (full definition) formatted NURBS (full definition) geometric representation to a tool path instruction set for layered freeform fabrication. The developed direct slicing approach overcomes the inherent limitation of using current STL format in terms of the improved process accuracy, easy of model database management and the potential for the representation of heterogeneous information.

(4) The development of a novel Internal Architecture Design (IAD) approach for the mapping of characteristic micro-architecture of 3D designed scaffold to a layered 2D process pattern. This mapping procedure based process planning algorithm is implemented for three-dimensional printing and extrusion based freeform fabrication techniques. The Interior Architecture Design (IAD) approach enables the generation of layered freeform fabrication tool paths without forming a CAD model *prior* to the fabrication of complex scaffolds. .

1.3 Future Research Recommendations

The work presented in this thesis can be improved upon to include more features and algorithm capabilities in the design of tissue scaffolds. Following research tasks have been outlined and can be undertaken to for future research and development.

1.3.1 Biomimetic Design of Tissue Scaffold Architectures

1. A unit cell library that is composed of several complex internal architectures has been proposed to suit various applications for both hard and soft tissue engineering. Research has proven that cellular response is markedly different for several architectural shapes. However, there is a lack of understanding as to the exact significance of these unit cell architectures. Do cells prefer rectangular holes or do they prefer circular holes? Does the Hilbert and Sierpinski pattern influence cellular proliferation rates and direction? Research must be performed to link the biological response to the design theory of the unit cells. Once this link has been researched and understood, unit cell architectures can be optimized to obtain desired cellular response characteristics.
2. On a side note, scaffold structures that are designed to biodegrade over time will undergo changing geometrical structure influenced both by the added extra-cellular matrix produced by the cells themselves and the erosion of the material over time. Hence tortuosity parameters are dynamic and future work can include simulation algorithms to predict the dynamic change of tortuosity taking into account cell proliferation rates, oxygen consumption, nutrient transfer etc.

1.3.2 Direct Slicing of CAD Models

1. To further enhance the capability of the current direct slicing algorithm, an adaptive direct slicing procedure can be implemented wherein the slicing thickness does not remain constant and its value adaptively changes depending on the curvature of the model.
2. An optimization scheme can also be implemented to orient the model within the fabrication bed space to obtain optimum part qualities in terms of reducing the build height and fabrication time. Reduction in build height can greatly reduce the staircase stepping effect and hence ensure better fabricated quality.
3. Currently, the algorithm has been set up to extract NURBS data information and then sliced to obtain the layer contours. The algorithm can be developed to slice more general features such as planes, spheres and cylinders to enhance the capability of the algorithm for more general models.

1.3.3 Internal Architecture Design of Tissue Scaffolds

1. The IAD process described in this thesis facilitates the fabrication of heterogeneous structures in the structural sense. By a combination of different material architectures within the same structure, true heterogeneity both in terms of material and structure can be achieved. By assigning specific material information for each unit cell, the process will carry on this information to the point of fabrication. A framework for

heterogeneous modeling has been formulated [Sun et al., 2001] and a future extension of the IAD process would be to incorporate material heterogeneity within the scaffold structure. Process planning instructions generated from the IAD algorithm will then allow the fabrication using biomanufacturing systems.

1.4 Concluding Remarks

The field of computer-aided tissue engineering is still in its infancy. There is still much to be learned and discovered. With advances in computing power, with new software specifically developed for tissue engineering and biological systems, and with improvements in freeform fabrication process, one can envision that CATE will play a significant role in the future of tissue engineering. The bio/tissue informatics model developed based on the CATE approach will eventually provide precise design and control of architecture with multi-material printing for a better understanding of cellular biology. Although SFF based methods have significantly produced better scaffolds, they have shortcomings such as limited material selection, structural resolution and limited CAD capability. Research investigators are now addressing these needs by providing for a broader material library, higher controlled resolution using advanced bio-friendly SFF techniques and CAD/CAE tools for the design of heterogeneous tissue scaffolds.

LIST OFF REFERENCES

- [1] Valencia A., Bateman A., “Increasing the Impact of Bioinformatics”, *Bioinformatics*, 2005, 21(1): 1-1
- [2] Ang T.H., Sultana F.S.A., Hutmacher D.W., Wong Y.S., Fuh J.Y.H., Mo X.M., Loh H.T., Burdet E., Teoh S.H., “Fabrication of 3D chitosan-hydroxyapatite scaffolds using a robotic dispensing system”, *Mater. Sci. Eng.* 2002;20:35–42
- [3] Atala A, Bauer SB, Soker S, Yoo JJ, Retik AB. , Tissue-engineered autologous bladders for patients needing cystoplasty. , *Lancet*. 2006; 367(9518):1215-6.
- [4] Bablani, Minoo, Bagchi, A., "Quantification of Errors in Rapid Prototyping Processes, and Determination of Preferred Orientation of Parts," *Transactions of the North American Manufacturing Research Institution of the SME*, vol. XXIII, SME, Houghton, MI, May 1995:319-324.
- [5] Bajaj, C. L., Coyle, E. J., Lin, K.-N., “Arbitrary Topology Shape Reconstruction from Planar Cross Sections”, *Graphical Models and Image Processing*, 1996; 58(6):524-543.
- [6] Bartels R., John B., Brian B., “ An introduction to splines for Use in computer graphics and geometric modeling”, Morgan Kaufmann Press, Los Altos, CA, 1987; ISBN 1558604006
- [7] Barth W., Stürzlinger W., “Efficient ray tracing for Bezier and B-spline surfaces”, *Computers and Graphics*, 1993;17(4)
- [8] Borden, M., Attawia, M., Khan, Y., Laurencin, C., “Tissue engineered microsphere-based matrices for bone repair: design and evaluation”, *Biomaterials*, 2002; 23(2): 551-559
- [9] Burgielski Z, Jansen T, von Rymon-Lipinski B, Hanssen N, Keeve E: Julius--a software framework for computer-aided-surgery. *Biomed Tech (Berl)*, 2002; 47:101-103.
- [10] Chalasani, K. L. and Bagchi, A. "On a Slicing Algorithm for Free Form Fabrication", *IEEE Transaction Computer Graphics and Applications*, 1991
- [11] Cha-Soo Jun; Dong-Soo Kim; Deok-Soo Kim; Hyun-Chan Lee; Jiseon Hwang; Tien-Chien Chang ;“Surface slicing algorithm based on topology transition “,*Computer Aided Design* 2001;33(11):825-38
- [12] Chu, T.-M.G., et al., Mechanical and in vivo performance of hydroxyapatite implants with controlled architectures. *Biomaterials*, 2002. 23(5):1283-1293.
- [13] Chua, C.K., Leong, K.F., Cheah, C.M., Chua, S.W., “Development of a tissue engineering scaffold structure library for rapid prototyping. Part 1: Investigation and classification”, *Int J. of Advanced Manufacturing technology*, 2002;21(4):291-301
- [14] Cima MJ, Sachs E, Cima LG, Yoo J, Khanuja S, Borland SW, Wu BM, Giordano RA. Computer-derived microstructure by 3D printing: bio- and structural materials. *Proceedings of the SFF symposium*, 1994.

- [15] Cundy, H., Rollett, A. *Mathematical Models*, 3rd ed. Stradbroke, England: Tarquin Pub., pp. 67-68, 1989.
- [16] D'Urso PS, Atkinson RL, Lanigan MW, Earwaker WJ, Bruce IJ, Holmes A, et al: "Stereolithographic (SL) biomodelling in craniofacial surgery", *Br J Plast Surg*, 1998; 51:522-530.
- [17] Daniel L., Gonczarowski J., "Improved techniques for ray tracing parametric surfaces", *The visual computer*, 1990; 6(3); 134-152.
- [18] Dolenc, Mäkelä I, "Slicing procedures for layered manufacturing techniques," *Computer-Aided Design* 1992; 26(2):119-126.
- [19] Eaglstein WH, Falanga V., "Tissue engineering and the development of Apligraf, a human skin equivalent", *Clin Ther.* 1997;19(5):894-905.
- [20] Evans P., Starly, B., Sun, W., "Computer-Aided Tissue Engineering for the Design and Evaluation of Lumbar-Spine Arthroplasty", *Computer-Aided Design and Applications*, 2006; 3 (6): 771-778
- [21] Fang, Z., Starly, B. and Sun, W., "Computer-Aided Characterization of Effective Mechanical Properties for Porous Tissue Scaffolds," *Computer-Aided Design*, 2005; 37(1): 65-72.
- [22] Folch, A., Toner, M. "Microengineering of Cellular Interactions", *Annual Rev. of Biomedical Engineering* 2000;2:227
- [23] Fournier A., Buchanan J., "Chebyshev polynomials for boxing and intersection of parametric curves and surfaces", *Eurographics*, 1994; 13(3).
- [24] Frank D., Fadel G., "Preferred Direction of Build for Rapid Prototyping Processes," *Proceedings of the Fifth International Conference on Rapid Prototyping*, R. P. Chartoff, A. J. Lightman, and J. A. Schenk, eds. University of Dayton, June 1994; 191-200.
- [25] Girod S, Teschner M, Schrell U, Kevekordes B, Girod B: Computer-aided 3-D simulation and prediction of craniofacial surgery: a new approach. *J Craniomaxillofac Surg*, 2001; 29:156-158.
- [26] Gordon J, Kang QK, Shor L, Gucer S, Hartsock LA, Sun W, An YH: Osteogenesis of cell-seeded polycaprolactone scaffolds in nude mice. *MUSC Orthopaedic Journal*, 2005; 8: 43-44.
- [27] Griffith LG, Wu BM, Cima MJ, Chaignaud B, Vacanti JP. In vitro organogenesis of liver tissue. *Ann NY Acad Sci* 1997; 831: 382-97.
- [28] Griffith LG. , "Emerging design principles in biomaterials and scaffolds for tissue engineering", *Ann N Y Acad Sci.*, 2002;961:83-95
- [29] Guduri, S., Crawford, R.H., and Beaman J.J., "A Method To Generate Exact Contour Files For Solid Freeform Fabrication," *Proceedings of SolidFreeform Fabrication Symp.*, 3-5 August 1992, The University of Texas at Austin, Austin, Texas: 95-101.

- [30] Hans Sagan, *Space-Filling Curves*, Springer-Verlag, New York, 1994. ISBN: 0-387-94265-3.
- [31] Hassfeld S, Muhling J, "Computer assisted oral and maxillofacial surgery--a review and an assessment of technology", *Int J Oral Maxillofac Surg*, 2001;30:2-13.
- [32] Hollister, S.J. Levy, R.A., Chu, T.W., Halloran, J.W., Feinberg, S.E., "An image based approach for designing and manufacturing craniofacial scaffolds", *Int J of Oral and Maxillofacial surgery*, 2000; 29; 67-71
- [33] Hollister, S.J., et al., "An image-based approach for designing and manufacturing craniofacial scaffolds", *International Journal of Oral and Maxillofacial Surgery*, 2000. 29(1):66.
- [34] Hollister, S.J., R.D. Maddox, and J.M. Taboas, Optimal design and fabrication of scaffolds to mimic tissue properties and satisfy biological constraints. *Biomaterials*, 2002. 23(20): 4095-4103.
- [35] Hutmacher DW, Schantz T, Zein I, Ng KW, Teoh SH, Tan KC., "Mechanical properties and cell cultural response of polycaprolactone scaffolds designed and fabricated via fused deposition modeling", *Journal of Biomedical Materials Research*, 2001; 55:203-216.
- [36] Hutmacher, D.W., "Elastic cartilage engineering using novel scaffold architectures in combination with a biomimetic cell carrier", *Biomaterials*, 2003;24(24):4445-4458.
- [37] Hutmacher, D.W., Sittinger, M., Risbud M.V., "Scaffold-based tissue engineering: rationale for computer-aided design and solid free-form fabrication systems", *Trends in Biotechnology*, 2004; 22(7):354-362.
- [38] Jamieson R., Hacker H., "Direct slicing of CAD models for rapid prototyping" *Rapid Prototyping Journal* 1995; 1(2); 130-147.
- [39] Jans G, Vander Sloten J, Gobin R, Van der Perre G, Van Audekercke R, Mommaerts M: Computer-aided craniofacial surgical planning implemented in CAD software. *Comput Aided Surg*, 1999; 4:117-128.
- [40] Jessica Viola, Bhavya Lal, Oren Grad "The Emergence of Tissue Engineering as a Research Field", National Science Foundation Report, October 14, 2003
- [41] Kajiya J.T., "Ray tracing parametric patches", *Computer Graphics SIGGRAPH '82 Proceedings* 1982; 16(3); 245-254.
- [42] Kalita, J.S, Bose S., Hosick H., Bandyopadhyay A., "Development of controlled porosity polymer-ceramic composite scaffolds via fused deposition modeling", *Materials Science and Engineering C*, 2003; 23:611– 620
- [43] Keppel, E., "Approximating Complex Surfaces by Triangulation of Contour Lines", *IBM Journal of Research and Development*, 1975; 19(1): 2-11.

- [44] Khalil S., Nam J., Sun W., "Biopolymer Deposition for Freeform fabrication of Tissue Scaffolds", the Polymer Networks 2004 Conference (NIH/NICHHD), August 16-18, 2004, Natcher Conference Center, NIH, Bethesda, Maryland.
- [45] Khalil, S., Nam, J., Sun, W., "Multi-nozzle Deposition for Construction of 3D Biopolymer Tissue Scaffolds," Rapid Prototyping Journal, 2005; 11(1), 2005: 9-17.
- [46] Kim SS, Utsunomiya H, Koski JA, Wu BM, Cima MJ, Sohn J, Mukai K, Griffith LG, Vacanti JP., " Survival and function of hepatocytes on a novel three-dimensional synthetic biodegradable polymer scaffold with an intrinsic network of channels", *Annals of Surgery* 1998; 228:8-13
- [47] Lam CXF, Mo XM, Teoh SH, Hutmacher DW. "Scaffold development using 3D printing with a starch-based polymer", *Mater Sci EngC* 2002; 20(1-2):49-56.
- [48] Lambrecht JT, Brix F, "Individual skull model fabrication for craniofacial surgery", *Cleft Palate J*, 1990, 27:382-385.
- [49] Landers, R., Hübner, U., Schmelzeisen R., Mülhaupt R., "Rapid prototyping of scaffolds derived from thermoreversible hydrogels and tailored for applications in tissue engineering", *Biomaterials*, 2002; 23(23): 4437-4447
- [50] Langer, R. and Vacanti, J.P., "Tissue Engineering", *Science*, 1993; 260: 920-926.
- [51] Langer, R., "Tissue Engineering: a new field and its challenges", *Scientific American*, 1999; 280:86-9.
- [52] Langer, R., *Biomaterials and biomedical engineering. Chemical Engineering Science Frontiers of Chemical Engineering Science*, 1995. 50(24): 4109-4121.
- [53] Lanza, R., Vacanti, J., *Principles of Tissue Engineering*. 2000: Academic Press.
- [54] Laurencin CT, El-Amin SF, Ibim SE, Willoughby DA, Attawia M, Allcock HR, Ambrosio AA., A highly porous 3-dimensional polyphosphazene polymer matrix for skeletal tissue regeneration. *J Biomed Mater Res*. 1996; 30(2):133-8.
- [55] Leong KF, Phua KK, Chua CK, Du ZH, Teo KO. Fabrication of porous polymeric matrix drug delivery devices using the selective laser sintering technique. *Proc Inst Mech EngH* 2001; 215(2): 191-201.
- [56] Levi D, Rampa F, Barbieri C, Pricca P, Franzini A, Pezzotta S, "True 3D reconstruction for planning of surgery on malformed skulls" *Childs Nerv Syst*, 2002; 18:705-706
- [57] Li Y, Ma T, Kniss DA, Lasky LC, Yang ST. "Effects of filtration seeding on cell density, spatial distribution, and proliferation in nonwoven fibrous matrices, *Biotechnol Prog*", 2001; 17(5):935-44.
- [58] Lin, F., Sun, W. and Yan, Y., "A Decomposition-Accumulation Model for Layered Manufacturing Fabrication", *Rapid Prototyping Journal*, 2001; 7 (1): 24-31

- [59] Lu L, Mikos AG., The importance of new processing techniques in tissue engineering.,MRS Bull., 1996; 21(11):28-32.
- [60] Ma W., Peiren W., " An adaptive slicing and selective hatching strategy for layered manufacturing ", Journal of Materials Processing Technology 1999; 89; 191-197
- [61] Malda J, Martens DE, Tramper J, van Blitterswijk CA, Riesle J., Cartilage tissue engineering: controversy in the effect of oxygen, Crit Rev Biotechnol. 2003; 23(3):175-94.
- [62] N.J. Mankovich, D.R. Robertson, A.M. Cheeseman, "Three-dimensional image display in medicine", J. Digit. Imaging, 1990;3 (2):69-80.
- [63] Marmulla R, Niederdellmann H: Surgical planning of computer-assisted repositioning osteotomies. Plast Reconstr Surg, 1999; 104:938-944
- [64] Marsan A., Kumar V., Dutta D., Pratt M.J., "An Assessment of Data Requirements and Data Transfer Formats for Layered Manufacturing", Technical Report NISTIR 6216, National Institute of Standards and Technology, Gaithersburg, MD.
- [65] Marsan, A. L., Dutta, D., "Construction of a Surface Model and Layered Manufacturing Data From 3D Homogenization Output", Journal of Mechanical Design, 1996; 118(3): 412-418.
- [66] Martin W., Cohen E., Russell F., Peter S., "Practical Ray tracing of Trimmed NURBS surfaces", Journal of Graphics Tools 2000; 5(1): 27-52.
- [67] Martina M, Subramanyam G, Weaver JC, Hutmacher DW, Morse DE, Valiyaveetil S. "Developing macroporous bicontinuous materials as scaffolds for tissue engineering." Biomaterials. 2005;26(28):5609-5616
- [68] Medimonitor-Special Millennium Edition, Datamonitor, February 8, 2000.
- [69] Meehan M, Teschner M, Girod S: Three-dimensional simulation and prediction of craniofacial surgery. Orthod Craniofac Res, 2003; 6:102-107
- [70] Miot S, Woodfield T, Daniels AU, Suetterlin R, Peterschmitt I, Heberer M, van Blitterswijk CA, Riesle J, Martin I., "Effects of scaffold composition and architecture on human nasal chondrocyte redifferentiation and cartilaginous matrix deposition", Biomaterials., 2005; 26(15):2479-89.
- [71] Mommaerts MY, Jans G, Vander Sloten J, Staels PF, Van der Perre G, Gobin R: On the assets of CAD planning for craniosynostosis surgery. J Craniofac Surg, 2001; 12:547-554.
- [72] Moroni L., de Wijn J.,Van Blitterswijk C.A., "3D Plotted Scaffolds for Tissue Engineering: Dynamical Mechanical Analysis", European Cells and Materials 2004;7(1)
- [73] Muller A, Krishnan KG, Uhl E, Mast G, "The application of rapid prototyping techniques in cranial reconstruction and preoperative planning in neurosurgery", J Craniofac Surg 2003;14:899-914.

- [74] Munchenberg J, Worn H, Brief J, Kubler C, Hassfeld S, Raczkowsky J, "Intuitive operation planning based on force feedback", *Stud Health Technol Inform* 2000;70:220-226.
- [75] Murphy WL, Peters MC, Kohn DH, Mooney DJ., Sustained release of vascular endothelial growth factor from mineralized poly(lactide-co-glycolide) scaffolds for tissue engineering. *Biomaterials*. 2000 Dec; 21(24):2521-7.
- [76] Nam J., Starly, B., Darling A., Sun W., "Computer-Aided Tissue Engineering for Modeling and Design of Novel Tissue Scaffold", CAD'04 International Conference, Pattaya Beach, THAILAND, May 24-28, 2004.
- [77] Owen J., "STEP - An introduction", Information Geometers Ltd., 2nd edition (1997), ISBN 1-874728-11-9
- [78] Piatt, J.H., Jr., et al., Application of computer-assisted design in craniofacial reconstructive surgery using a commercial image guidance system. Technical note. *J Neurosurg*, 2006. 104: p. 64-7.
- [79] Piegl L.A., Tiller W., "The NURBS Book", Springer Verlag, New York, NY, 2nd edition, 1997, ISBN 3540615458
- [80] Pirone DM, Chen CS., "Strategies for engineering the adhesive microenvironment.", *Mammary Gland Biol Neoplasia*. 2004 Oct;9(4):405-17.
- [81] Prasad C. K., Krishnan LK. "Effect of passage number and matrix characteristics on differentiation of endothelial cells cultured for tissue engineering." *Biomaterials*. 2005;26(28):5658-67
- [82] Puduhal N.S., Dutta D., "Determination of Optimal Orientation Based on Variable Slicing Thickness in Layered Manufacturing," *Proceedings of the ASME Winter Annual Conference*, San Francisco, CA; Nov. 1995.
- [83] Rajagopalan M., Aziz N.M., Huey C.O., "A model for interfacing geometric modeling data with rapid prototyping systems", *Advances in Engineering Software* 1995; 23; 89-96.
- [84] Rogers D.F., "Introduction to NURBS: with Historical Perspective", Morgan Kaufmann Press, 2000, ISBN 1558606696
- [85] Sachlos E, Czernuszka JT., "Making tissue engineering scaffolds work. Review: the application of solid freeform fabrication technology to the production of tissue engineering scaffolds", *Eur Cell Mater*. 2003;5:29-39;
- [86] Saim AB, Cao Y, Weng Y, Chang CN, Vacanti MA, Vacanti CA, Eavey RD , Engineering autogenous cartilage in the shape of a helix using an injectable hydrogel scaffold.,, *Laryngoscope*. 2000; 110:1694-7.
- [87] Sederberg, T.W., Nishita T., "Curve intersection using Bezier clipping", *Computer-Aided Design*, 1990; 22(9); 538-549.

- [88] Shao X., Hutmacher, D.W., Tuan Ho S., James C.H., Lee H., "Evaluation of a hybrid scaffold/cell construct in repair of high-load-bearing osteochondral defects in rabbits", *Biomaterials*, 2006; 27(7):1071-1080
- [89] Starly B., Darling A., Gomez C., Sun W., Shokoufandeh A., Regli W., "Image Based Bio-CAD Modeling and Its Application in Biomedical and Tissue Engineering", *ACM Symposium on Solid Modeling and Applications 04*, Genova, Italy, June 9-11, 2004.
- [90] Starly B., Sun W., Lau A., Fang Z., "Biomimetic Model for Heterogeneous Bone Scaffold" *Biomedical Engineering: Recent Developments*: Editor, J. Vossoughi, 2002 Medical and Engineering Publishers, Inc.,305-306
- [91] Sun W., Lal P., "Recent development on computer aided tissue engineering – a review", *Computer Methods and Programs in Biomedicine* 2002; 67; 85-103.
- [92] Sun, W., "Multi-volume CAD Modeling for Heterogeneous Object Design and Fabrication," *Journal of Computer Science and Technology*, 2000; 15(1):27 – 36
- [93] Sun, W., Darling, A., Starly, B, Nam, J., "Computer-Aided Tissue Engineering: Overview, scope and challenges", *Biotechnology and Applied Biochemistry*, 2004; 39(1): 29-47.
- [94] Sun, W., Hu, X., "Reasoning Boolean Operation Based CAD Modeling for Heterogeneous Objects," *Journal of Computer Aided Design*, 2002; 34: 481-488.
- [95] Sweeney M.A.J., Bartels R., " Ray tracing free form B-spline surfaces", *IEEE Computer Graphics & Applications* 1986; 6(2).
- [96] Taguchi T, Xu L, Kobayashi H, Taniguchi A, Kataoka K, Tanaka J., "Encapsulation of chondrocytes in injectable alkali-treated collagen gels prepared using poly(ethylene glycol)-based 4-armed star polymer." *Biomaterials*, 2005;26(11):1247-5
- [97] Tan KH, Chua CK, Leong KF, Cheah CM, Cheang P, Abu Bakar MS, Cha SW. , "Scaffold development using selective laser sintering of polyetheretherketone-hydroxyapatite biocomposite blends", *Biomaterials*. 2003;24(18):3115-23.
- [98] Tran KT, Griffith L, Wells A., "Extracellular matrix signaling through growth factor receptors during wound healing.", *Wound Repair Regen*, 2004;12(3):262-8.
- [99] Troulis MJ, Everett P, Seldin EB, Kikinis R, Kaban LB: Development of a three-dimensional treatment planning system based on computed tomographic data. *Int J Oral Maxillofacial Surg*, 2002; 31:349-357.
- [100] Van Sint Jan S, Salvia P, Feipel V, Sobzack S, Rooze M, Sholukha V., "In vivo registration of both electrogoniometry and medical imaging: development and application on the ankle joint complex", *IEEE Trans Biomed Eng*, 2006;53(4):759-62.
- [101] Vannier MW, Marsh JL: Three-dimensional imaging, surgical planning, and image-guided therapy. *Radiol Clin North Am*, 1996; 34:545-563
- [102] Vougioukas VI, Hubbe U, van Velthoven V, Freiman TM, Schramm A, Spetzger U: "Neuronavigation-assisted cranial reconstruction" *Neurosurgery* 2004;55:162-167

- [103] Vozzi G., Flaim C., Ahluwalia A., Bhatia S., “Fabrication of PLGA scaffolds using soft lithography and microsyringe deposition”, *Biomaterials*, 2003; 24(14):2533-2540
- [104] Wang, F., Shor, L., Darling, A., Khalil, S., Sun, W., Güçeri, S., Lau, A., “Precision Extruding Deposition and Characterization of Cellular Poly-e-Caprolactone Tissue Scaffolds”, *Rapid Prototyping Journal*, 2004; 10(1):42-49.
- [105] Wells, D. *The Penguin Dictionary of Curious and Interesting Geometry*. London: Penguin, p. 229, 1991.
- [106] William H.P., Saul A., Brian P., “Numerical recipes in C : the art of scientific computing”, Cambridge University Press; 2nd edition, 1993, ISBN 0-521-43108-5
- [107] Williams J., Adewunmi A., Feinberg S., Hollister S., Das S. , “Bone tissue engineering using polycaprolactone scaffolds fabricated via selective laser sintering”, *Biomaterials*, 2005: 26(23)4817-4827
- [108] Wu BM, Borland SW, Giordano RA, Cima LG, Sachs EM, Cima MJ., “Solid free-form fabrication of drug delivery devices”, *Journal of Controlled Release* 1996; 40:77-87.
- [109] Xia J, Ip HH, Samman N, Wang D, Kot CS, Yeung RW, “Computer-assisted three-dimensional surgical planning and simulation: 3D virtual osteotomy”, *Int J Oral Maxillofacial Surg*, 2000; 29:11-17
- [110] Yang C.G., “On speeding up ray tracing of B-spline surfaces”, *Computer Aided design*, 1987; 19(3):122--130
- [111] Yang, S., Leong, K., Du, Z., Chua, C., “The design of scaffolds for use in tissue engineering. Part 2. Rapid prototyping techniques,” *Tissue Engineering*, 2002; 8 (1):1-11.
- [112] Yang, S.F., Du, Z.H., Leong, K.F., and Chua, C.K., “Review: The Design of Scaffolds for Use in Tissue Engineering. Part 1. Traditional Approaches”, *Tissue Engineering*, 2001; 7(6):679-690.
- [113] Zein I, Hutmacher DW, Tan KC, Teoh SH., “Fused deposition modeling of novel scaffold architectures for tissue engineering applications”, *Biomaterials*, 2002; 23:1169-1185.
- [114] Zeltinger J, Sherwood JK, Graham DA, Mueller R, Griffith LG., “Effect of pore size and void fraction on cellular adhesion, proliferation, and matrix deposition”, *Tissue Engineering*, 2001; 7:557-572..
- [115] Zhao Z., Laperriere L., “Adaptive direct slicing of the solid model for rapid prototyping”, *Proceedings of the First Conference on Rapid Prototyping and Manufacturing '98, Beijing*, 1998; 470-474.

VITA

- Education** **PhD**, Mechanical Engineering (2006), Drexel University, Philadelphia, PA
B.Tech, Mechanical Engineering (2001), Kerala University, Kerala, India
- Honors and Awards** Graduate Student Service Award, 2006
George Hill Jr. Fellowship, 2006
Graduate Research Award, 2006
MEM Outreach Service Award, 2006
Teaching Excellence Award, 2005
Joseph E. Caroleone Award for Academic Merit, 2004-2005
- Selected Journal Publications**
- Piatt, J.H., Jr., **Starly B.**, Sun, W., Faerber, E, “Application of computer-assisted design in craniofacial reconstructive surgery using a commercial image guidance system.”, Technical note. J Neurosurg, 2006. 104(1 Suppl): p. 64-7.
 - **Starly B.**, Lau W., Bradbury, T., Sun W., “Internal architecture design methodology for tissue replacement structures”, Computer Aided Design, , Vol. 38 (2), 2006, Pages 115-124
 - Fang, Z., **Starly, B.**, Sun, W., Shokufandeh, A., Regli, W., “A Computer Aided Multi-Scale Modeling for Direct Fabrication of Bone Tissue Structures”, Computer-Aided Design and Applications, Vol. 2, No 5, 2005
 - Sun, W., **Starly, B.**, Nam, J. and Darling, A., “Bio-CAD Modeling and Its Applications in Computer-Aided Tissue Engineering”, Computer-Aided Design, Vol. 37 (11), 2005, 1097-1114
 - **Starly, B.**, Lau, A., Sun, W. Lau, W. and Bradbury T., “Direct Slicing of STEP Based NURBS Models for Layered Manufacturing,” Computer-Aided Design, Vol 37, Issue 4, April 2005, pp 387-397
 - Fang, Z., **Starly, B.** and Sun, W., “Computer-Aided Characterization of Effective Mechanical Properties for Porous Tissue Scaffolds,” Computer-Aided Design, Vol. 37, No. 1, 2005, pp. 65-72.
 - Sun, W., Darling, A., **Starly, B**, Nam, J., “Computer-Aided Tissue Engineering: Overview, scope and challenges”, Biotechnology and Applied Biochemistry, Vol. 39, Issue 1, 2004, pp. 29-47.
 - Sun, W., **Starly, B.**, Darling, A., Gomez, C., “Computer-Aided Tissue Engineering: Application to biomimetic modeling and design of tissue scaffolds”, Biotechnology and Applied Biochemistry, Vol. 39, Issue 1, 2004, pp. 49-58.
- Patents**
- US Patent Pending: “Apparatus, Method and Article for Direct Slicing of STEP based NURBS models for Solid FreeForm Fabrication”, Application No:60/487,463 (co inventors - Thomas Bradbury, Dr. Wei Sun, Wing Lau, Dr. Alan Lau).

